Dynamics of a vortex in stratified-rotating fluids under the complete Coriolis force.

Iman Toghraei

▶ To cite this version:

Iman Toghraei. Dynamics of a vortex in stratified-rotating fluids under the complete Coriolis force.. Fluids mechanics [physics.class-ph]. Institut Polytechnique de Paris, 2023. English. NNT : 2023IPPAX034 . tel-04449818

HAL Id: tel-04449818
https://theses.hal.science/tel-04449818
Submitted on 9 Feb 2024

INSTITUT
POLYTECHNIQUE
DE PARIS

NNT : 2023IPPAX034

Thèse de doctorat

Dynamics of a vortex in stratified-rotating fluids under the complete Coriolis force

Thèse de doctorat de l’Institut Polytechnique de Paris
préparée à l’École polytechnique

École doctorale n°626 École doctorale de l’Institut Polytechnique de Paris (EDIPP)
Spécialité de doctorat : Mécanique des fluides et des solides, acoustique

Thèse présentée et soutenue à Palaiseau, le 26 avril 2023, par

IMAN TOGHRAEI

Composition du Jury :

Maurice ROSSI Directeur de Recherche, CNRS, IJLRA, Sorbonne Université	Président
Stéphane MATHIS Directeur de recherche CEA, DSM, IRFU, DAp, UMR AIM Paris-Saclay	Rapporteur
Patrice MEUNIER Directeur de recherche, IRPHE, CNRS, Aix Marseille Université	Rapporteur
Thomas DUBOS Professeur, LMD, École polytechnique	Examinateur
Paul BILLANT Directeur de recherche, LadHyX, CNRS, École polytechnique	Directeur de thèse

Abstract

The effects of the planetary rotation on geophysical fluid motions are usually studied using the traditional approximation. This consists in taking into account only the vertical component of the planetary rotation vector at a given latitude, while the horizontal component is neglected. This thesis studies the dynamics of a vortex when the horizontal component is also taken into account (non-traditional approximation). To this end, we perform direct numerical simulations of the evolution of a vertical Lamb-Oseen vortex in the presence of the complete Coriolis force in a stably stratified fluid. The results of these simulations are completed and interpreted by asymptotic analyses when the horizontal component of the planetary rotation is small and the Reynolds number is large. It is shown that the Coriolis force due to the horizontal component of the planetary rotation generates a critical layer at the radius where the angular velocity of the vortex is equal to the Brunt–Väisälä frequency when the Froude number is greater than unity. As a result, an intense vertical velocity field and a vertical vorticity anomaly are created in the vicinity of the critical layer. These flows can then lead to two types of instability: a two-dimensional instability triggered by the shear of the vertical vorticity anomaly and a three-dimensional instability due to the shear of the vertical velocity field. The domains of existence of these two instabilities are mapped in the parameter space. They both lead to a rapid decay of the vortex until the critical layer disappears when the angular velocity is everywhere below the buoyancy frequency. This process can occur even if the horizontal component of the planetary rotation is very small when the Reynolds number is large. Therefore, the horizontal component of the planetary rotation could have a much larger impact on geophysical vortices than one might think by considering only its order of magnitude.

Résumé

Les études des effets de la rotation planétaire sur les mouvements des fluides géophysiques sont généralement réalisées dans le cadre de l'approximation traditionnelle. Celle-ci consiste à ne prendre en compte que la composante verticale du vecteur de rotation planétaire à une latitude donnée, tandis que la composante horizontale est négligée. Cette thèse étudie la dynamique d'un tourbillon lorsque l'on tient compte également de la composante horizontale (approximation non traditionnelle). Dans ce but, nous effectuons des simulations numériques directes de l'évolution d'un tourbillon vertical de Lamb-Oseen en présence de la force de Coriolis complète dans un fluide stratifié de manière stable. Les résultats de ces simulations sont complétés et interprétés par des analyses asymptotiques lorsque la composante horizontale de la rotation planétaire est petite et le nombre de Reynolds grand.

La dynamique du tourbillon est régie par cinq paramètres adimensionnels : le nombre de Reynolds, le nombre de Froude qui mesure la stratification, les nombres de Rossby traditionnel et non-traditionnel qui mesurent respectivement la rotation d'ensemble verticale et horizontale et le nombre de Schmidt qui est toujours égal à l'unité.

Pour des conditions initiales purement bidimensionnelles, les simulations numériques montrent que le tourbillon reste complètement bidimensionnel tout au long de son évolution, même s'il y a trois composantes de vitesse. Il peut cependant devenir tridimensionnel lorsque de petites perturbations tridimensionnelles sont ajoutées initialement. Nous avons donc divisé notre étude en deux parties : l'évolution bidimensionnelle (chapitre 3) et l'évolution tridimensionnelle (chapitre 4).

Dans le cas bidimensionnel, les simulations numériques pour des nombres de Froude supérieurs à l'unité ont montré qu'un champ de vitesse vertical et une anomalie de vorticité verticale sont générés à un certain rayon en raison de la force de Coriolis non traditionnelle. Progressivement, le champ de vitesse vertical et l'anomalie de vorticité verticale se concentrent et s'amplifient au voisinage de ce rayon. A un certain moment, une instabilité bidimensionnelle apparaît dans l'écoulement pour des nombres de Reynolds suffisamment grands et des nombres de Rossby non-traditionnels $\widetilde{Ro}$ suffisamment faibles.

Pour comprendre cette dynamique, nous avons effectué des analyses asymptotiques pour de grands nombres de Rossby non-traditionnels $\widetilde{Ro}$. En l'absence d'effets visqueux et de dépendance temporelle, l'analyse théorique montre que la vitesse verticale est singulière lorsque le nombre de Froude est supérieur à l'unité à un rayon où la vitesse angulaire est égale à l'inverse du nombre de Froude (c'est-à-dire la fréquence de Brunt-Väisälä sous forme dimensionnelle). Cette singularité est d'abord régularisée par la dépendance temporelle, puis par une combinaison d'effets visqueux et de dépendance temporelle dans la phase de saturation. Ainsi, deux solutions linéaires pour la vitesse verticale et l'anomalie verticale de vorticité ont été fournies pour chaque étape de cette évolution. Ces solutions linéaires sont en parfait accord avec les simulations numériques dans les deux phases. Une analyse asymptotique des effets non-linéaires a également été réalisée. Les prédictions du système d'équations obtenu sont en meilleur accord avec les simulations numériques, ce qui indique l'importance des effets non-linéaires.

Ensuite, nous avons montré qu'un point d'inflexion apparaît dans le champ de

vitesse angulaire et qu'il est responsable de l'apparition de l'instabilité bidimensionnelle. En utilisant les solutions asymptotiques de la vorticité verticale, une condition d'instabilité exprimée en termes des nombres adimensionnels $(Re, \widetilde{Ro})$ a été dérivée à partir du critère de Rayleigh pour l'instabilité de cisaillement. Dans l'espace des paramètres $(Re, \widetilde{Ro})$, le critère prédit parfaitement les domaines stables et instables et montre que même pour de petits nombres de Rossby non traditionnels, le tourbillon est instable si le nombre de Reynolds est grand.

Nous avons ensuite examiné l'évolution du tourbillon lorsque de petites perturbations tridimensionnelles sont ajoutées initialement. Bien que l'évolution initiale du tourbillon reste similaire, l'instabilité peut différer : elle est tridimensionnelle en dessous d'un nombre de Rossby non traditionnel critique. Cette instabilité tridimensionnelle semble similaire à l'instabilité de cisaillement observée par Boulanger *et al.* (2007, 2008) sur un tourbillon incliné stratifié. Au-dessus du nombre de Rossby critique non traditionnel, l'instabilité reste bidimensionnelle comme observé précédemment. Par conséquent, l'instabilité dominante est déterminée par les paramètres du problème.

Pour comprendre la compétition entre les instabilités bidimensionnelles et tridimensionnelles, nous avons effectué une analyse de stabilité linéaire des écoulements issus des simulations numériques. Les résultats confirment que l'instabilité tridimensionnelle devient dominante par rapport à l'instabilité bidimensionnelle lorsque $\widetilde{Ro}$ diminue. Nous avons également effectué des analyses de stabilité locale des solutions asymptotiques linéaires et non linéaires fournies dans le chapitre 3 afin de mieux comprendre les instabilités. L'analyse locale de stabilité tridimensionnelle montre que le taux de croissance de l'instabilité tridimensionnelle peut être prédit de manière correcte par une équation de Rayleigh qui ne prend en compte que le champ de vitesse vertical comme écoulement de base. Cependant, sa précision diminue lorsque $\widetilde{Ro}$ augmente pour un nombre de Reynolds donné. L'équation prenant en compte les effets du second ordre offre alors une meilleure précision. En outre, l'analyse de la stabilité bidimensionnelle locale donne une équation de Rayleigh avec le champ de vitesse angulaire comme écoulement de base qui permet de bien prédire le taux de croissance de l'instabilité bidimensionnelle.

Les analyses de stabilité locale démontrent ainsi que l'instabilité bidimensionnelle est une instabilité de cisaillement due à un point d'inflexion dans le profil de vitesse angulaire, tandis que l'instabilité tridimensionnelle est une instabilité de cisaillement du profil de vitesse verticale. En outre, nous avons étudié les domaines d'existence des instabilités dans l'espace des paramètres $(Re, \widetilde{Ro})$ au moyen d'analyses de stabilité locale. Les résultats montrent que l'instabilité bidimensionnelle est la plus dangereuse dans une gamme intermédiaire de $\widetilde{Ro}$ tandis que l'instabilité tridimensionnelle est dominante lorsque $\widetilde{Ro}$ est plus bas.

Globalement, ces deux instabilités conduisent à une décroissance rapide du tourbillon jusqu'à la disparition de la couche critique lorsque la vitesse angulaire est partout inférieure à la fréquence de flottabilité. Ce processus peut se produire même si la composante horizontale de la rotation planétaire est très faible lorsque le nombre de Reynolds est grand. Par conséquent, la composante horizontale de la rotation planétaire pourrait avoir un impact beaucoup plus important sur les tourbillons géophysiques que ce que l'on pourrait penser en considérant seulement son ordre de grandeur.

Acknowledgement

Firstly, I would like to thank my supervisor, Paul, for his support throughout these years. It was a great asset to my life to have his guidance and assistance. I enjoyed every conversation I had with him and I learned a lot from him. It has been an honor to work with Paul for nearly four years.

It was a pleasure to receive insightful questions and suggestions from my jury members, especially Stéphane Mathis and Patrice Meunier who reviewed my manuscript.

My thanks go out to Benjamin, Cécilia, Jérôme, Ruben, Samy, Salma, Tulio, Øyvind and the rest of the people at Ladhyx. You were great frineds and I'm going to miss you a lot in my life. Thanks to the staff at Ladhyx, Daniel, Melanie, Sandrine, Toaï and others for all the help they provided whenever necessary.

My heartfelt thanks to my parents and sister for their support throughout my life, especially during these years away from home.

And I would like to express my deepest gratitude to my lovely wife for the love and support she has shown me throughout these years...

Contents

List of Figures

Chapter 1

Introduction

1.1 Geophysical Fluid dynamics

Geophysical fluid dynamics is a branch of fluid dynamics that focuses on the motion of fluids on Earth, other planets, and stars. Studies of weather and climate dynamics in the atmosphere, ocean dynamics, waves, vortices, and astrophysical phenomena such as convection in stars are some examples. Research in geophysical fluid dynamics deals with the specificity of these flows compared to classical fluid mechanics.

The density stratification of the fluid and the presence of a background rotation separate geophysical fluid dynamics from classical fluid mechanics. The density variation can be due to the temperature gradient in the atmosphere or the salinity in the ocean. A density field that decreases vertically is said to be stable. Vertical motions are limited by the buoyancy force, but horizontal motions are not constrained by this force. Besides, geophysical flows are subjected to a background rotation caused by the rotation of the planet around its axis. This rotation adds an acceleration term called Coriolis acceleration (force) in the equations of motion. One of the effects of a background rotation is to impart rigidity along the axis of rotation to homogeneous fluids as depicted in figure 1.1(a) in the famous experiment of Taylor (1923). This effect is opposite to the one of a stable stratification which tends to spread the dye horizontally (figure 1.1(b). Hence, the vertical variations in geophysical flows result from the competition between these two effects. In the following, we try to explain some important aspects of these two characteristics of geophysical flows.

1.2 Stratification

Density variations are a key characteristic of fluid in geophysical fluid dynamics. It is essential that the lighter part of the fluid is placed above the heavier part of the fluid for a fluid to be stably stratified. In oceans and atmospheres, density variations are typically observed vertically, but in the presence of an ambient flow and rotation, they can also be observed horizontally due to the thermal wind relation. Brunt-Väisälä (buoy-

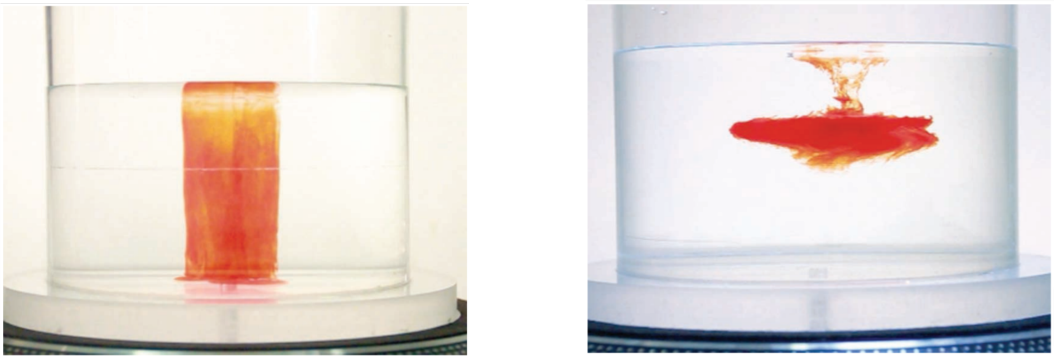

(a) (b)

Fig. 1.1: (*a*) Columnar behavior of the injected dye in a vertical rotating fluid. (*b*) Horizontal spreading of the injected dye in a stratified fluid. Source: Michael Le Bars.

ancy) frequency is used to measure stratification

$$N = \sqrt{-\frac{g}{\rho_0}\frac{\mathrm{d}\rho}{\mathrm{d}z}}, \tag{1.1}$$

where g is the gravity, ρ_0 a constant reference density and $\bar{\rho}(z)$ the mean density profile. A parcel oscillates at the Brunt-Väisälä frequency when it is slightly displaced in the vertical direction in a stably stratified fluid. Temperature variations in atmospheric and oceanic flows are the major reasons for variation in density, although salinity and compression of ocean waters also have an impact. Figure 1.2 shows the mean Brunt-Väisälä frequency profile in the pacific Ocean (Maes & O'Kane, 2014) where the temperature variations are mostly responsible for the density variations. To simplify things in fundamental studies, the Brunt-Väisälä frequency can be often considered constant, despite its change with depth.

The Froude number F_h is a dimensionless number that measures the ratio between the inertial forces and the buoyancy forces: $F_h \equiv U/(NL_h)$ where U and L_h are the reference velocity and length scales. If the Froude number is less than one, buoyancy forces dominate the inertial forces and the flow is said to be strongly stratified. Conversely, a flow with weak stratification has a Froude number larger than one.

1.3 Rotation

1.3.1 Basic concepts

It is more convenient to describe the motion of objects or fluids on Earth with respect to the Earth's surface. Consequently, all equations in geophysical fluid dynamics must be rewritten in a frame that rotates with the Earth. Consider an object or a parcel of fluid in a frame that rotates at a constant angular velocity Ω_b with respect to the inertial frame. If $\boldsymbol{r}$ is its position vector, the object velocity $\boldsymbol{v}$ (the position vector derivative with respect to time) in the two rotating and inertial frames are connected

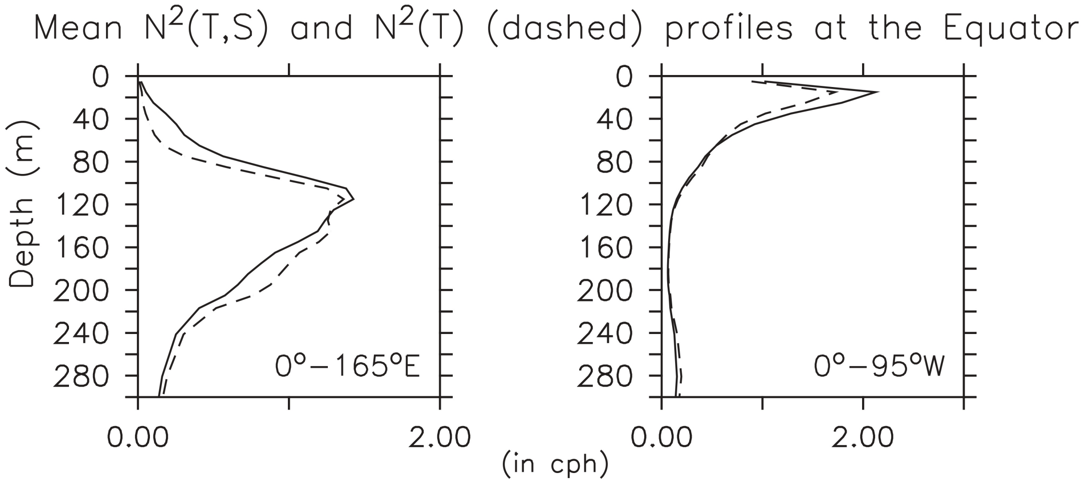

Fig. 1.2: Mean profile of the squared Brunt–Väisälä frequency (cycles per hour) calculated from temperature profile (dashed line) and from both temperature and salinity profiles (solid line) in the Pacific Ocean. Source: Maes & O'Kane (2014).

by

$$\boldsymbol{v}_I = \boldsymbol{v}_R + \boldsymbol{\Omega_b} \times \boldsymbol{r}, \tag{1.2}$$

where the subscripts I and R denote the inertial and rotating frames, respectively. This relation is next derived in order to obtain the relation between the accelerations a in the two frames which needed to apply Newton's second law of motion

$$\boldsymbol{a}_I = \boldsymbol{a}_R + 2\boldsymbol{\Omega_b} \times \boldsymbol{v}_R + \boldsymbol{\Omega_b} \times (\boldsymbol{\Omega_b} \times \boldsymbol{r}). \tag{1.3}$$

The relation (1.3) shows us that two additional terms must be added to the acceleration in the rotating frame. We call the first term, $2\boldsymbol{\Omega_b} \times \boldsymbol{v}_R$, Coriolis acceleration, and the second term, $\boldsymbol{\Omega_b} \times (\boldsymbol{\Omega_b} \times \boldsymbol{r})$, the centrifugal acceleration. When multiplied by a mass, they are called the Coriolis force and the centrifugal force, respectively.

1.3.2 Centrifugal force

The centrifugal force makes an outward pull in the rotating frame. However, it is canceled thanks to the gravity of the Earth. The net force between gravity and the centrifugal force is sometimes called effective gravity. The gravity is towards the center of the Earth whereas the centrifugal force is perpendicular to the rotation vector. Because of this horizontal component, the effective gravity is not exactly perpendicular to the surface of the earth. However, in geophysical sciences, the surface of the Earth is replaced by a virtual surface to which the net force is always perpendicular. This virtual surface is called *geoid*. The geoid can also be defined as a surface with constant geopotential or potential energy per unit mass.

1.3.3 Coriolis force

In contrast, the Coriolis force is directly incorporated into the equations of motion. From its definition, we can notice some properties of the Coriolis force: it is proportional to the magnitude of the relative velocity and the rotation vector and perpendicular to their directions. Without motions, the Coriolis force is then zero. In addition, for a positive rotation, the direction of the force is always on the right side of the direction of motion. The main effect of the Coriolis force is then to deflect particle motions in a direction perpendicular to the velocity.

The Rossby number measures the ratio between the inertial forces and the Coriolis force. It is defined as $Ro \equiv U/(2\Omega_b L_h)$ where Ω_b is the rotation rate. Rotation effects are negligible for large Rossby numbers. In contrast, when the Rossby number is small $Ro < 1$, the rotation has a significant effect, as shown in figure 1.1(a). Consequently, the Coriolis force becomes important when the turnover time scale L_h/U is at least of the order of the inverse of Earth's angular velocity Ω^{-1}. Because of this, the effects of the Coriolis force are more important on slow geophysical flows, i.e. large-scale flows.

1.3.4 Traditional approximation of the Coriolis force

Figure 1.3 shows the Earth rotating around its North-South pole axis at a constant rate. Although the Earth is almost a sphere, Cartesian coordinates are appropriate and more convenient for describing fluid motions when the scale of phenomena is smaller than the radius of the Earth. These Cartesian coordinates (x, y, z) are built on a plane that is tangent to the surface of the Earth (geoid) at the latitude ϕ. x is in the zonal direction, y is in the meridional direction and z is always perpendicular to the geoid surface. The rotation vector is expressed as

$$\boldsymbol{\Omega_b} = \Omega_b \cos(\phi)\boldsymbol{e_y} + \Omega_b \sin(\phi)\boldsymbol{e_z} = \frac{1}{2}\left(\tilde{f}\boldsymbol{e_y} + f\boldsymbol{e_z}\right), \tag{1.4}$$

where $f = 2\Omega_b \sin(\phi)$ is the vertical Coriolis parameter and $\tilde{f} = 2\Omega_b \cos(\phi)$ is the horizontal Coriolis parameter. The sign and magnitude of the Coriolis parameters depend on latitude. In particular, f is positive in the northern hemisphere and negative in the southern hemisphere, whereas $\tilde{f}$ is always positive. At the poles, $\tilde{f}$ equals zero while f is equal to zero at the equator.

In the so-called *traditional approximation* (Eckart, 1960), only accelerations due to the vertical Coriolis parameter f (traditional Coriolis force) are considered in the momentum equations while the terms proportional to $\tilde{f}$ are neglected. Apart from the mathematical simplicity provided by the approximation, physical reasons also support it. To see this, it is instructive to non-dimensionalize the continuity equation and the inviscid momentum equations in the presence of the complete Coriolis acceleration $2\boldsymbol{\Omega}_b \times \boldsymbol{u}$

$$\boldsymbol{\nabla}_h \boldsymbol{.} \boldsymbol{u}_h + \frac{\partial u_z}{\partial z} = 0, \tag{1.5a}$$

$$\frac{\partial \boldsymbol{u}_h}{\partial t} + \boldsymbol{u}_h \boldsymbol{.} \boldsymbol{\nabla_h} \boldsymbol{u}_h + w\frac{\partial \boldsymbol{u}_h}{\partial z} = -\frac{1}{\rho}\boldsymbol{\nabla}_h p - f\boldsymbol{e_z} \times \boldsymbol{u}_h - \tilde{f} w \boldsymbol{e_x}, \tag{1.5b}$$

$$\frac{\partial w}{\partial t} + \boldsymbol{u_h}\boldsymbol{.}\boldsymbol{\nabla}_h w + w\frac{\partial w}{\partial z} = -\frac{1}{\rho}\frac{\partial p}{\partial z} + b + \tilde{f}u, \tag{1.5c}$$

where p is the pressure, b the buoyancy and $\boldsymbol{u} = \boldsymbol{u}_h + w\boldsymbol{e_z}$ the velocity field where $\boldsymbol{u}_h = u\boldsymbol{e_x} + v\boldsymbol{e_y}$ is the horizontal velocity. To do so, we introduce non-dimensional variables with a prime such that

$$\begin{aligned} &\boldsymbol{u}_h = U\boldsymbol{u}_h^{'}, \quad w = Ww^{'}, \quad x = L_h x^{'}, \quad y = L_h y^{'}, \quad z = L_v z^{'}, \\ &t = \frac{L_h}{U}t^{'}, \quad p = \rho U^2 p^{'}, \quad b = \rho\frac{U^2}{L_v}b^{'}. \end{aligned} \tag{1.6}$$

Then, by using the relation $U/L_h = W/L_v$ imposed by the continuity equation (1.5a), the non-dimensional equations can be written

$$\boldsymbol{\nabla}_h^{'}.\boldsymbol{u}_h^{'} + \frac{\partial u_z^{'}}{\partial z^{'}} = 0, \tag{1.7a}$$

$$\frac{\partial \boldsymbol{u}_h^{'}}{\partial t^{'}} + \boldsymbol{u}_h^{'}.\boldsymbol{\nabla}_h^{'}\boldsymbol{u}_h^{'} + w^{'}\frac{\partial \boldsymbol{u}_h^{'}}{\partial z^{'}} = -\boldsymbol{\nabla}_h^{'}p^{'} - \frac{1}{Ro}\boldsymbol{e_z} \times \boldsymbol{u}_h^{'} - \frac{1}{\widetilde{Ro}}\frac{W}{U}w^{'}\boldsymbol{e_x}, \tag{1.7b}$$

$$\frac{W^2}{U^2}\left[\frac{\partial w^{'}}{\partial t^{'}} + \boldsymbol{u}_h^{'}.\boldsymbol{\nabla}_h^{'}w^{'} + w^{'}\frac{\partial w^{'}}{\partial z^{'}}\right] = -\frac{\partial p^{'}}{\partial z^{'}} + b^{'} + \frac{1}{\widetilde{Ro}}\frac{W}{U}u^{'}, \tag{1.7c}$$

where $Ro = U/(fL_h)$ and $\widetilde{Ro} = U/(\tilde{f}L_h)$. We see that the non-dimensional terms are all proportional to $W/(U\widetilde{Ro})$. Hence, these terms are a priori negligible since the vertical velocity in geophysical flows is generally much smaller than the horizontal velocity, either because the vertical scale is much smaller than the horizontal scale or because large vertical motions are prevented by the stratification. On the other hand, small-scale geophysical flows mainly have high-frequency motions, i.e. Ro and $\widetilde{Ro}$ are large so that rotation effects are too small to be important. This means that the traditional approximation should be justified for most geophysical flows. If the mentioned conditions are not met, the traditional approximation might be no longer legitimate as shown by Gerkema *et al.* (2008) in a comprehensive review on the effect of the non-traditional Coriolis force in geophysical flows. Following are some examples of flows where the traditional approximation has been shown to fail to accurately describe the dynamics.

1.3.5 Some effects of the non-traditional Coriolis force

Ocean deep convection is a process in which surface waters sink to great depths. This leads to the transport of numerous small-scale convective plumes to the bottom of the oceans. As deep convection has a long time scale and a strong vertical velocity, we expect the non-traditional Coriolis force to be significant. Observations reported by Pickart *et al.* (2002) revealed that plumes convection are slantwise in the Labrador Sea. Shear currents are primarily responsible for slantwise convection, but the effect of the non-traditional Coriolis force can also be significant (Marshall & Schott, 1999; Straneo *et al.*, 2002). Denbo & Skyllingstad (1996) numerically found that the non-traditional Coriolis force creates asymmetries in the circulation of a single penetrating plume.

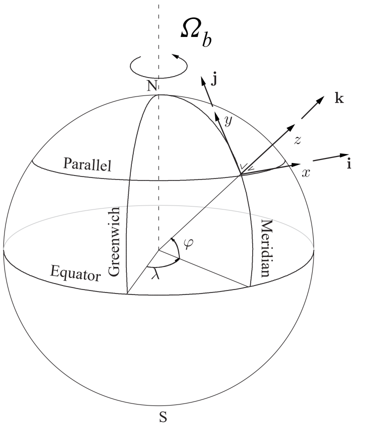

Fig. 1.3: Local Cartesian coordinate on the Earth's surface. x is in the zonal direction, y is in the meridional direction and z is always perpendicular to the geoid. ϕ is the latitude and λ is longitude. Source: Cushman-Roisin & Beckers (2011).

As a result of this asymmetry, the plume is inclined. In an experiment, Sheremet (2004) showed a developed non-vertical plume in the presence of an inclined background rotation (figure 1.4). While initially vertical (figure 1.4(a)), the plume becomes tilted along the background rotation axis (figure 1.4(c)).

Similarly, geophysical vortices can respond to the non-traditional Coriolis effect by a tilt of their axis. According to theoretical analyses (Gerkema *et al.*, 2008), mesoscale anticyclonic eddies (lenses) are predicted to be tilted in the presence of the complete Coriolis forces. Lavrovskii *et al.* (2000) and Semenova & Slezkin (2003) discuss the orientation of ellipsoidal vortex lenses in a linearly stratified fluid. Due to the non-traditional Coriolis force, lenses incline in both vertical and horizontal directions. Mid-latitude vortices are expected to have a vertical tilt of 30° to 10° and a horizontal tilt of less than 1°.

The non-traditional Coriolis force has also been shown to modify instabilities in addition to its tilting effect. Etling (1971) and Leibovich & Lele (1985) argue that the non-traditional Coriolis force enhances the instability of Ekman layers. Ekman currents are horizontal, but they contain vertical motions due to the formation of vortex rolls when they become unstable. The instability threshold decreases due to the effect of the non-traditional Coriolis force on these vertical motions. Further, the non-traditional Coriolis force can significantly modify the inertial instability (Chew *et al.*, 2022; Park *et al.*, 2021; Kloosterziel *et al.*, 2017; Tort *et al.*, 2016; Hua *et al.*, 1997). Chew *et al.* (2022) showed that a meridionally homogeneous flow at rest is subjected to a novel unstable mode. In addition, linear stability analysis by Park *et al.* (2021) indicates that the growth rate of the inflectional instability is significantly increased when the complete Coriolis force is present. Linear stability analysis of zonal jets done by Tort *et al.* (2016) shows an increase of the growth rate in weakly stratified fluid under the complete Coriolis force.

Wave dynamics are also affected by the non-traditional Coriolis force (Zhang & Yang, 2021; Kohma & Sato, 2013; Gerkema *et al.*, 2008). Gerkema *et al.* (2008) shows the effects of the non-traditional Coriolis forces on propagation and frequency range of internal waves. Zhang & Yang (2021) studied how the non-traditional Coriolis force influences the propagation of equatorial near-inertial solitary waves by altering the dispersion relation and the interaction with the base flow.

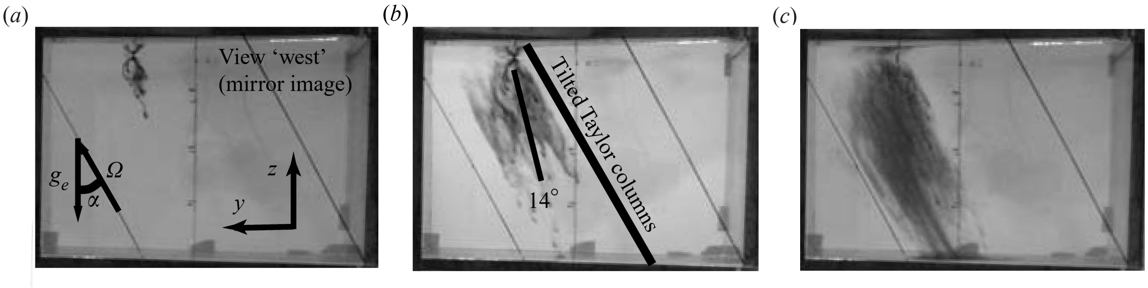

Fig. 1.4: The development of the dyed plume at three consecutive times (a) $t = 55$ s, (b) $t = 476$ s, (c) $t = 1592$ s from the start of the plume. The background rotation makes an angle $\alpha = 30°$ with the vertical axis. Source: Sheremet (2004).

1.4 Geophysical vortices

This thesis will explore the effects of the non-traditional Coriolis force on vortices. A vortex is a coherent structure with a closed circulation. They are observed both in the atmosphere and in the oceans. Atmospheric cyclones are large air masses that rotate around a center of low pressure. Different names are given to cyclones depending on their size and location of formation. The largest cyclones, known as synoptic cyclones, have a horizontal scale extending up to thousands of kilometers. A tropical or extra-tropical cyclone, a polar low, and a circumpolar vortex are examples of these cyclones. They are often generated by several atmospheric instabilities. A tropical cyclone obtains its energy from warm ocean waters, resulting in powerful winds, waves, and torrential rain. Tropical cyclones with maximum winds exceeding 65 knots are called hurricanes in the Atlantic and east Pacific, and typhoons in the western north Pacific. Figure 1.5(a) shows the tropical cyclone called Hurricane Katrina formed in late August 2005 in the United States. It caused 1,392 deaths and around $145.5 billion in damages (Knobby *et al.*, 2023). There are also smaller vortices in the atmosphere at the mesoscales. It is the vertical and horizontal shear of horizontal winds that form some mesoscale vortices in the atmosphere. They can be of several types including mesocyclones, tornadoes, and dust devils. Figure 1.5(b) shows a tornado. In spite of the fact that their horizontal length scales are relatively small, ranging from 10 meters to 1 kilometer, the wind speed of a tornado can reach 150 (m/s) causing considerable destruction and casualties every year (Schecter & Montgomery, 2006).

In the oceans, vortices are caused by barotropic and baroclinic instabilities, a change in ocean current direction, or even topography. Oceanic vortices can take the form of rings on the surfaces or they can exist in the ocean's depths. Oceanic eddies typically have a radius of 50 to 150 km, but have a much smaller thickness. These eddies are

Fig. 1.5: (*a*) Satellite image of the tropical cyclone called Hurricane Katrina that sustained winds greater than 250 kilometers per hour and caused 1,392 fatalities. Source:GOES 12 Satellite, NASA, NOAA. (*b*) A tornado captured by Jason Persoff.

therefore dominated by horizontal motions. They are responsible for transporting heat, and biological species, as well as mixing oceanic water masses (Flor, 2010).

Table 1.1 provides an estimation of the physical parameters of geophysical vortices. According to the table, the first three columns indicate the characteristic rotational velocity of the vortex U, its horizontal length scale L_h, and the ambient Brunt–Väisälä frequency N as reported by Schecter & Montgomery (2006). For non-tropical vortices, the Coriolis parameters f and $\tilde{f}$ are approximately taken at mid-latitude $\phi = 45°$. Based on these physical parameters, we can estimate the horizontal Froude number F_h, the traditional Rossby number Ro, and the non-traditional Rossby number $\widetilde{Ro}$ defined as

$$F_h = \frac{U}{N(L_h/2)}, \quad Ro = \frac{U}{(L_h/2)(f/2)}, \quad \widetilde{Ro} = \frac{U}{(L_h/2)(\tilde{f}/2)}. \tag{1.8}$$

The estimation of F_h, Ro and $\widetilde{Ro}$ are listed in the last three columns of table 1.1. The horizontal Froude number F_h varies from values higher than one for small-scale vortices to small values for large-scale vortices. As a result, large-scale vortices are strongly influenced by the buoyancy force. Furthermore, the traditional Rossby number Ro is relatively low for horizontally large-scale vortices such as circumpolar and synoptic vortices, which makes the traditional Coriolis force also important. Small-scale vortices like dust devils and tornadoes, however, have very large Rossby numbers $Ro \gg 1$.

1.5 Critical layers

1.5.1 Classical critical layers

A key element of the thesis will be the presence of critical layers. Critical layers are regarded as positions in which an inviscid small perturbation of a flow is potentially singular. From a classical point of view, it appears in a homogeneous parallel shear flow at a location where the phase speed of an imposed perturbation matches the local mean flow velocity (Stewartson, 1977). Such perturbation can be internal (Hickernell, 1984) or can be imposed either by external forces acting on boundaries such as Rossby waves (Stewartson, 1977). In theory, the singularity is smoothed either by introducing time dependency, viscosity, or non-linearity (Maslowe, 1986). In particular, studies have shown that a viscous critical layer length scale scaling as $Re^{-1/3}$ can smooth the singularity (Drazin & Reid, 2004). A critical layer can also lead to secondary instabilities such as shear instability (Killworth & McIntyre, 1985), and Rayleigh-Taylor instability (Lin *et al.*, 1993).

In addition to parallel shear flows, studies have shown that vortices also possess critical layers. Le Dizès (2000) has studied the critical layers that appear in a vortex subjected to a rotating strain field. The critical layer is located at the point where the angular velocity of the vortex equals the angular frequency of the strain. Similar to classical shear flows, singularity is then smoothed by the introduction of viscous and non-linear effects in the critical-layer region. Helical Rossby waves can also induce critical layers in vortices at a location where the frequency over the azimuthal mode of the imposed wave matches the vortex's angular velocity (Maslowe & Nigam, 2008).

Vortex type	U (m/s)	L_h (km)	N $(1/s)$	$f.10^{-4}$ $(1/s)$	$\tilde{f}.10^{-4}$ $(1/s)$	F_h	Ro	$\widetilde{Ro}$
Dust devils	5-15	0.005-0.002	0.01	1	1	50-600	2000-30000	2000-30000
Tornadoes	30-150	0.01-1	0.01	1	1	6-300	300-15000	300-15000
Tropical cyclones	20-80	15-100	0.01	0.2-0.5	1.4	0.04-1	1-250	1-40
Polar lows	20-40	10-100	0.01	1	1	0.04-0.8	1-40	1-40
Supercell mesocyclones	5-15	5-15	0.01	1	1	0.06-0.6	1-30	1-30
Island wake vortices	5-10	10-20	0.01	0.2-1	1-1.5	0.05-0.2	1-25	1-5
Synoptic-scale cyclones	10-30	500-1000	0.01	1	1	0.002-0.01	0.1-0.6	0.1-0.6
Oceanic eddies	1-2	50-150	0.01	1	1	0.001-0.01	0.05-0.5	0.05-0.5
Circumpolar vortex	50-100	3000	0.02-0.03	1	1	0.001-0.005	0.2-0.3	0.2-0.3

Table 1.1: Estimated physical parameters of atmospheric vortices and oceanic eddies reported by Schecter & Montgomery (2006). The corresponding horizontal Froude number F_h, traditional Rossby number Ro and non-traditional Rossby number $\widetilde{Ro}$ are also indicated. For non-tropical vortices, the traditional Coriolis parameter and non-traditional Coriolis parameters are taken at mid-latitude $\phi = 45°$.

Maslowe & Nigam (2008) argue that non-linear effects have a greater theoretical significance in smoothing critical layers than viscous effects. Caillol (2012) has studied the existence of critical layers in a rapidly rotating vortex. He shows the creation of secondary vortices at the critical radius that rotates around the basic vortex axis.

1.5.2 Baroclinic critical layers

A baroclinic critical layer is another type of critical layer found in stratified flows. Consider a horizontal shear flow $U_x(y)$ in a stratified fluid with a Brunt–Väisälä frequency N. For perturbations with a wavenumber k_x and a frequency ω, a baroclinic critical layer occurs at the position $y = y_c$ where $\omega + k_x U_x(y) = \pm N$. Wang & Balmforth (2020, 2021) have studied analytically the dynamics of forced baroclinic critical layers in horizontal shear flows $U_x = \Lambda y$ (figure 1.6 (*a*)). A wavemaker at $y = 0$ constantly generates perturbations with zero frequency and wavenumbers k_x and k_z. The baroclinic critical layers are then located at $k_x \Lambda y = \pm N$. They derived analytical solutions applying to two distinct time ranges: at early times, they provide an unsteady linear solution near the critical layer connected to a steady solution far from it. The former solution grows and thins over time. At late times, they have derived a reduced model taking into account non-linear effects which describes the mean-flow responses. To study secondary two-dimensional instabilities of the solutions, small perturbations are added to both linear and non-linear reduced models. Wang & Balmforth (2021) have shown that the mechanism of the instability is based on the formation of inflectional points induced by the critical layers to the mean flow. During the saturation stage of the instability, a coherent vortex appears near the critical layer (figure 1.6 (*b*)). In addition, the instability is self-replicating. The coherent vortex excites a new quasi-steady wave by acting as a wavemaker. New critical layers are then created by this new wave (figure 1.6 (*b*)). Subsequently, vortices form at the new critical layers, and so on.

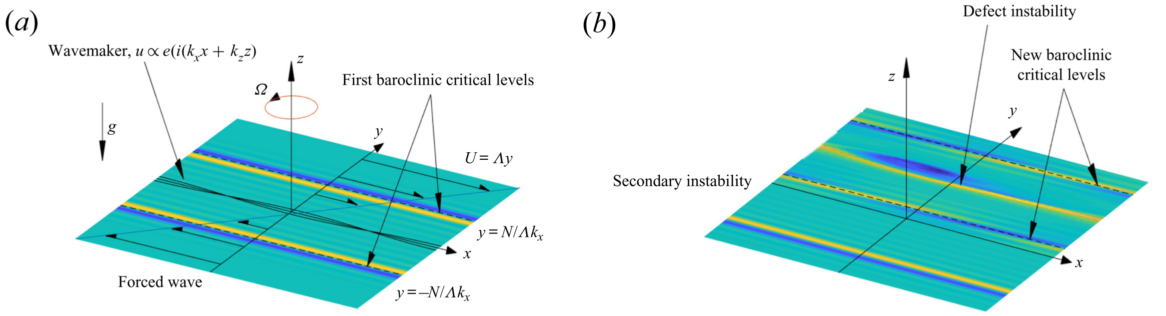

Fig. 1.6: (*a*) The model studied by Wang & Balmforth (2020, 2021). The wavemaker is located at $y = 0$, forcing the baroclinic critical levels at $k_x \Lambda y = \pm N$. (*b*) A secondary instability creates a coherent vortical structure that excites a new wave with a different phase speed. The new wave then forces a new set of baroclinic critical levels. Source: Wang & Balmforth (2021).

In the case of a vortex with angular velocity Ω, baroclinic critical layers can also exist when $\omega + m\Omega = \pm N$ for a perturbation with an azimuthal mode m and frequency

ω. Boulanger *et al.* (2007, 2008) have experimentally studied an inclined vortex in a stratified fluid. Because the vortex axis is tilted with respect to gravity forces, a steady perturbation with azimuthal mode $m = 1$ is imposed to the vortex. A baroclinic critical layer then develops at the radius where $\Omega = N$ (the frequency of the perturbation is zero). Near the critical layer, an intense axial flow and strong density variations are observed (figure 1.7 (a, b)). For a sufficiently large Reynolds number, the critical layer deforms into several vortices with a zig-zag structure (figure 1.7 (c, d, e, f)). They are due to a three-dimensional shear instability caused by the strong shear of the axial velocity. In a theoretical study, they smoothed the singularity by introducing viscous effects and provided an expression for the axial flow (Boulanger *et al.*, 2007). The theoretical expressions of the axial flow were used to perform a stability analysis and a good agreement was found with the experimental results (Boulanger *et al.*, 2008).

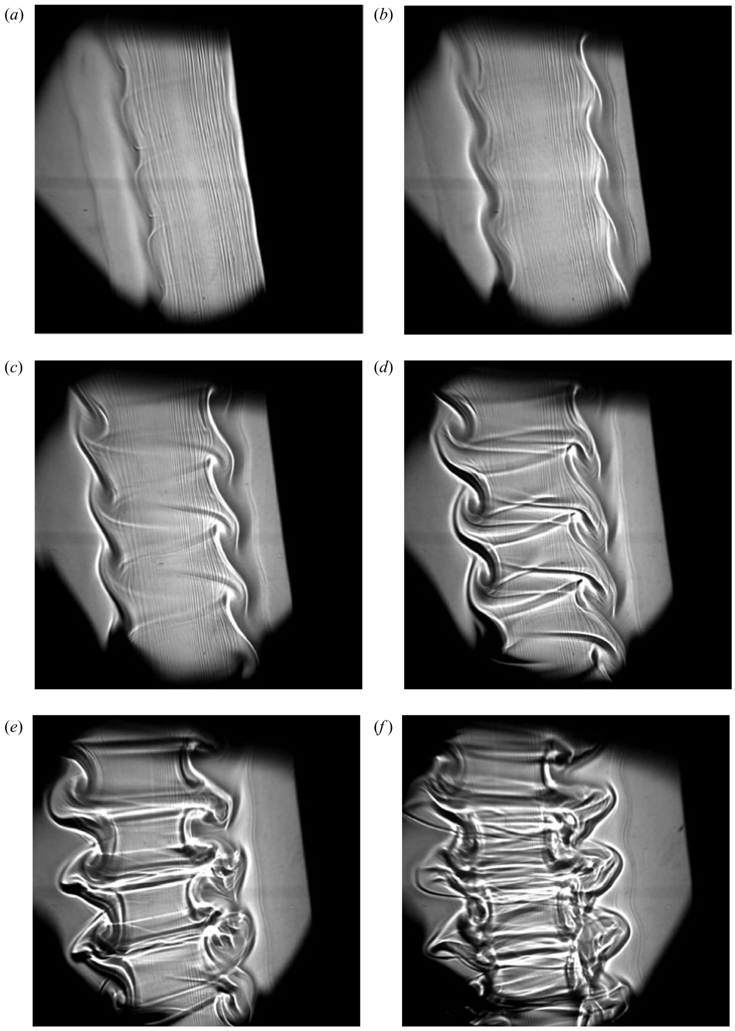

Fig. 1.7: Shadowgraph sequence of the vortex in a vertical longitudinal plane. The time interval is 1.1 rotation period. The parameters are: Froude number $F = 3$, Reynolds number $Re = 720$ and inclination angle $\alpha = 0.07$ rad. Source: Boulanger *et al.* (2008).

1.6 Goals of the dissertation

In this thesis, we study the evolution of a vortex in a stratified rotating fluid under the complete Coriolis force, i.e. in the presence of background rotation in both vertical and horizontal directions. In our review, we have demonstrated that considering the complete Coriolis force might be essential for flows with non-negligible vertical motion or weakly stratified fluids. Instabilities are triggered, modified, or enhanced, and wave dynamics are changed due to the non-traditional Coriolis force. However, little is known about its effect on vortices. In order to tackle this problem, we have conducted direct numerical simulations (DNS) of a single vertical stratified vortex under the complete Coriolis force. These simulations are accompanied by asymptotic analyses for a small non-traditional Coriolis parameter in order to understand the dynamics.

In this configuration, the buoyancy force is misaligned with the rotation vector similarly as the tilted stratified vortex studied by Boulanger *et al.* (2007, 2008) where the resulting strong shear of the vertical velocity in the critical layer leads to a three-dimensional instability (figure 1.7). The present DNS also shows a critical layer appearing at a radius where the angular velocity of the vortex is equal to the Brunt–Väisälä frequency. However, two types of instability will be shown to develop: a two-dimensional and a three-dimensional instabilities.

In order to understand the mechanism of both instabilities, the competition between them, as well as the evolution of the critical layer, asymptotic analyses have been performed for large non-traditional Rossby numbers (based on the horizontal component of the background rotation) and large Reynolds numbers. They also demonstrate the similarity between the evolution of the critical layer in this thesis and the critical layers studied in Boulanger *et al.* (2007, 2008) and Wang & Balmforth (2020, 2021).

Chapter 2 gives initial conditions and governing equations as well as a brief explanation of the numerical methods that have been used. In chapter 3, we study the stratified vortex under the complete Coriolis force with a purely two-dimensional initial conditions. The evolution of the vortex with slightly three-dimensional initial conditions will be presented in chapter 4. Finally, conclusions as well as perspectives are discussed in chapter 5.

Chapter 2

Numerical methods

To perform direct numerical simulations (DNS), we have used the numerical code NS3D (Deloncle *et al.*, 2008; Deloncle, 2014) based on the pseudo-spectral method. As the numerical code NS3D originally only considered a vertical background rotation, we have modified it to perform a simulation under the complete Coriolis force, i.e. with a horizontal and vertical background rotation. In this chapter, we first provide initial conditions and governing equations. Following this, we will construct the spectral form of the non-dimensional governing equations and discuss the boundary conditions, as well as space and time discretizations, used in the numerical code.

2.1 Initial simulations

Figure 2.1 illustrates the geometry of simulations. At the center of the box with dimensions of $l_x \times l_y \times l_z$, a single Lamb-Oseen stratified vortex is located with a vorticity field

$$\boldsymbol{\omega}(\boldsymbol{x}, t=0) = \zeta_0 \boldsymbol{e_z} = \frac{\Gamma}{\pi a_0^2} e^{-r^2/a_0^2} \boldsymbol{e_z}, \tag{2.1}$$

where Γ is the circulation, a_0 is the radius. Here, $\boldsymbol{x} = (x, y, z)$ and (r, θ, z) are Cartesian and cylindrical coordinates, respectively, and $(\boldsymbol{e_x}, \boldsymbol{e_y}, \boldsymbol{e_z})$ and $(\boldsymbol{e_r}, \boldsymbol{e_\theta}, \boldsymbol{e_z})$ are the associated unit vectors. The vortex is subjected to a background rotation vector $\boldsymbol{\Omega_b}$ that is decomposed into two vertical and horizontal components: $2\boldsymbol{\Omega_b} = \tilde{f}\boldsymbol{e_y} + f\boldsymbol{e_z}$ where $f = 2\Omega_b \sin(\phi)$ and $\tilde{f} = 2\Omega_b \cos(\phi)$, where ϕ is the angle between the background rotation vector and the unit vector in the y direction, $\boldsymbol{e}_y$. The fluid is stably stratified with a constant Brunt–Väisälä frequency $N = \sqrt{-(g/\rho_0)\partial\bar{\rho}/\partial z}$, where g is the gravity, ρ_0 a constant reference density and $\bar{\rho}(z)$ the mean density profile.

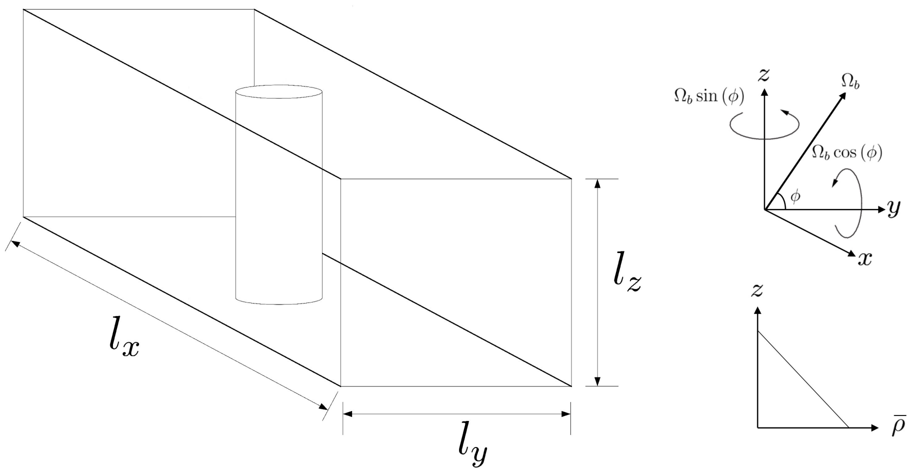

Fig. 2.1: Sketch of the initial vortex in a stratified rotating fluid with a background rotation Ω_b inclined with an angle ϕ

2.2 Governing equations

2.2.1 Dimensional form

The incompressible Navier-Stokes equations under the Boussinesq approximation govern the dynamics

$$\boldsymbol{\nabla}\boldsymbol{.}\boldsymbol{u} = 0, \tag{2.2}$$

$$\frac{\partial \boldsymbol{u}}{\partial t} = \boldsymbol{u} \times \boldsymbol{\omega} - \boldsymbol{\nabla}\left(\frac{p}{\rho_0} + \frac{\boldsymbol{u}^2}{2}\right) + b\boldsymbol{e_z} - 2\boldsymbol{\Omega_b} \times \boldsymbol{u} + \nu \boldsymbol{\nabla}^2 \boldsymbol{u}, \tag{2.3}$$

$$\frac{\partial b}{\partial t} + \boldsymbol{u}\boldsymbol{.}\boldsymbol{\nabla} b + N^2 u_z = \kappa \nabla^2 b, \tag{2.4}$$

where $\boldsymbol{u} = (u_x, u_y, u_z)$, b and p are the velocity, buoyancy and pressure, respectively. The buoyancy is $b = -g\rho/\rho_0$ where g is the gravity, ρ is the density perturbation related to the total density field ρ_t via $\rho_t(\boldsymbol{x}, t) = \rho_0 + \bar{\rho}(z) + \rho(x, t)$. Finally, ν and κ are the viscosity of the fluid and the diffusivity of the stratifying agent, respectively.

2.2.2 Non-dimensionalization and control parameters

The governing equations are non-dimensionalized by using $2\pi a_0^2/\Gamma$ and a_0 as time and length units:

$$\boldsymbol{\nabla}\boldsymbol{.}\boldsymbol{u} = 0, \tag{2.5}$$

$$\frac{\partial \boldsymbol{u}}{\partial t} = \boldsymbol{u} \times \boldsymbol{\omega} - \boldsymbol{\nabla}\left(\frac{p}{\rho_0} + \frac{\boldsymbol{u}^2}{2}\right) + b\boldsymbol{e_z} - 2\left(\frac{1}{Ro}\boldsymbol{e_z} + \frac{1}{\widetilde{Ro}}\boldsymbol{e_y}\right) \times \boldsymbol{u} + \frac{1}{Re}\boldsymbol{\nabla}^2 \boldsymbol{u}, \tag{2.6}$$

$$\frac{\partial b}{\partial t} + \boldsymbol{u}\boldsymbol{.}\boldsymbol{\nabla} b + \frac{1}{F_h^2} u_z = \frac{1}{ReSc} \nabla^2 b, \tag{2.7}$$

where the same notation has been kept for the non-dimensional variables. In the following, all results will be reported in non-dimensional form. The problem is controlled by five non-dimensional numbers: the Reynolds, Froude, traditional and non-traditional Rossby and Schmidt numbers

$$Re = \frac{\Gamma}{2\pi\nu}, \qquad F_h = \frac{\Gamma}{2\pi a_0^2 N}, \qquad Ro = \frac{\Gamma}{\pi a_0^2 f}, \qquad \widetilde{Ro} = \frac{\Gamma}{\pi a_0^2 \tilde{f}}, \qquad Sc = \frac{\nu}{\kappa}. \tag{2.8}$$

The traditional Rossby number Ro and non-traditional Rossby number $\widetilde{Ro}$ are defined with the vertical and horizontal components of the rotation vector, respectively. The Schmidt number will be always set to unity.

2.3 Direct Numerical Simulations

2.3.1 Spectral form of the governing equations

The spectral form of the equations is built by applying a three-dimensional Fourier transform to (2.2-2.4). The three-dimensional Fourier transform of a periodic quantity q is defined as

$$\hat{q}(\boldsymbol{k}, t) = \int_0^{l_z} \int_0^{l_y} \int_0^{l_x} q(\boldsymbol{x}, t) e^{-i\boldsymbol{k}.\boldsymbol{x}} \mathrm{d}\boldsymbol{x}, \tag{2.9}$$

where $\hat{q}$ is the three-dimensional Fourier transform of q and $\boldsymbol{k} = (k_x, k_y, k_z)$ is the total wavenumber. Considering the periodicity of quantities, applying the three-dimensional Fourier transform to (2.5) then gives

$$\boldsymbol{k}.\hat{\boldsymbol{u}} = 0. \tag{2.10}$$

It shows the orthogonality of the velocity field and wave vector in spectral space. Similarly, the spectral form of (2.3) is given by

$$\left[\frac{\partial}{\partial t} + \frac{1}{Re}\|\boldsymbol{k}\|^2\right] \hat{\boldsymbol{u}} = \widehat{\boldsymbol{u} \times \boldsymbol{\omega}} + i\boldsymbol{k}\left(\widehat{\frac{p}{\rho_0} + \frac{\boldsymbol{u}^2}{2}}\right) - 2\left(\frac{1}{Ro}\boldsymbol{e_z} + \frac{1}{\widetilde{Ro}}\boldsymbol{e_y}\right) \times \hat{\boldsymbol{u}} + \hat{b}\boldsymbol{e_z}. \tag{2.11}$$

Using the tensor $\mathcal{P}_\perp$

$$\mathcal{P}_\perp(\boldsymbol{k}) = \left[\delta_{mn} - \frac{k_m k_n}{\|\boldsymbol{k}\|^2}\right]_{1 \leqslant m,n \leqslant 3}, \tag{2.12}$$

where δ_{mn} is the Kronecker delta, we then project (2.11) on the space of solenoidal fields $\mathcal{D}(\boldsymbol{e_k}^\perp)$ where $\boldsymbol{e_k} = \boldsymbol{k}/\|\boldsymbol{k}\|$ is the unit wave vector

$$\frac{\partial \hat{\boldsymbol{u}} e^{\boldsymbol{k}^2 t/Re}}{\partial t} = \mathcal{P}_\perp\left(\widehat{\boldsymbol{u} \times \boldsymbol{\omega}} - 2\left(\frac{1}{Ro}\boldsymbol{e_z} + \frac{1}{\widetilde{Ro}}\boldsymbol{e_y}\right) \times \hat{\boldsymbol{u}} + \hat{b}\boldsymbol{e_z}\right) e^{\boldsymbol{k}^2 t/Re}. \tag{2.13}$$

In (2.13), the orthogonality of the velocity field and wave vector has been enforced. Note that the pressure p is absent in (2.13) due to the projection on the space of solenoidal fields. Similarly, the spectral form of (2.4) is derived by applying the three-dimensional Fourier transform to (2.4):

$$\left[\frac{\partial}{\partial t} + \frac{1}{ReSc}\|\boldsymbol{k}\|^2\right] \hat{b} = -i\boldsymbol{k}.\widehat{b\boldsymbol{u}} - N^2 u_z, \tag{2.14}$$

which is equivalent to

$$\frac{\partial \hat{b} e^{\boldsymbol{k}^2 t/(ReSc)}}{\partial t} = \left[-i\boldsymbol{k}.\widehat{b\boldsymbol{u}} - N^2 u_z \right] e^{\boldsymbol{k}^2 t/(ReSc)}. \tag{2.15}$$

2.3.2 Boundary conditions

As mentioned earlier, periodic boundary conditions are implemented in NS3D. According to Pradeep & Hussain (2004), the periodicity of a domain can result in nonphysical results and must be implemented cautiously. When a single vortex is simulated, a strain field is induced due to the periodicity of the domain. In addition, periodic boundary conditions imply a zero net circulation of the domain, whereas a single vortex has a non-zero net circulation. This implies that the initial condition is not exactly $\omega(\boldsymbol{x}, t = 0)$ as defined in (2.1) but $\omega'(\boldsymbol{x}, t = 0) = \omega(\boldsymbol{x}, t = 0) - \Gamma/(l_x l_y)$ where the artificial background vorticity $\Gamma/(l_x l_y)$ makes the net circulation zero. It is therefore necessary to have a sufficiently large domain in order to minimize these effects of periodicity. As shown by Bonnici (2018), with a horizontal domain of $l_x = l_y = 18$, the artificial background vorticity $\Gamma/(l_x l_y)$ represents only 1% of the maximum vortex vorticity. The strain field due to the image vortices is also very small. Therefore, all simulations reported throughout this thesis are carried out with a horizontal domain of $l_x = l_y = 18$.

2.3.3 Space and time discretizations

We use Cartesian coordinates $\boldsymbol{x} = (x, y, z)$ to discretize the physical space with the resolution $N_x \times N_y \times N_z$. Similarly, the spectral coordinates $\boldsymbol{k} = (k_x, k_y, k_z)$ are discretized with the same resolution. In view of the fact that dissipation requires small scales to be resolved, the resolution needed to resolve small scale depends on the Reynolds number. The maximum resolution, however, will be limited by computational costs. Consequently, several tests are required to confirm that the resolution is suitable while the computational cost is reasonable. For example, in the case of two-dimensional simulations, the velocity field has been found to differ by less than 0.1 % when the horizontal resolution is doubled from $N_x = N_y = 512$ to $N_x = N_y = 1024$ for $Re = 2000$.

Time integration is performed using the fourth-order Runge-Kutta method. In this method, the initial value problem

$$\frac{\partial q}{\partial t} = f(q, t), \qquad q(t_0) = q_0, \tag{2.16}$$

is discretized in time by the approximation

$$q(t_{n+1}) = q(t_n) + \frac{1}{6}\left(k_1 + 2k_2 + 2k_3 + k_4\right)\delta_t, \tag{2.17}$$

where δ_t is the time step $t_{n+1} = t_n + \delta_t$ and

$$\begin{aligned} k_1 =& f(q(t_n), t_n), \\ k_2 =& f(q(t_n) + k_1\frac{\delta_t}{2}, t_n + \frac{\delta_t}{2}), \\ k_3 =& f(q(t_n) + k_2\frac{\delta_t}{2}, t_n + \frac{\delta_t}{2}), \\ k_4 =& f(q(t_n) + k_3\delta_t, t_n + \delta_t). \end{aligned} \tag{2.18}$$

Since the Runge-Kutta method is an explicit method, the time step δ_t must satisfy the Courant–Friedrichs–Levy (CFL) convergence condition

$$\delta_t \left(\frac{u_x}{\delta_x} + \frac{u_y}{\delta_y} + \frac{u_z}{\delta_z} \right) \leq C, \tag{2.19}$$

where $(\delta_x, \delta_y, \delta_z) = (l_x/N_x, l_y/N_y, l_z/N_z)$ and $C = 1$ is the Courant number. For example, the time step is $\delta_t = 0.01$ for the resolution $N_x = N_y = 512$ in accordance with other parameters in (2.19). For the resolutions, the time step is modified so as to satisfy (2.19).

2.3.4 Pseudo-spectral method

Using the fourth-order Runge-Kutta, equations (2.13) and (2.15) are integrated in time. Computations of the non-linear terms $\widehat{\boldsymbol{u} \times \boldsymbol{\omega}}$ and $\widehat{b\boldsymbol{u}}$ in spectral space are, however, highly expensive in the spectral method. In the so-called pseudo-spectral method, a backward Fourier transform of the terms $(\hat{\boldsymbol{u}}, \hat{\boldsymbol{\omega}}, \hat{b})$ is performed, then non-linear terms are computed in physical space and finally, a forward Fourier transform is applied to the non-linear terms. In spite of the lower computation cost of the pseudo-spectral method, computations of non-linear terms lead to an aliasing error, which is the transposition of higher-order terms into lower-order terms because of the periodicity of the quantities (Orszag, 1971; Delbende, 1998). To get rid of aliasing errors, the top one-third of the modes along each direction is removed.

Chapter 3

Two-dimensional evolution of the vortex

Dynamics of a stratified vortex under the complete Coriolis force: two-dimensional three-components evolution

Iman Toghraei[1], and Paul Billant[1]
[1]LadHyX, CNRS, École polytechnique, Institut Polytechnique de Paris, 91120 Palaiseau, France

(Published in *J. Fluid Mech.* (2022), 950, A29)

Abstract: We study the dynamics of an initially axisymmetric and vertical Lamb-Oseen vortex in a stratified-rotating fluid under the complete Coriolis force on the f plane, i.e. in presence of a background rotation both along the vertical and horizontal directions. By a combination of direct numerical simulations and asymptotic analyses for small horizontal background rotation, we show that a critical layer appears at the radius where the angular velocity of the vortex is equal to the buoyancy frequency when the Froude number is larger than unity. This critical layer generates a vertical velocity which is invariant along the vertical and which first increases linearly with time and then saturates at an amplitude scaling like $Re^{1/3}$, where Re is the Reynolds number. In turn, a quasi-axisymmetric anomaly of vertical vorticity is produced at the critical radius through the non-traditional Coriolis force. Below a critical non-traditional Rossby number $\widetilde{Ro}$ (based on the horizontal component of the background rotation) depending on Re, the Rayleigh's inflectional criterion is satisfied and a shear instability is subsequently triggered rendering the vertical vorticity fully non-axisymmetric. The decay of the angular velocity is then enhanced until it is everywhere lower than the buoyancy frequency. A theoretical criterion derived from the Rayleigh condition predicts well the instability. It shows that this phenomenon can occur even for a large non-traditional Rossby number $\widetilde{Ro}$ for large Re. Hence, the non-traditional Coriolis force might have much more impact on geophysical vortices than anticipated by considering the order of magnitude of $\widetilde{Ro}$.

3.1 Introduction

The Coriolis force due to the planetary rotation is an essential ingredient of geophysical fluid dynamics. When studying its effect on fluid motions, it is common to use the so-called traditional approximation which amounts to take into account only the vertical component, $\Omega_b \sin(\phi)$, of the planetary angular velocity vector $\boldsymbol{\Omega_b}$ at a given latitude ϕ. Its horizontal component $\Omega_b \cos(\phi)$ is neglected mainly because the associated Coriolis force (called non-traditional Coriolis force) involves vertical motions or appears in the vertical momentum equation, whereas geophysical flows are usually in hydrostatic balance with weak vertical motions compared to horizontal motions (Gerkema *et al.*, 2008).

However, Gerkema *et al.* (2008) have reviewed several circumstances where the effect of the non-traditional Coriolis force becomes non-negligible. This occurs for example when the vertical velocity is not small like for the instability of Ekman layers (Wippermann, 1969; Etling, 1971) and for deep convection (Sheremet, 2004). In the latter case, its effect is particularly intuitive since convective cells become slanted along the axis of rotation instead of the direction of gravity. The non-traditional Coriolis force may have also many effects on equatorial flows (Hayashi & Itoh, 2012; Igel & Biello, 2020) and on the propagation and frequency range of internal waves, especially when the stratification is weak (Gerkema *et al.*, 2008). Recently, the non-traditional force has been shown to significantly modify several instabilities: the inertial instability (Tort *et al.*, 2016; Kloosterziel *et al.*, 2017), the symmetric instability (Zeitlin, 2018) and the shear instability (Park *et al.*, 2021). Tort & Dubos (2014) and Tort *et al.* (2014) have also derived shallow water models taking into account the complete Coriolis force.

In the case of vortices, Lavrovskii *et al.* (2000) and Semenova & Slezkin (2003) have shown analytically that the equilibrium shape of a meddy-like anticyclonic vortex in a stratified fluid is slightly tilted with respect to the horizontal in presence of the full Coriolis force. However, they have assumed that the vortex has a uniform vorticity and is embedded within a fluid a rest. Hence, there exist both a discontinuity of vorticity and velocity at the vortex boundary. Here, we study numerically and theoretically the evolution of a vortex with a continuous distribution of vorticity under the complete Coriolis force. The vortex is initially axisymmetric and columnar with a vertical axis in a stratified-rotating fluid under the Boussinesq and f-plane approximations. Since there is a misalignment between the buoyancy force and the rotation vector, this configuration is somewhat similar to the tilted vortex in a stratified non-rotating fluid considered by Boulanger *et al.* (2007, 2008). They have shown that a critical layer develops at the radius where the angular velocity of the vortex is equal to the Brunt–Väisälä frequency. Near this critical layer, they observed an intense axial flow and strong density variations that are uniform along the vortex axis but that lead to a three-dimensional shear instability under certain circumstances. We will show that a similar critical layer develops in the present configuration when the Froude number is larger than unity. For some parameters, an instability will be also triggered but it will be two-dimensional instead of being three-dimensional and due to a different mechanism. In addition, we will show that the critical layer evolution contains two different regimes: first, an unsteady inviscid phase followed by a second viscous phase which can be steady or can evolve non-linearly depending on the parameters. Such evolution is similar to the one evidenced by Wang & Balmforth (2020, 2021) in their studies of forced baroclinic critical layers. They have also reported the subsequent development of a two-dimensional shear instability and studied its non-linear evolution by means of a reduced model. Our investigations are based on direct numerical simulations coupled to asymptotic analyses of the critical layer in the limit of small non-traditional Coriolis parameter following the lines of Boulanger *et al.* (2007, 2008); Wang & Balmforth (2020, 2021).

As a preliminary remark, we stress that the present study has been first carried out by means of three-dimensional numerical simulations. However, the flow turned out to remain independent of the vertical coordinate although the vertical velocity is non-zero. In other words, the dynamics were two-dimensional but with 3 components of velocity (2D3C). As we will see later, this can be easily understood from the governing equations. For this reason, the subsequent simulations reported in this paper have been restricted to a two-dimensional configuration. However, in a future paper, we will show that the introduction of infinitely small three-dimensional perturbations may also lead for some parameters to a full three-dimensionalisation of the vortex, i.e. a 3D3C dynamics, via an axial shear instability similar to the one reported by Boulanger *et al.* (2007, 2008). We stress that the two-dimensional dynamics is still observed in this full three-dimensional configuration in a significant range of the parameters space.

The paper is organized as follows. The problem is first formulated in §3.2. Direct numerical simulations are described in §3.3. Asymptotic analyses are conducted for small non-traditional Coriolis parameter in §3.4. In §3.5, the numerical and asymptotic results are compared. The origin of the full non-axisymmetric dynamics of the vortex will be investigated in §3.6. Finally, the late evolution is discussed in §3.7 and the conclusions are given in §3.8.

3.2 Formulation of the problem

3.2.1 Governing equations

We use the incompressible Navier-Stokes equations under the Boussinesq approximation

$$\boldsymbol{\nabla}\boldsymbol{.}\boldsymbol{u} = 0, \tag{3.1}$$

$$\frac{\partial \boldsymbol{u}}{\partial t} + (\boldsymbol{u}\boldsymbol{.}\boldsymbol{\nabla})\,\boldsymbol{u} = -\boldsymbol{\nabla}\left(\frac{p}{\rho_0}\right) + b\boldsymbol{e_z} - 2\boldsymbol{\Omega_b} \times \boldsymbol{u} + \nu \boldsymbol{\nabla}^2 \boldsymbol{u}, \tag{3.2}$$

$$\frac{\partial b}{\partial t} + \boldsymbol{u}\boldsymbol{.}\boldsymbol{\nabla} b + N^2 u_z = \kappa \nabla^2 b, \tag{3.3}$$

where $\boldsymbol{u}$ is the velocity field, p is the pressure and $b = -g\rho/\rho_0$ is the buoyancy, g is the gravity, ρ is the density perturbation and ρ_0 is a constant reference density. $\boldsymbol{e_z}$ is the vertical unit vector and $\boldsymbol{\Omega_b}$ is the background rotation vector. It is assumed to have not only a vertical component but also a horizontal component along the y direction: $2\boldsymbol{\Omega_b} = \tilde{f}\boldsymbol{e_y} + f\boldsymbol{e_z}$ where $f = 2\Omega_b \sin(\phi)$ and $\tilde{f} = 2\Omega_b \cos(\phi)$, where ϕ is the latitude or, equivalently, the angle between the background rotation vector and the unit vector in the y direction, $\boldsymbol{e}_y$ (figure 3.1). ν and κ are the viscosity of the fluid and diffusivity of the stratifying agent, respectively. The total density field ρ_t reads $\rho_t(\boldsymbol{x}, t) = \rho_0 + \bar{\rho}(z) + \rho(x, t)$, where $\bar{\rho}$ is the mean density profile along the z-axis. The Brunt–Väisälä frequency

$$N = \sqrt{-\frac{g}{\rho_0}\frac{\mathrm{d}\bar{\rho}}{\mathrm{d}z}} \tag{3.4}$$

will be assumed to be constant.

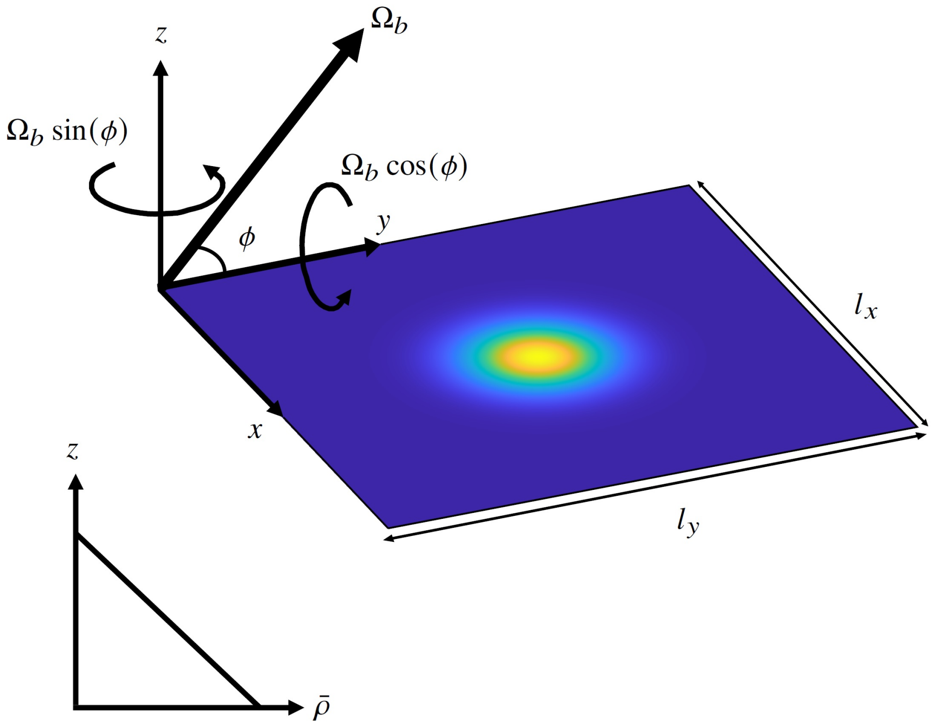

Fig. 3.1: Sketch of the initial vortex in a stratified fluid and in presence of a background rotation Ω_b inclined with an angle ϕ.

3.2.2 Initial conditions

A single vertical vortex with a Lamb-Oseen profile is taken as initial conditions. Its vorticity field reads

$$\boldsymbol{\omega}(\boldsymbol{x}, t=0) = \zeta \boldsymbol{e_z} = \frac{\Gamma}{\pi a_0^2} e^{-r^2/a_0^2} \boldsymbol{e_z}, \tag{3.5}$$

where Γ is the circulation, a_0 is the radius and r is the radial coordinate. The geometry of the flow is sketched in figure 3.1.

3.2.3 Non-dimensionalization

Equations (3.1-3.3) are non-dimensionalized by using $2\pi a_0^2/\Gamma$ and a_0 as time and length units:

$$\boldsymbol{\nabla . u} = 0, \tag{3.6}$$

$$\frac{\partial \boldsymbol{u}}{\partial t} + (\boldsymbol{u}.\boldsymbol{\nabla})\,\boldsymbol{u} = -\boldsymbol{\nabla} p + b\boldsymbol{e_z} - 2\left(\frac{1}{Ro}\boldsymbol{e_z} + \frac{1}{\widetilde{Ro}}\boldsymbol{e_y}\right) \times \boldsymbol{u} + \frac{1}{Re}\boldsymbol{\nabla}^2 \boldsymbol{u}, \tag{3.7}$$

$$\frac{\partial b}{\partial t} + \boldsymbol{u}.\boldsymbol{\nabla} b + \frac{1}{F_h^2} u_z = \frac{1}{ReSc} \nabla^2 b, \tag{3.8}$$

where the same notation has been kept for the non-dimensional variables. Note that ρ_0 has been eliminated by redefining the pressure p. The Reynolds, Froude, Rossby and Schmidt numbers are defined as

$$Re = \frac{\Gamma}{2\pi\nu}, \qquad F_h = \frac{\Gamma}{2\pi a_0^2 N}, \qquad Ro = \frac{\Gamma}{\pi a_0^2 f}, \qquad \widetilde{Ro} = \frac{\Gamma}{\pi a_0^2 \tilde{f}}, \qquad Sc = \frac{\nu}{\kappa}. \tag{3.9}$$

Note that two Rossby numbers Ro and $\widetilde{Ro}$ are defined based on the two components of the rotation vector. The Schmidt number will be always set to unity. In the following, all results will be reported in non-dimensional form.

3.2.4 Numerical method

A pseudo-spectral method with periodic boundary conditions is used to integrate the equations (3.1-3.3) in space (Deloncle *et al.*, 2008). Time integration is performed with a fourth-order Runge–Kutta scheme. Most of the aliasing is removed by truncating the top one third of the modes along each direction. The viscous and diffusive terms are integrated exactly. The horizontal sizes of the computational domain have been set to $l_x = l_y = 18$. As shown by Bonnici (2018) and Billant & Bonnici (2020), this is sufficiently large to minimize the effects of the periodic boundary conditions and to give results independent of the box sizes. In particular, the periodic boundary condition imposes that the net circulation over the domain is zero implying that the initial vorticity is not exactly (3.5) but $\zeta' = \zeta - \Gamma/(l_x l_y)$. However, with $l_x = l_y = 18$, the artificial background vorticity $\Gamma/(l_x l_y)$ is weak and represents only 1% of the maximum vorticity of the vortex. The horizontal resolution has been varied from $n_x = n_y = 512$ for $Re = 2000$ up to $n_x = n_y = 1024$ for $Re = 10000$. As mentioned in the introduction, preliminary simulations were fully three-dimensional with a resolution n_z and a vertical size l_z similar to the horizontal ones. However, the flow were always observed to remain independent of the vertical coordinate. It can be seen indeed from (3.6-3.8) that if $\partial/\partial z = 0$ at $t = 0$, then the flow will remain independent of the vertical coordinate for all time. Therefore, only two-dimensional simulations but with 3 components of velocity will be presented in the following. Several tests using different horizontal resolutions have been performed in order to verify the accuracy of the computations. For $Re = 2000$, the velocity has been found to differ by less than 0.1% when the resolution is increased from 512×512 to 1024×1024. Similarly, for $Re = 10000$, the relative variation of the velocity is less than 0.5% when the resolution is increased from 1024×1024 to 1536×1536.

3.3 Direct Numerical Simulations

3.3.1 Illustrative example of the vortex dynamic

To get an overview of the effect of the complete Coriolis force, we start by presenting the vortex evolution for the sample set of parameters $Re = 2000$, $F_h = 10$, $Ro = 23.1$, $\phi = 60°$ ($\widetilde{Ro} = 40$). Figures 3.2 and 3.3 show the evolution of the vertical velocity and vertical vorticity at six different times (A movie is available in the supplementary

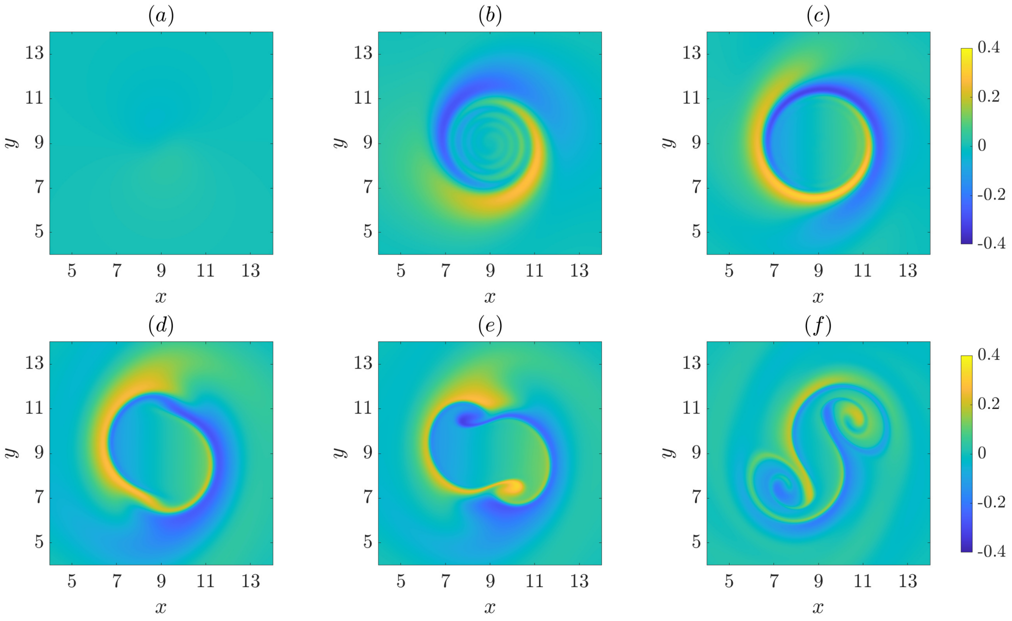

Fig. 3.2: Vertical velocity at different times: (a) $t = 1$, (b) $t = 30$, (c) $t = 60$, (d) $t = 75$, (e) $t = 80$ and (f) $t = 90$ for $Re = 2000$, $F_h = 10$, $Ro = 23.1$, $\phi = 60°$ $(\widetilde{Ro} = 40)$.

material). Initially, the vortex is completely axisymmetric (figure 3.3(a)) and the vertical velocity is zero (figure 3.2(a)). As time goes on, a vertical velocity field with an azimuthal wavenumber $m = 1$ develops (figure 3.2(b)). This structure tends to intensify and becomes more and more concentrated at a particular radius (figure 3.2(c)). Concomitantly, a ring of negative vertical vorticity appears and grows at the same radius (figure 3.3(b, c)). Later, the vertical velocity structure and the ring of anomalous vertical vorticity are no longer perfectly circular (figure 3.3(d, e, f)). Two negative vortices appear on the vertical vorticity ring and revolve around the vortex center (figure 3.3(e, f)). Simultaneously, the shape of the vertical velocity structure is deformed similarly (figure 3.2(e, f)). As already mentioned, preliminary three-dimensional simulations with various vertical sizes l_z of the computational domain and resolutions n_z have shown that the velocity and vorticity fields remain always completely independent of the vertical coordinate, i.e. the same evolution is observed in any horizontal cross-section. It is also important to stress that this phenomenon occurs only in presence of the complete Coriolis force. Indeed, if $\widetilde{Ro} = \infty$, the vertical velocity remains identically zero while the vertical vorticity simply decays by viscous diffusion.

From figure 3.3, we can distinguish two phases in the evolution of the vortex. First, a circular ring of anomalous vertical vorticity develops and then, this ring becomes non-axisymmetric. A more in-depth analysis of these two phases will be discussed later. Let us first examine the effects of the control parameters on this phenomenon.

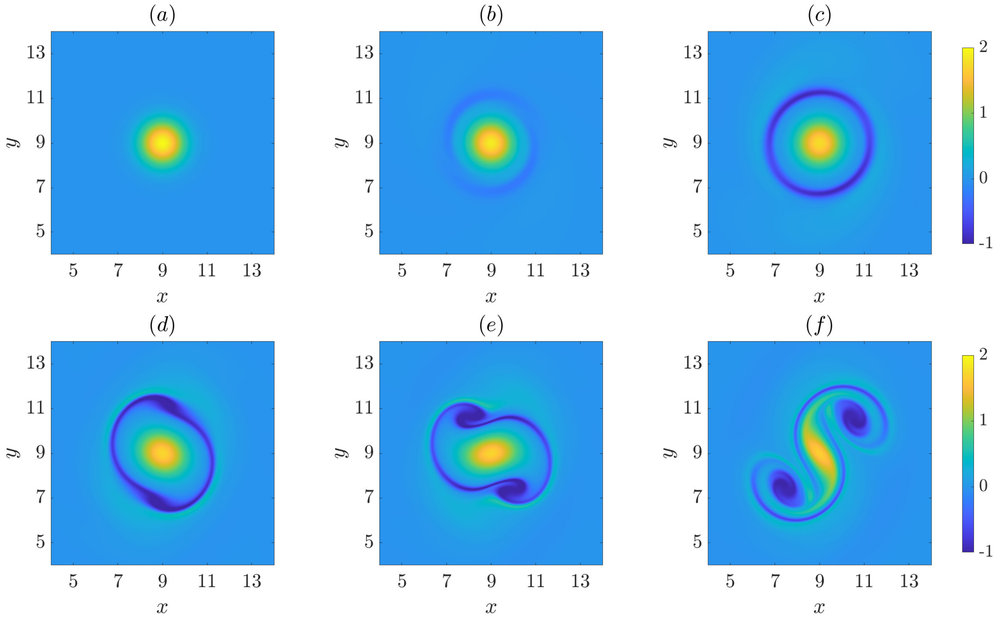

Fig. 3.3: Vertical vorticity at different times: (a) $t=1$, (b) $t=30$, (c) $t=60$, (d) $t=75$, (e) $t=80$ and (f) $t=90$ for $Re=2000$, $F_h=10$, $Ro=23.1$, $\phi=60°$ ($\widetilde{Ro}=40$).

3.3.2 Effects of the stratification

When the Froude number is decreased from $F_h=10$ to $F_h=2$, the same evolution of the vertical velocity (figure 3.4 $(a)-(d)$, see the movie in the supplementary material) and the vertical vorticity (figure 3.4 $(e)-(h)$) is observed but at a smaller radius. However, the anomaly of the vertical vorticity does not become negative this time and the maximum vertical velocity is also lower than for $F_h=10$. Figure 3.5(a) shows the evolution of the vertical velocity maximum u_{zm}. In fact, three phases can be distinguished. First, u_{zm} increases linearly with time with some small oscillations superimposed which will be later attributed to inertia-gravity waves. The propagation of waves can be also seen in the vertical velocity field at the beginning of the movies. Then, u_{zm} saturates and tends to slightly decrease. When $t \gtrsim 60$, large oscillations arise when the vortex becomes fully non-axisymmetric.

If the Froude number is below unity, such evolution is no longer observed. In §3.4, it will be shown that this phenomenon is due the presence of a critical layer where the angular velocity of the vortex is equal to the non-dimensional Brunt–Väisälä frequency, i.e. $\Omega=1/F_h$, where Ω is the non-dimensional angular velocity of the vortex corresponding to the vorticity field (3.5).

3.3.3 Effects of the Rossby numbers

When the traditional Rossby number Ro, which is based on the vertical component of the background rotation, is varied, while keeping the other numbers fixed (Re, F_h,

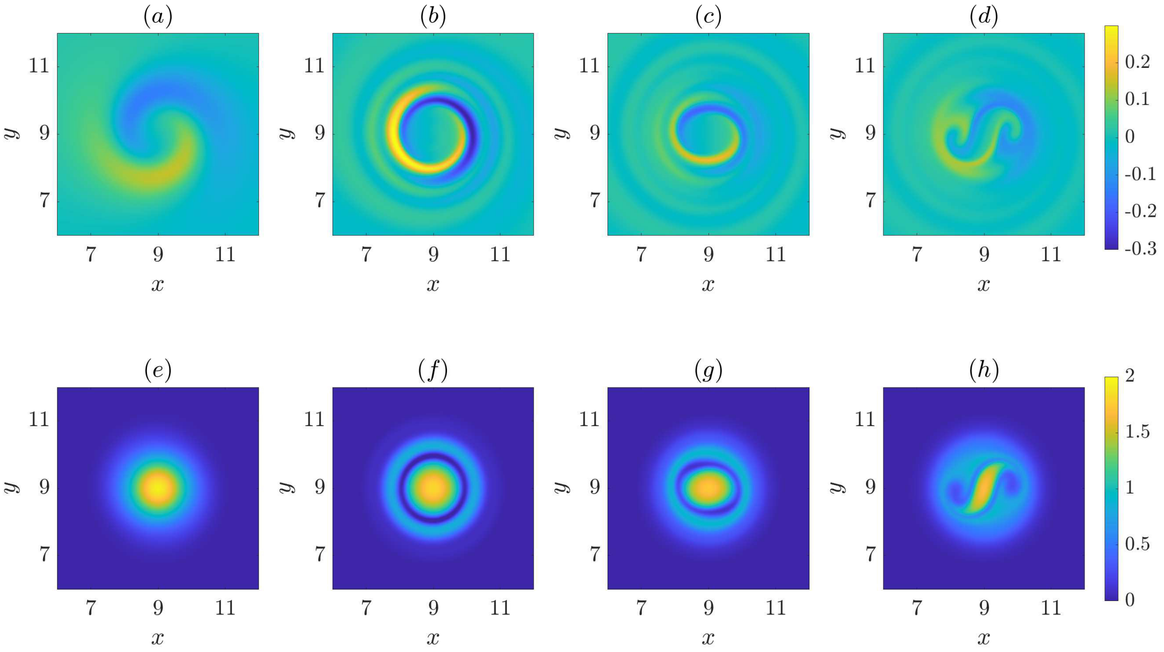

Fig. 3.4: Vertical velocity (top) and vertical vorticity (bottom) at different times: (a, e) $t = 10$, (b, f) $t = 40$, (c, g) $t = 65$ and (d, h) $t = 80$ for $Re = 2000$, $F_h = 2$, $Ro = 23.1$, $\phi = 60°$ ($\widetilde{Ro} = 40$).

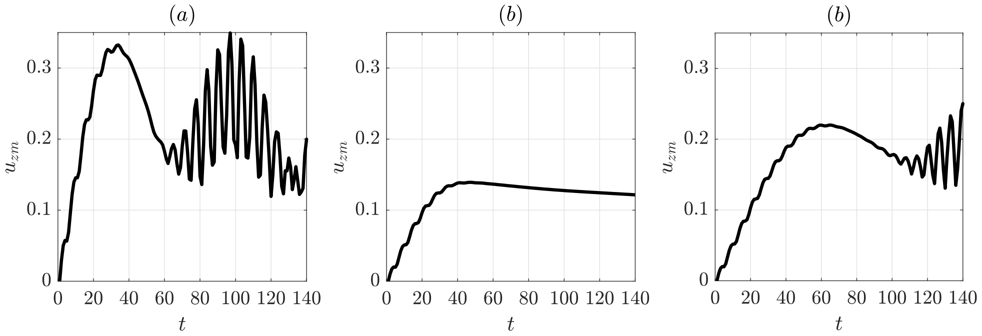

Fig. 3.5: Maximum vertical velocity as a function of time for $F_h = 2$ and (a) $Re = 2000$, $Ro = 23.1$, $\phi = 60°$ ($\widetilde{Ro} = 40$), (b) $Re = 2000$, $Ro = 20.3$, $\phi = 80°$ ($\widetilde{Ro} = 115.2$) and (c) $Re = 10000$, $Ro = 20.3$, $\phi = 80°$ ($\widetilde{Ro} = 115.2$).

$\widetilde{Ro}$), the vortex evolution remains strictly identical. This is consistent with the fact that the dynamics is independent of the vertical coordinate so that the Coriolis force associated with Ro can be eliminated from (3.7) by redefining the pressure.

In contrast, varying the non-traditional Rossby number $\widetilde{Ro}$, which is based on the horizontal component of the background rotation, has important effects on the evolution of the vortex. Since the Rossby number Ro has no effect, the effect of $\widetilde{Ro}$ has been studied by varying the latitude ϕ while keeping the background rotation rate Ω_b constant. Hence, both $\widetilde{Ro}$ and Ro varies. Figure 3.6 shows the evolution of the vertical velocity and vertical vorticity when the latitude is increased from $\phi = 60°$ to $\phi = 80°$ ($\widetilde{Ro}$ is increased from $\widetilde{Ro} = 40$ to $\widetilde{Ro} = 115.2$) while keeping the other parameters fixed (A movie is available in the supplementary material). The initial evolution (figure 3.6(a, b, e, f) is similar to the one in figure 3.4 but, later (figure 3.6(c, d, g, h)), the fields keep the same shape, i.e. no significant asymmetric deformations can be seen in contrast to figure 3.4(d, h). As seen in figure 3.5(b), only two phases are then present in the evolution of the maximum vertical velocity. First, a phase where u_{zm} grows linearly with weak oscillations and, second, a phase where u_{zm} remains approximately constant. In addition, the maximum vertical velocity is lower (figure 3.6(b, c)) and the anomalous vorticity ring is weaker (figure 3.6(g)) than in figure 3.4. At late time $t = 200$ (figure 3.6(d, h)), we can see that the vertical velocity has decreased by viscous diffusion while the vertical velocity field has moved towards the center of the vortex. This is consistent with the critical layer's interpretation since, as the angular velocity decays, the radius where $\Omega = 1/F_h$ decreases.

3.3.4 Effects of the Reynolds number

Figure 3.7 shows the evolution of the vertical velocity and vertical vorticity when the Reynolds number is increased from $Re = 2000$ to $Re = 10000$ while keeping the other parameters as in figure 3.6. A movie is also available in the supplementary material. The maximum vertical velocity is almost doubled and the vertical velocity field is much thinner and focused near a given radius (figure 3.7(b)) than in figure 3.6. Furthermore, the ring of anomalous vertical vorticity (figure 3.7(f)) is more intense. Later, asymmetric deformations of this ring and of the vertical velocity field are clearly visible (figure 3.7(c, d, g, h)) in contrast to figure 3.6. Oscillations are then visible in the evolution of u_{zm} (figure 3.5(c)).

3.3.5 Combined effects of $\widetilde{Ro}$ and Re

In the previous sections, we have seen that the vertical vorticity becomes fully non-axisymmetric in a second stage if ϕ is sufficiently lower than 90°, i.e. if $\widetilde{Ro}$ is not too large (figure 3.4) or if the Reynolds number is large enough (figure 3.7), otherwise the vertical vorticity field remains quasi-axisymmetric (figure 3.6). Figure 3.8 summarizes several other simulations for various $\widetilde{Ro}$ and Reynolds numbers Re keeping the Froude number equal to $F_h = 2$. Yellow and blue symbols indicate simulations where the vertical vorticity remains quasi-axisymmetric or becomes non-axisymmetric, respectively. We can see that the critical Rossby number $\widetilde{Ro}_c$ above which the vortex remains quasi-

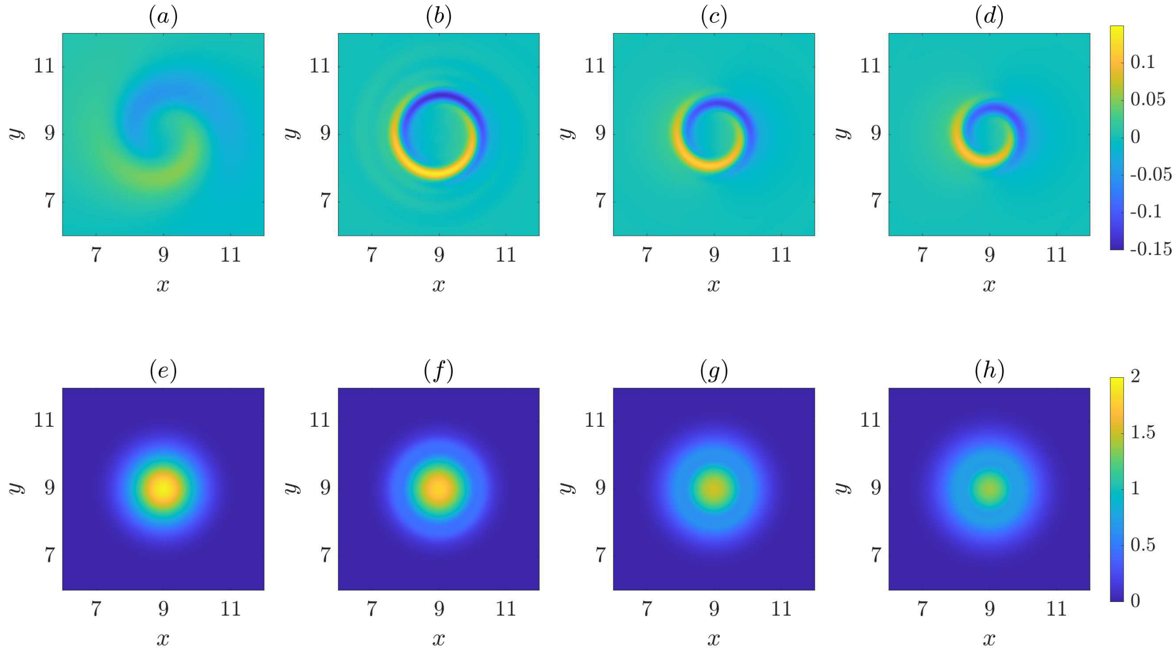

Fig. 3.6: Vertical velocity (top) and vertical vorticity (bottom) at different times: (a,e) $t = 10$, (b,f) $t = 50$, (c,g) $t = 150$ and (d,h) $t = 200$ for $Re = 2000$, $F_h = 2$, $Ro = 20.3$, $\phi = 80°$ ($\widetilde{Ro} = 115.2$).

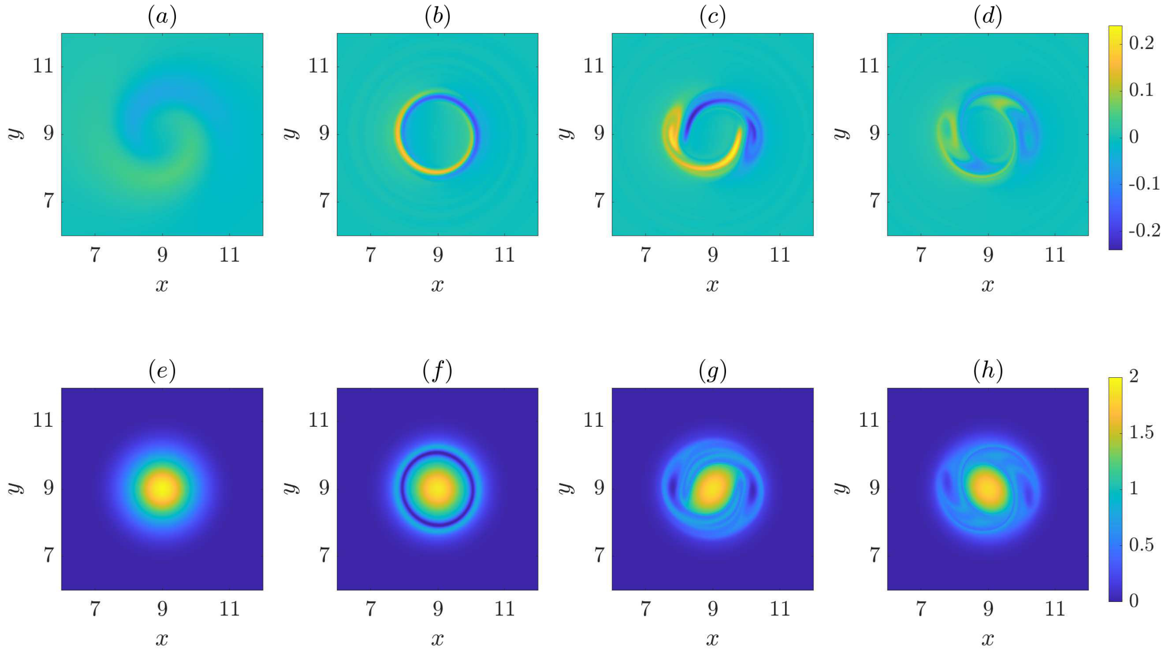

Fig. 3.7: Vertical velocity (top) and vertical vorticity (bottom) at different times: (a, e) $t = 10$, (b, f) $t = 100$, (c, g) $t = 150$ and (d, h) $t = 200$ for $Re = 10000$, $F_h = 2$, $Ro = 20.3$, $\phi = 80°$ ($\widetilde{Ro} = 115.2$).

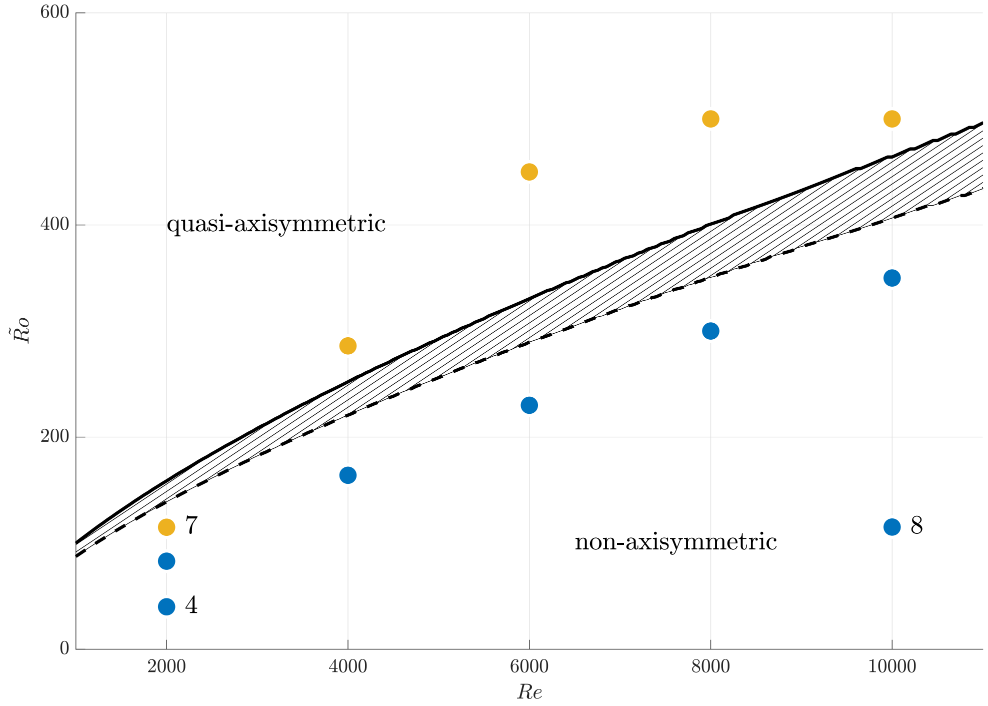

Fig. 3.8: Map of the simulations in the parameter space $(Re, \widetilde{Ro})$ for $F_h = 2$. The yellow and blue circles represent simulations where the vertical vorticity remains quasi-axisymmetric or not, respectively. The solid and dashed lines represent the criterion (3.71) for different values of (a, c): $(\infty, 0)$ and $(\infty, 0.4)$, respectively. The numbers near some points indicate the figure numbers where the corresponding simulation is shown.

axisymmetric increases with the Reynolds number from $\widetilde{Ro}_c \simeq 100$ for $Re = 2000$ to $\widetilde{Ro}_c \simeq 400$ for $Re = 10000$.

3.4 Asymptotic analyses

In order to understand the vortex evolution observed in the DNS, it is interesting to perform an asymptotic analysis for small horizontal component of the background rotation, i.e. for $\widetilde{Ro} \gg 1$, and for large Reynolds number. To this end, it is first convenient to rewrite (3.6-3.8) in cylindrical coordinates (r, θ, z)

$$\frac{1}{r}\frac{\partial r u_r}{\partial r} + \frac{1}{r}\frac{\partial u_\theta}{\partial \theta} + \frac{\partial u_z}{\partial z} = 0, \tag{3.10a}$$

$$\begin{aligned}&\frac{\partial u_r}{\partial t}+u_r\frac{\partial u_r}{\partial r}+\frac{u_\theta}{r}\frac{\partial u_r}{\partial \theta}+u_z\frac{\partial u_r}{\partial z}-\frac{{u_\theta}^2}{r}=-\frac{\partial p}{\partial r}+\frac{2u_\theta}{Ro}-\frac{2u_z}{\widetilde{Ro}}\cos(\theta)\\&+\frac{1}{Re}\left(\nabla^2 u_r-\frac{2}{r^2}\frac{\partial u_\theta}{\partial \theta}\right),\end{aligned}\tag{3.10b}$$

$$\begin{aligned}&\frac{\partial u_\theta}{\partial t}+u_r\frac{\partial u_\theta}{\partial r}+\frac{u_\theta}{r}\frac{\partial u_\theta}{\partial \theta}+u_z\frac{\partial u_\theta}{\partial z}+\frac{u_r u_\theta}{r}=-\frac{1}{r}\frac{\partial p}{\partial \theta}-\frac{2u_r}{Ro}+\frac{2u_z}{\widetilde{Ro}}\sin(\theta)\\&+\frac{1}{Re}\left(\nabla^2 u_\theta+\frac{2}{r^2}\frac{\partial u_r}{\partial \theta}\right),\end{aligned}\tag{3.10c}$$

$$\frac{\partial u_z}{\partial t}+u_r\frac{\partial u_z}{\partial r}+\frac{u_\theta}{r}\frac{\partial u_z}{\partial \theta}+u_z\frac{\partial u_z}{\partial z}=-\frac{\partial p}{\partial z}+b+\frac{2u_r}{\widetilde{Ro}}\cos(\theta)-\frac{2u_\theta}{\widetilde{Ro}}\sin(\theta)+\frac{1}{Re}\nabla^2 u_z,\tag{3.10d}$$

$$\frac{\partial b}{\partial t}+u_r\frac{\partial b}{\partial r}+\frac{u_\theta}{r}\frac{\partial b}{\partial \theta}+u_z\frac{\partial b}{\partial z}+\frac{u_z}{F_h^2}=\frac{1}{ReSc}\nabla^2 b.\tag{3.10e}$$

It is also convenient to consider the equation for the vertical vorticity ζ:

$$\frac{\partial \zeta}{\partial t}+\boldsymbol{u}.\boldsymbol{\nabla}\zeta=(\boldsymbol{\omega}+\frac{2}{Ro}\boldsymbol{e_z}).\boldsymbol{\nabla}u_z+\frac{2}{r\tilde{Ro}}\left[\frac{\partial}{\partial r}\left(ru_z\sin(\theta)\right)+\frac{\partial}{\partial \theta}\left(u_z\cos(\theta)\right)\right]+\frac{1}{Re}\Delta\zeta,\tag{3.11}$$

where $\boldsymbol{\omega}=\nabla\times\boldsymbol{u}$.

The solution is expanded with the small parameter $\varepsilon=2/\widetilde{Ro}\ll 1$ in the form

$$(u_r,u_\theta,u_z,p,b)=(0,u_{\theta 0},0,p_0,0)+\varepsilon(u_{r1},u_{\theta 1},u_{z1},p_1,b_1)+...,\tag{3.12}$$

where $u_{\theta 0}=r\Omega$, with $\Omega=(1-e^{-r^2})/r^2$, is the non-dimensional angular velocity of the vortex corresponding to the vorticity field (3.5).

It is first instructive to consider a steady and non-diffusive flow, i.e. $\partial/\partial t=0$ and $Re=\infty$. Then, (3.10b) reduces at leading order to the cyclostrophic balance

$$-\frac{u_{\theta 0}^2}{r}=-\frac{\partial p_0}{\partial r}+\frac{2u_{\theta 0}}{Ro},\tag{3.13}$$

whereas (3.10a,3.10c-3.10e) are identically zero at leading order. At first order in ε, it is sufficient to consider only (3.10d) and (3.10e):

$$\Omega\frac{\partial u_{z1}}{\partial \theta}=-r\Omega\sin(\theta)+b_1,\tag{3.14a}$$

$$\Omega\frac{\partial b_1}{\partial \theta}=-\frac{u_{z1}}{F_h^2}.\tag{3.14b}$$

The solution is

$$u_{z1}=\frac{r\Omega^2F_h^2}{F_h^2\Omega^2-1}\cos(\theta),\tag{3.15a}$$

$$b_1 = \frac{-r\Omega}{F_h^2\Omega^2 - 1}\sin(\theta), \tag{3.15b}$$

showing that the Coriolis force due to the horizontal component of the background rotation (first term in the right hand side of (3.14a) forces a vertical velocity and buoyancy fields. These fields are independent of the vertical coordinate as observed in the DNS. However, we can remark that (3.15a-3.15b) are singular if there exists a radius r_c where $\Omega(r_c) = 1/F_h$. Such critical radius exists wherever $F_h > 1$ since the non-dimensional angular velocity decreases from unity on the vortex axis to zero for $r \to \infty$.

A similar critical layer occurs in the case of a tilted vortex in a stratified fluid (Boulanger *et al.*, 2007) and in stratified rotating shear flow (Wang & Balmforth, 2020). This singularity can be smoothed if the flow is no longer assumed to be steady or inviscid. Although these two effects can a priori operate simultaneously, the unsteadiness turns out to be, first, the dominant effect while diffusive effects are negligible followed by a second phase where it is the opposite.

3.4.1 Unsteady inviscid analysis

Accordingly, we first consider (3.10a-3.10e) in the inviscid limit $Re = \infty$ but keeping the time derivatives. At leading order, the equations reduce to

$$-\frac{u_{\theta 0}^2}{r} = \frac{\partial p_0}{\partial r} + \frac{2u_{\theta 0}}{Ro}, \tag{3.16}$$

$$\frac{\partial u_{\theta 0}}{\partial t} = 0, \tag{3.17}$$

so that $u_{\theta 0} = r\Omega$ as before. At first order, the equations (3.10d-3.10e) become

$$\frac{\partial u_{z1}}{\partial t} + \Omega\frac{\partial u_{z1}}{\partial \theta} = b_1 - r\Omega\sin(\theta), \tag{3.18a}$$

$$\frac{\partial b_1}{\partial t} + \Omega\frac{\partial b_1}{\partial \theta} = -\frac{u_{z1}}{F_h^2}. \tag{3.18b}$$

The only difference with (3.15) is the presence of the time derivatives. By imposing $u_{z1} = b_1 = 0$ at $t = 0$, the solutions can be found in the form

$$u_{z1} = u_{zp}\mathrm{e}^{i\theta} + u_{zp}^*\mathrm{e}^{-i\theta}, \tag{3.19a}$$

$$b_1 = b_p\mathrm{e}^{i\theta} + {b^*}_p\mathrm{e}^{-i\theta}, \tag{3.19b}$$

where the star denotes the complex conjugate and

$$u_{zp} = \frac{r\Omega}{4}\left[-\frac{1}{\alpha}\left(1 - \mathrm{e}^{i\alpha t}\right) + \frac{1}{\beta}\left(1 - \mathrm{e}^{-i\beta t}\right)\right], \tag{3.20a}$$

$$b_p = -i\frac{r\Omega}{4F_h}\left[\frac{1}{\alpha}\left(1 - \mathrm{e}^{i\alpha t}\right) + \frac{1}{\beta}\left(1 - \mathrm{e}^{-i\beta t}\right)\right], \tag{3.20b}$$

with

$$\alpha = \frac{1 - F_h\Omega}{F_h}, \qquad \beta = \frac{1 + F_h\Omega}{F_h}. \tag{3.21}$$

Compared to the steady solution (3.15), the additional terms present in (3.20) correspond to waves generated at $t = 0$ to satisfy the initial conditions. These waves oscillate at the frequencies $1/F_h - \Omega$ and $-1/F_h - \Omega$, i.e. the non-dimensional Brunt–Väisälä frequency with an additional Doppler shift coming from the azimuthal motion of the vortex. Hence, they correspond to inertia-gravity waves with zero vertical wavenumber. In contrast to (3.15), we see now that the vertical velocity and buoyancy (3.19a-3.19b) are no longer singular at the radius r_c where $\Omega(r_c) = 1/F_h$. Indeed, we have $(1 - e^{i\alpha t})/\alpha \simeq -it$ when $\alpha \to 0$ so that (3.20a-3.20b) remain finite at $r = r_c$.

Following Wang & Balmforth (2020), the behaviour of these solutions in the vicinity of the critical radius can be studied more precisely by introducing the variable $\eta = r - r_c$. When $\eta \ll 1$, the vertical velocity approximates to

$$\begin{aligned} u_{z1} = &\left[\left(\frac{r_c\Omega_c}{2\eta\Omega_c'} + \frac{\Omega_c}{2\Omega_c'} + \frac{r_c}{2} - \frac{r_c\Omega_c''\Omega_c}{4{\Omega_c'}^2}\right)\left(1 - \cos\left(\eta\Omega_c' t\right)\right) + \frac{r_c}{4}\left(1 - \cos\left(\frac{2}{F_h}t\right)\right)\right]\cos\left(\theta\right) \\ &- \left[\left(\frac{r_c\Omega_c}{2\eta\Omega_c'} + \frac{\Omega_c}{2\Omega_c'} + \frac{r_c}{2} - \frac{r_c\Omega_c''\Omega_c}{4{\Omega_c'}^2}\right)\sin\left(\eta\Omega_c' t\right) + \frac{r_c}{4}\sin\left(\frac{2}{F_h}t\right)\right]\sin\left(\theta\right) + O(\eta), \end{aligned} \tag{3.22}$$

where the subscript c indicates a value taken at r_c. The terms involving $\eta\Omega_c' t$ in the sin and cos functions have not been expanded in (3.22) since this quantity can be large when t is large even for small η. The approximation (3.22) is therefore uniformly valid whatever t. Taking into account only the leading order, (3.22) can be simplified and rewritten as

$$u_{z1} = \frac{r_c\Omega_c t}{2}\left[\left(\frac{1 - \cos U}{U}\right)\cos\left(\theta\right) - \frac{\sin U}{U}\sin\left(\theta\right)\right] + O(1), \tag{3.23}$$

where $U = \eta\Omega_c' t$. This expression shows that the radial profile of the vertical velocity in the vicinity of r_c depends only on the self-similar variable U. This implies that the vertical velocity will be more and more concentrated around r_c as time increases. In addition, (3.23) shows that the amplitude of u_{z1} will increase linearly with time for a fixed value of U. In practice, the approximation (3.23) will be accurate only when t is large since the neglected terms are of order unity. Since $\Omega_c = 1/F_h$, this will occur more and more later when F_h increases. We emphasize that the inertia-gravity wave oscillating at frequency $1/F_h + \Omega_c = 2/F_h$ is neglected in (3.23) unlike in (3.22).

3.4.2 Unsteady viscous analysis

Here, viscous and diffusive effects are taken into account in addition to the time evolution. Following Boulanger *et al.* (2007) and Wang & Balmforth (2020, 2021), we assume that the Reynolds number is large $Re \gg 1$ and consider only the vicinity of the critical radius by introducing a rescaled radius such that $\tilde{r} = Re^{1/3}(r - r_c)$. We also assume that the evolution occurs over the slow time $T = Re^{-1/3}t$. Since $Re \gg 1$, the leading order solution of (3.10a-3.10e) is still $u_{\theta 0} = r\Omega$. At order ε, the equations (3.10d-3.10e) become

$$\begin{aligned}\frac{1}{Re^{1/3}}\frac{\partial u_{z1}}{\partial T} + \left(\Omega_c + \frac{\tilde{r}\Omega_c'}{Re^{1/3}} + O\left(\frac{1}{Re^{2/3}}\right)\right)\frac{\partial u_{z1}}{\partial \theta} &= b_1 \\ - \left(r_c\Omega_c + \frac{\tilde{r}(\Omega_c + r_c\Omega_c')}{Re^{1/3}} + O\left(\frac{1}{Re^{2/3}}\right)\right)\sin(\theta) &+ \frac{1}{Re^{1/3}}\frac{\partial^2 u_{z1}}{\partial \tilde{r}^2} + O\left(\frac{1}{Re^{2/3}}\right),\end{aligned} \tag{3.24a}$$

$$\frac{1}{Re^{1/3}}\frac{\partial b_1}{\partial T} + \left(\Omega_c + \frac{\tilde{r}\Omega_c'}{Re^{1/3}} + O\left(\frac{1}{Re^{2/3}}\right)\right)\frac{\partial b_1}{\partial \theta} = -\frac{u_{z1}}{F_h^2} + \frac{1}{Sc}\left[\frac{1}{Re^{1/3}}\frac{\partial^2 b_1}{\partial \tilde{r}^2} + O\left(\frac{1}{Re^{2/3}}\right)\right]. \tag{3.24b}$$

These equations can be solved by expanding u_{z1} and b_1 as follows

$$u_{z1} = Re^{1/3}\left[\tilde{u}_{z1}(\tilde{r},T)\mathrm{e}^{i\theta} + c.c.\right] + \tilde{u}_{z2}(\tilde{r},T)\mathrm{e}^{i\theta} + c.c. + ..., \tag{3.25a}$$

$$b_1 = Re^{1/3}\left[\tilde{b}_1(\tilde{r},T)\mathrm{e}^{i\theta} + c.c.\right] + \tilde{b}_2(\tilde{r},T)\mathrm{e}^{i\theta} + c.c. + ... \tag{3.25b}$$

By substituting (3.25a-3.25b) in (3.24a-3.24b), we get at order $O(Re^{1/3})$

$$i\Omega_c\tilde{u}_{z1} = \tilde{b}_1, \tag{3.26a}$$

$$i\Omega_c\tilde{b}_1 = -\frac{\tilde{u}_{z1}}{F_h^2}, \tag{3.26b}$$

which both yields

$$\tilde{b}_1 = i\Omega_c\tilde{u}_{z1}. \tag{3.27}$$

The equations at order $O(1)$ are

$$\frac{\partial \tilde{u}_{z1}}{\partial T} + i\Omega_c\tilde{u}_{z2} + i\tilde{r}\Omega_c'\tilde{u}_{z1} = \tilde{b}_2 - \frac{r_c\Omega_c}{2i} + \frac{\mathrm{d}^2\tilde{u}_{z1}}{\mathrm{d}\tilde{r}^2}, \tag{3.28a}$$

$$\frac{\partial \tilde{b}_1}{\partial T} + i\Omega_c\tilde{b}_2 + i\tilde{r}\Omega_c'\tilde{b}_1 = -\frac{1}{F_h^2}\tilde{u}_{z2} + \frac{1}{Sc}\frac{\mathrm{d}^2\tilde{b}_1}{\mathrm{d}\tilde{r}^2}. \tag{3.28b}$$

By using (3.27), the solvability condition to find $\tilde{b}_2$ and $\tilde{u}_{z2}$ from (3.28a-3.28b) requires $\tilde{u}_{z1}$ to satisfy

$$\frac{\partial \tilde{u}_{z1}}{\partial T} + i\tilde{r}\Omega_c'\tilde{u}_{z1} = \frac{i}{4}r_c\Omega_c + \frac{1}{2}\left(1 + \frac{1}{Sc}\right)\frac{\mathrm{d}^2\tilde{u}_{z1}}{\mathrm{d}\tilde{r}^2}. \tag{3.29}$$

As shown by Wang & Balmforth (2020, 2021), the solution is

$$\tilde{u}_{z1} = iA\frac{1}{\pi}\int_0^{\left|\Omega_c'\right|T/\gamma} \exp\left(-\frac{z^3}{3} + i\gamma\tilde{r}z\right)\mathrm{d}z, \tag{3.30}$$

where

$$A = \frac{\pi r_c \Omega_c}{2\left|2\Omega_c^{'}\right|^{2/3}\left(1+\frac{1}{Sc}\right)^{1/3}}, \qquad \gamma = \frac{\left|2\Omega_c^{'}\right|^{1/3}}{\left(1+\frac{1}{Sc}\right)^{1/3}}. \tag{3.31}$$

When $\left|\Omega_c^{'}\right| T/\gamma \gg 1$, the upper bound in the integral can be replaced by infinity so that (3.30) recovers the steady solution (Boulanger *et al.*, 2007)

$$\tilde{u}_{z1} = iA\mathrm{Hi}(i\gamma\tilde{r}), \tag{3.32}$$

where Hi is the Scorer's function (Abramowitz & Stegun, 1972). We will see that the time interval where both the unsteadiness and viscous effects are important is short so that (3.32) turns out to be reached quickly after the inviscid regime.

3.4.3 Effect on the vertical vorticity

We now turn to the study of the effect of the vertical velocity on the vertical vorticity. Since the flow is invariant along the vertical, the equation for the vertical vorticity (3.11) reduces to

$$\frac{\partial \zeta}{\partial t} + \boldsymbol{u}.\boldsymbol{\nabla}\zeta = \frac{\varepsilon}{r}\left[\frac{\partial}{\partial r}\left(r u_z \sin(\theta)\right) + \frac{\partial}{\partial \theta}\left(u_z \cos(\theta)\right)\right] + \frac{1}{Re}\Delta_h \zeta. \tag{3.33}$$

This equation shows that the vertical velocity generated at order $O(\varepsilon)$ will in turn force a vertical vorticity field at order $O(\varepsilon^2)$. In order to compute this second order horizontal flow, the vertical vorticity and stream function can be expanded as

$$\zeta = \zeta_0 + \varepsilon^2 \zeta_2 + ..., \tag{3.34}$$

$$\psi = \psi_0 + \varepsilon^2 \psi_2 + ..., \tag{3.35}$$

where (ζ_0, ψ_0) are the non-dimensional vertical vorticity and stream function of the base flow (3.5) and $\zeta_2 = \Delta_h \psi_2$. The second order vertical vorticity follows

$$\frac{\partial \zeta_2}{\partial t} + \Omega\frac{\partial \zeta_2}{\partial \theta} - \frac{1}{r}\frac{\partial \psi_2}{\partial \theta}\frac{\partial \zeta_0}{\partial r} = \frac{1}{r}\left[\frac{\partial}{\partial r}\left(r u_{z1} \sin(\theta)\right) + \frac{\partial}{\partial \theta}\left(u_{z1}\cos(\theta)\right)\right] + \frac{1}{Re}\Delta_h \zeta_2. \tag{3.36}$$

Since the first order vertical velocity u_{z1} has an azimuthal wavenumber $m = 1$, ζ_2 and ψ_2 can be sought in the form

$$\zeta_2 = \zeta_{20}(r,t) + \left[\zeta_{22}(r,t)e^{2i\theta} + c.c.\right], \tag{3.37}$$

$$\psi_2 = \psi_{20}(r,t) + \left[\psi_{22}(r,t)e^{2i\theta} + c.c.\right]. \tag{3.38}$$

In the following, we will determine only the axisymmetric part ζ_{20} since we will show that the component ζ_{22} grows slower than ζ_{20}.

Inviscid evolution of ζ_{20}

When u_{z1} follows the unsteady inviscid expression (3.19a), the axisymmetric vertical vorticity ζ_{20} is given by

$$\frac{\partial \zeta_{20}}{\partial t} = -\frac{i}{2r}\frac{\partial}{\partial r}\left(r(u_{zp}^{*} - u_{zp})\right) . \tag{3.39}$$

By assuming that $\zeta_{20} = 0$ at $t = 0$, the solution reads

$$\begin{aligned}\zeta_{20} =& \frac{\zeta_0}{4}\left(\frac{\cos(\alpha t) - 1}{\alpha^2} + \frac{\cos(\beta t) - 1}{\beta^2}\right) \\ &+ \frac{r\Omega\Omega'}{4}\left[\frac{\alpha t \sin(\alpha t) + 2(\cos(\alpha t) - 1)}{\alpha^3} - \frac{\beta t \sin(\beta t) + 2(\cos(\beta t) - 1)}{\beta^3}\right] .\end{aligned} \tag{3.40}$$

Considering the vicinity of the critical radius $\eta = r - r_c$, this solution approximates at leading order to

$$\zeta_{20} = \frac{r_c \Omega_c}{4{\Omega_c'}^2 \eta^3}\left[2\left(1 - \cos(\eta\Omega_c' t)\right) - \eta\Omega_c' t \sin(\eta\Omega_c' t)\right] + O\left(\frac{1}{\eta^2}\right) , \tag{3.41}$$

where ηt has been considered finite as in (3.22) so that the approximation remains valid even for long time. In terms of the similarity variable U, (3.41) can be rewritten

$$\zeta_{20} = \frac{r_c \Omega_c \Omega_c' t^3}{4}\left[\frac{2(1 - \cos U) - U \sin U}{U^3}\right] + O\left(\frac{1}{\eta^2}\right) . \tag{3.42}$$

This expression shows that ζ_{20} remains finite and even vanishes when $U \to 0$ but ζ_{20} is more and more concentrated in the vicinity of the critical layer as time increases. Furthermore, its amplitude increases like t^3 at leading order.

Using the same approach for ζ_{22}, it can be shown that its amplitude grows like t^2 instead of t^3. Indeed, the forcing term of ζ_{22} is proportional to t^2 like for ζ_{20} but the left hand side of (3.36) is dominated by the term $2i\Omega_c\zeta_{22}$ instead of $\partial\zeta_{20}/\partial t$ for the axisymmetric component. Thus, ζ_{22} is proportional to t^2, at least initially. This explains why the vertical vorticity is observed in the DNS to remain quasi-axisymmetric during the first two phases.

Viscous evolution of ζ_{20}

When the vertical velocity is given by the unsteady viscous solution (3.25a) and (3.30), it is possible to also obtain its effect on the second order axisymmetric vertical vorticity ζ_{20}. Expressing first (3.36) in terms of $\tilde{r}$ and T gives at leading order when $Re \gg 1$

$$\frac{1}{Re^{1/3}}\frac{\partial \zeta_{20}}{\partial T} = \frac{-i}{2}Re^{2/3}\frac{\partial}{\partial \tilde{r}}\left(\tilde{u}_{z1}^{*} - \tilde{u}_{z1}\right) + O(Re^{1/3}) + \frac{1}{Re^{1/3}}\frac{\partial^2 \zeta_{20}}{\partial \tilde{r}^2} + \dots . \tag{3.43}$$

As shown by Wang & Balmforth (2021), the exact solution of (3.43) can be found by means of a Fourier transform in $\tilde{r}$ using (3.30). This gives

$$\zeta_{20} = -i\frac{ReA}{2\gamma\pi}\int_0^{|\Omega_c'|T} \exp\left(\frac{-q^3}{3\gamma^3} + iq\tilde{r}\right)\left(\frac{1 - \exp\left(q^3/|\Omega_c'| - q^2 T\right)}{q}\right) \mathrm{d}q + c.c. \quad . \tag{3.44}$$

In appendix, an approximation of (3.44) valid for large time $T \gg 1$ is found in the form

$$\zeta_{20} = \zeta_{20}^{(1)} + \zeta_{20}^{(2)}, \tag{3.45}$$

where

$$\zeta_{20}^{(1)}(\tilde{r}) = Re\frac{A}{2}\int_0^{\tilde{r}} \left(\mathrm{Hi}^*(i\gamma u) + \mathrm{Hi}(i\gamma u)\right) \mathrm{d}u, \tag{3.46a}$$

$$\zeta_{20}^{(2)}(\tilde{r}, t) = -Re\frac{A}{2\gamma}\mathrm{erf}\left(\frac{\tilde{r}}{\sqrt{4tRe^{-1/3}}}\right). \tag{3.46b}$$

This approximation shows that ζ_{20} saturates and tends toward (3.46a) for $tRe^{-1/3} \to \infty$ for $\tilde{r} = O(1)$. However, when $|\tilde{r}| \to \infty$ and $tRe^{-1/3}$ is finite, ζ_{20} vanishes. The approximation (3.45) will be compared to numerical solutions of (3.43) as well as DNS in section (3.5.2).

To summarize, the axisymmetric vertical vorticity correction at order $O(\varepsilon^2)$, ζ_{20}, follows two distinct regimes. First, it evolves purely inviscidly and grows like t^3 according to (3.40). Then, it tends to saturate and follows the approximation (3.45) for large times. This shows that ζ_{20} saturates toward the steady solution (3.46a) for finite $\tilde{r}$.

3.4.4 Non-linear analysis of the critical layer

The viscous linear analysis of the critical layer in sections 3.4.2 and 3.4.3 has shown that the vertical velocity scales as $u_z = O(\varepsilon Re^{1/3})$. This creates a vorticity correction of the order $\delta\zeta = O(\varepsilon^2 Re)$ (see (3.34), (3.37), (3.45)-(3.46)). Since $r = r_c + \tilde{r}/Re^{1/3}$ in the critical layer, the corresponding angular velocity correction $\delta\Omega$ is given at leading order by $\delta\zeta \simeq r_c Re^{1/3}\partial\delta\Omega/\partial\tilde{r}$ so that $\delta\Omega = O(\varepsilon^2 Re^{2/3})$. In turn, we see that this angular velocity correction would have the same order as the other terms of order $O(1/Re^{1/3})$ in (3.24) if $\varepsilon^2 Re^{2/3} = O(1/Re^{1/3})$, i.e. if

$$Re = \frac{\widetilde{Re}}{\varepsilon^2}, \tag{3.47}$$

where $\widetilde{Re}$ is of order unity. For this distinguished limit, there is therefore a non-linear feedback of the horizontal flow on the evolutions of the vertical velocity and buoyancy as considered by Wang & Balmforth (2020, 2021). Using the scaling (3.47), the typical order of magnitudes of the different variables can be expressed in terms of ε only: $u_z = O\left(\varepsilon^{1/3}\right)$, $b = O\left(\varepsilon^{1/3}\right)$, $\delta\zeta = O(1)$, $\delta\Omega = O\left(\varepsilon^{2/3}\right)$, $u_r = O\left(\varepsilon^{4/3}\right)$ and the radius and slow time are $\tilde{r} = \varepsilon^{-2/3}(r - r_c)$ and $T = \varepsilon^{2/3}t$, respectively. We also assume $\partial/\partial z = 0$. Accordingly, we expand the variables as follows:

$$u_z = \varepsilon^{1/3}\left[\tilde{u}_{z1}\mathrm{e}^{i\theta} + c.c.\right] + \varepsilon\left[\tilde{u}_{z2}\mathrm{e}^{i\theta} + c.c.\right] + ..., \tag{3.48a}$$

$$b = \varepsilon^{1/3}\left[\tilde{b}_1\mathrm{e}^{i\theta} + c.c.\right] + \varepsilon\left[\tilde{b}_2\mathrm{e}^{i\theta} + c.c.\right] + ..., \tag{3.48b}$$

$$\Omega = \Omega_0 + \varepsilon^{2/3}\Omega_1 + ..., \tag{3.48c}$$

$$u_r = \varepsilon^{4/3} u_{r1} + ..., \tag{3.48d}$$

$$\zeta = \zeta_0 + \zeta_1 + \varepsilon^{2/3}\zeta_2 + ..., \tag{3.48e}$$

where Ω_0 and ζ_0 are the non-dimensional angular velocity and vorticity corresponding to (3.5). In the vicinity of r_c, they can be expanded as

$$\Omega_0 = \Omega_c + \tilde{r}\Omega_c^{'}\varepsilon^{2/3} + ..., \tag{3.49a}$$

$$\zeta_0 = \zeta_c + \tilde{r}\zeta_c^{'}\varepsilon^{2/3} + ... \tag{3.49b}$$

Note that there are only components of the form $\exp(\pm i\theta)$ in (3.48a-3.48b) because the flow is invariant along the vertical and because third harmonics arise only at higher order. Then, (3.10d-3.10e) become at leading order

$$\begin{aligned} &\varepsilon\frac{\partial \tilde{u}_{z1}}{\partial T} + \varepsilon u_{r1}\frac{\partial \tilde{u}_{z1}}{\partial \tilde{r}} + i\left(\Omega_c + \Omega_c^{'}\tilde{r}\varepsilon^{2/3}\right)\varepsilon^{1/3}\tilde{u}_{z1} + i\varepsilon\Omega_1\tilde{u}_{z1} + i\varepsilon\Omega_c\tilde{u}_{z2} \\ &= \varepsilon^{1/3}\tilde{b}_1 + \varepsilon\tilde{b}_2 - \varepsilon\frac{r_c\Omega_c}{2i} + \frac{\varepsilon}{\widetilde{Re}}\frac{\partial^2 \tilde{u}_{z1}}{\partial \tilde{r}^2} + O\left(\varepsilon^{5/3}\right), \end{aligned} \tag{3.50a}$$

$$\begin{aligned} &\varepsilon\frac{\partial \tilde{b}_1}{\partial T} + \varepsilon u_{r1}\frac{\partial \tilde{b}_1}{\partial \tilde{r}} + i\left(\Omega_c + \Omega_c^{'}\tilde{r}\varepsilon^{2/3}\right)\varepsilon^{1/3}\tilde{b}_1 + i\varepsilon\Omega_1\tilde{b}_1 + i\varepsilon\Omega_c\tilde{b}_2 \\ &= -\frac{\varepsilon^{1/3}}{F_h^2}\tilde{u}_{z1} - \frac{\varepsilon}{F_h^2}\tilde{u}_{z2} + \frac{\varepsilon}{\widetilde{ReSc}}\frac{\partial^2 \tilde{b}_1}{\partial \tilde{r}^2} + O\left(\varepsilon^{5/3}\right). \end{aligned} \tag{3.50b}$$

Similarly, the equation (3.11) for the vorticity becomes

$$\begin{aligned} &\varepsilon^{2/3}\frac{\partial \zeta_1}{\partial T} + \left(\Omega_c + \Omega_c^{'}\tilde{r}\varepsilon^{2/3}\right)\frac{\partial \zeta_1}{\partial \theta} + \varepsilon^{2/3}\Omega_1\frac{\partial \zeta_1}{\partial \theta} + \varepsilon^{2/3}u_{r1}\frac{\partial \zeta_1}{\partial \tilde{r}} + \varepsilon^{2/3}\Omega_c\frac{\partial \zeta_2}{\partial \theta} \\ &= \varepsilon^{2/3}\frac{\partial}{\partial \tilde{r}}\left(\left(\tilde{u}_{z1}\mathrm{e}^{i\theta} + \tilde{u}_{z1}^{*}\mathrm{e}^{-i\theta}\right)\sin(\theta)\right) + \frac{\varepsilon^{2/3}}{\widetilde{Re}}\frac{\partial^2 \zeta_1}{\partial \tilde{r}^2} + O\left(\varepsilon^{4/3}\right). \end{aligned} \tag{3.51}$$

At leading order, (3.50-3.51) become

$$\varepsilon^{1/3} i\Omega_c\tilde{u}_{z1} = \varepsilon^{1/3}\tilde{b}_1, \tag{3.52a}$$

$$\varepsilon^{1/3} i\Omega_c\tilde{b}_1 = -\frac{\varepsilon^{1/3}}{F_h^2}\tilde{u}_{z1}, \tag{3.52b}$$

$$\Omega_c\frac{\partial \zeta_1}{\partial \theta} = 0. \tag{3.52c}$$

The first two equations are identical to (3.26) and the third one implies $\zeta_1 \equiv \zeta_1(\tilde{r}, T)$ and $u_{r1} = 0$. At the next order, we have

$$\frac{\partial \tilde{u}_{z1}}{\partial T} + i\Omega_c^{'}\tilde{r}\tilde{u}_{z1} + i\Omega_1\tilde{u}_{z1} + i\Omega_c\tilde{u}_{z2} = \tilde{b}_2 - \frac{r_c\Omega_c}{2i} + \frac{1}{\widetilde{Re}}\frac{\partial^2 \tilde{u}_{z1}}{\partial \tilde{r}^2}, \tag{3.53a}$$

$$\frac{\partial \tilde{b}_1}{\partial T} + i\Omega_c^{'}\tilde{r}\tilde{b}_1 + i\Omega_1\tilde{b}_1 + i\Omega_c\tilde{b}_2 = -\frac{\tilde{u}_{z2}}{F_h^2} + \frac{1}{\widetilde{ReSc}}\frac{\partial^2 \tilde{b}_1}{\partial \tilde{r}^2}, \tag{3.53b}$$

$$\frac{\partial \zeta_1}{\partial T} + \Omega_c \frac{\partial \zeta_2}{\partial \theta} = -\frac{i}{2}\frac{\partial}{\partial \tilde{r}}\left(\tilde{u}_{z1}^* - \tilde{u}_{z1} + \tilde{u}_{z1}\mathrm{e}^{2i\theta} - \tilde{u}_{z1}^*\mathrm{e}^{-2i\theta}\right) + \frac{1}{\widetilde{Re}}\frac{\partial^2 \zeta_1}{\partial \tilde{r}^2}. \tag{3.53c}$$

Equations (3.53a) and (3.53b) are identical to (3.28) except for the presence of the terms involving Ω_1. They can be combined to give

$$\frac{\partial \tilde{u}_{z1}}{\partial T} + i\Omega_c' \tilde{r}\tilde{u}_{z1} + i\Omega_1 \tilde{u}_{z1} = \frac{i}{4} r_c \Omega_c + \frac{1}{2\widetilde{Re}}\left(1 + \frac{1}{Sc}\right)\frac{\partial^2 \tilde{u}_{z1}}{\partial \tilde{r}^2}, \tag{3.54}$$

whereas (3.53c) splits into

$$\frac{\partial \zeta_1}{\partial T} = -\frac{i}{2}\frac{\partial}{\partial \tilde{r}}\left(\tilde{u}_{z1}^* - \tilde{u}_{z1}\right) + \frac{1}{\widetilde{Re}}\frac{\partial^2 \zeta_1}{\partial \tilde{r}^2}, \tag{3.55a}$$

$$\Omega_c \frac{\partial \zeta_2}{\partial \theta} = -\frac{i}{2}\frac{\partial}{\partial \tilde{r}}\left(\tilde{u}_{z1}\mathrm{e}^{2i\theta} - \tilde{u}_{z1}^*\mathrm{e}^{-2i\theta}\right). \tag{3.55b}$$

Since $\zeta_1 = r_c \partial\Omega_1/\partial\tilde{r}$, the equations (3.54-3.55a) form a closed system of equations. An equation for Ω_1 can be obtained by integrating (3.55a):

$$\frac{\partial \Omega_1}{\partial T} = -\frac{i}{2r_c}\left(\tilde{u}_{z1}^* - \tilde{u}_{z1}\right) + \frac{1}{\widetilde{Re}}\frac{\partial^2 \Omega_1}{\partial \tilde{r}^2}. \tag{3.56}$$

Equation (3.55b) shows that the azimuthal wavenumbers $m = \pm 2$ are generated in the vorticity only at higher order explaining again why the vorticity remains quasi-axisymmetric in the DNS during the first two phases. For this reason, components of the form $\exp(\pm 3i\theta)$ arise in the vertical velocity and density (3.48a-3.48b) only at the higher order $\varepsilon^{5/3}$.

3.5 Comparison between the DNS and the asymptotic analyses

We now compare in details the asymptotic and numerical results.

3.5.1 Vertical velocity

Figure 3.9 shows the evolution of the maximum vertical velocity $u_{zm}(\theta, t)$ (solid line) for $\theta = 0$ (figure 3.9(a)) and $\theta = \pi/2$ (figure 3.9(b)) for the set of parameters $Re = 10000$, $F_h = 2$, $Ro = 20.3$, $\phi = 80°$ ($\widetilde{Ro} = 115.2$). Two different angles are considered since the theoretical vertical velocity has the form $u_z = u_{zc}(r,t)\cos(\theta) + u_{zs}(r,t)\sin(\theta)$. Hence, the plots for $\theta = 0$ and $\theta = \pi/2$ allow us to check the predictions for u_{zc} and u_{zs}, respectively.

We can see that the inviscid theoretical solution (3.19a) (red dashed line in figure 3.9(a, b)) predicts very well the initial linear increase of the maximum vertical velocity in the DNS for both angles. The unsteady viscous solution (3.25a,3.30) (yellow dashed line) increases also linearly initially and is in good agreement with the DNS except that it lacks the small oscillations. They are indeed due to inertia-gravity waves oscillating at frequency $1/F_h + \Omega = 2/F_h$ near r_c (see the last term of (3.20a)) and of the two lines of (3.22) which are neglected in (3.23) and section 3.4.2.

When the growth of u_{zm} is no longer linear, the time-dependent viscous solution (3.30) remains in very good agreement with the DNS and describes perfectly the transition towards the steady viscous solution (3.32) (green dashed line). The latter solution is close to the levels of saturation of $u_{zm}(\theta,t)$ for $\theta = 0$ and $\theta = \pi/2$ in the DNS, although the agreement is not as good as for the initial regime. However, the non-linear equations (3.54,3.56) (blue dashed lines) are in better agreement with the DNS indicating that non-linear effects are also active in the saturation. By essence, none of the theoretical solutions can exhibit oscillations associated with the late non-axisymmetric evolution observed in the DNS.

Figures 3.9(c,d) show a similar comparison when the Reynolds number is reduced to $Re = 2000$, keeping the other parameters fixed. In this case, $u_{zm}(\theta = 0, t)$ and $u_{zm}(\theta = \pi/2, t)$ do not oscillate at late time in the DNS (black solid line). The agreement with (3.19a) and (3.30) or (3.32) are then excellent in the initial and saturation regimes, respectively. In addition, we see that the predictions of the non-linear equations (3.54,3.56) remain very close to the linear ones, i.e. (3.30), showing that non-linear effects are weak in this case.

Figure 3.9 shows that the transition from the unsteady inviscid solution (3.19a) to the steady viscous one, (3.32), occurs in a short time range. Therefore, the unsteady viscous solution (3.30) can be well approximated by (3.19a) for $t \leq \mathcal{T}$ and (3.32) for $t \geq \mathcal{T}$, where

$$\mathcal{T} = 2\pi \frac{Re^{1/3}\mathrm{Hi}(0)}{|2\Omega_c'|^{2/3}(1 + 1/Sc)^{1/3}}, \tag{3.57}$$

is the time when the overall maximum given by (3.19a) and (3.32) becomes equal. This time is independent of $\widetilde{Ro}$ and depends only on the Reynolds number, the Froude number via Ω_c' and the Schmidt number.

Figure 3.10 displays a detailed comparison of the radial profile of u_z for $\theta = 0$ and $\theta = \pi/2$ predicted by (3.19a) (red dashed line) and observed in the DNS (black solid line) for different instants in the inviscid regime, i.e. $t \leq \mathcal{T}$ for the same parameters as figures 3.9(a,b). We see that the agreement is excellent even when $t \simeq \mathcal{T}$ (figures 3.10(c,f)). The approximation (3.30) and the solution of the non-linear equations (3.54,3.56) for the vertical velocity are also represented by yellow and blue dashed lines, respectively, in figures 3.10(b,c,e,f). The approximation (3.23) is almost identical to (3.30) in this time range and not represented. As expected, the agreement between the DNS and (3.30) or (3.54,3.56) is very good near r_c but deteriorates away from r_c. We can notice that the blue and yellow dashed lines are superposed everywhere except close to the critical radius r_c for $t = 40$ (figures 3.10(c,f)). In this region, the blue dashed lines are in very good agreement with the DNS indicating that non-linear effects are important there. However, away from r_c, it is (3.19a) (red dashed line) which better agrees with the DNS. For $t = 5$ (figures 3.10(a,d)), the approximations (3.30) and (3.54,3.56) are not accurate and not shown. This is because the profile of u_z is not yet sufficiently localized around r_c at this early time and, therefore, it cannot be well described by a local approximation near r_c. Indeed, we can see in figures 3.10(a,d) that the profiles of u_z are quite different from those in figures 3.10(b,c,e,f).

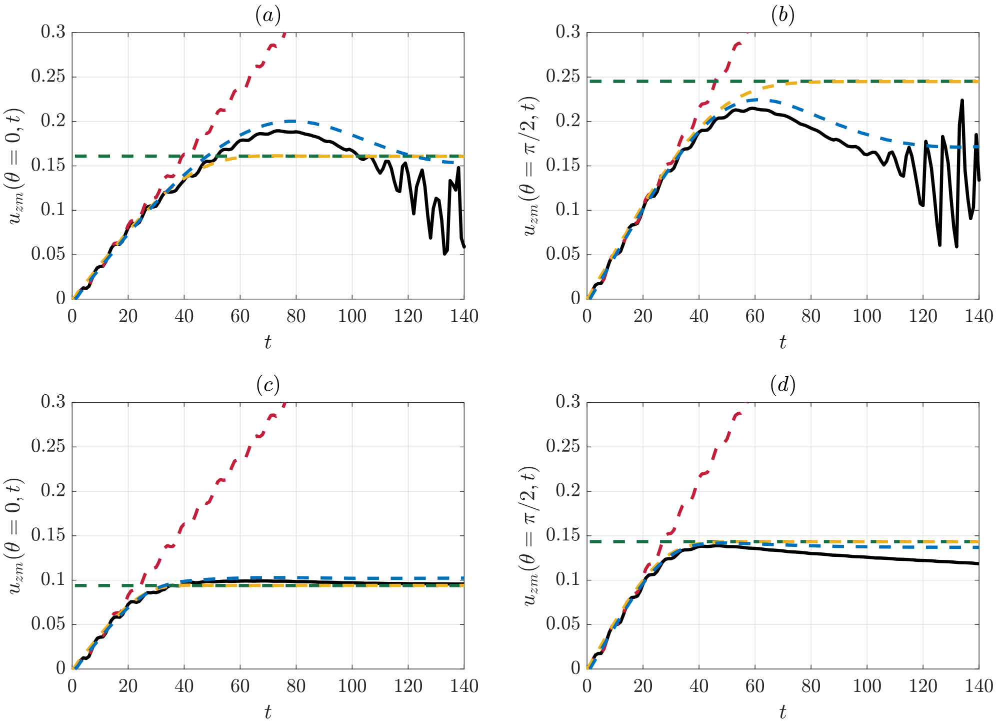

Fig. 3.9: Comparison between the maximum vertical velocity in the DNS (black solid line), predicted by the unsteady inviscid solution (3.19a) (red dashed line), by the unsteady viscous solution (3.25a,3.30) (yellow dashed line), by the steady viscous solution (3.25a,3.32) (green dashed line) and by the non-linear equations (3.54,3.56) (blue dashed line) for (*a*) $\theta = 0$ and (*b*) $\theta = \pi/2$ for $Re = 10000$, $F_h = 2$, $Ro = 20.3$, $\phi = 80°$ and for (*c*) $\theta = 0$ and (*d*) $\theta = \pi/2$ for $Re = 2000$, $F_h = 2$, $Ro = 20.3$, $\phi = 80°$ ($\widetilde{Ro} = 115.2$).

Figure 3.11 shows again the vertical velocity profiles observed in the DNS for the same parameters, but for $t \geq \mathcal{T}$ this time they are compared to the unsteady and steady viscous solutions (3.30) (yellow dashed lines) and (3.32) (green dashed lines) as well as the predictions of the non-linear equations (3.54,3.56) (blue dashed lines). At $t = 40$ (figures 3.11(a, d)), the steady viscous solution (3.32) (green dashed lines) is already in good agreement with the DNS since $t = 40$ is close to the time $\mathcal{T}$ where the transition from (3.19a) to (3.32) occurs (figures 3.9(a, b)). Nevertheless, it departs slightly from the DNS near r_c unlike the unsteady viscous solution (3.30) and non-linear predictions from (3.54,3.56). At longer times, $t = 60$ (figures 3.11(b, e)) and $t = 80$ (figures 3.11(c, f)), (3.30) and (3.32) become almost identical and remain in satisfactory agreement with the vertical velocity profiles of the DNS. Nevertheless, we can see a shift between the numerical and theoretical profiles. In contrast, the solution of the non-linear equations (3.54,3.56) remains in very good agreement with the DNS and does not exhibit such shift. This indicates that the shift is due to the viscous and non-linear variations of the angular velocity. For example, this makes the critical radius where $\Omega(r_c) = 1/F_h$ to move towards the vortex center as seen in figure 3.11. This phenomenon is absent from the linear equations (3.30,3.32) since they do not take into account any variation of the angular velocity.

3.5.2 Vertical vorticity

The asymptotic analyses have shown that the axisymmetric component of the vertical velocity is given by $\zeta = \zeta_0(r) + \varepsilon^2 \zeta_{20}(r, t) + ...$, where ζ_{20} follows (3.40) and (3.44) in the inviscid and viscous regimes, i.e. $t \leq \mathcal{T}$ and $t \geq \mathcal{T}$, respectively. A global view of these two regimes and the associated approximations can be gained by plotting $\partial\zeta_{20}/\partial r$ at $r = r_c$ (figure 3.12). The black solid line shows the evolution of $\partial\zeta_{20}/\partial r(r_c, t)$ computed numerically from (3.44). $\partial\zeta_{20}/\partial r(r_c, t)$ increases initially like t^4 in agreement with the approximation (3.42) (red dashed line). Subsequently, for $t \gg \mathcal{T}$, $\partial\zeta_{20}/\partial r(r_c, t)$ increases more slowly and saturates towards $\partial\zeta_{20}^{(1)}/\partial r(r_c)$ (black dashed line) for $t \to \infty$. The approximation (3.45) (blue dashed line) is in good agreement with the solution (3.44) (black line) in this regime. It will allow us to derive a theoretical criteria for the onset of non-axisymmetry in section 3.6.4.

Figure 3.13 compares the radial profile of the theoretical vorticity $\zeta = \zeta_0(r) + \varepsilon^2 \zeta_{20}(r, t) + ...$ with ζ_{20} given by the unsteady inviscid solution (3.40) (red dashed line) to the DNS when $t \leq \mathcal{T}$. The agreement is excellent and predicts very well the deformation of the vertical vorticity profile near $r_c \simeq 1.2$. A similar comparison is displayed in figure 3.14 for three different times such that $t \gtrsim \mathcal{T}$ and ζ_{20} given by the unsteady viscous solution (3.44). The agreement continues to be very good even for $t = 85$ (figure 3.14(c)), confirming the validity of the solution (3.44). A slight shift can be however noticed near r_c and near the vortex axis. In contrast, the predictions of the non-linear equations (3.54,3.56) (blue dashed lines) are in very good agreement with the DNS near r_c. This shows again that non-linear effects are not negligible in the critical layer.

Finally, the prediction for late time $t \gg \mathcal{T}$ based on the steady viscous solution (3.45) has been compared to a DNS for a larger non-traditional Rossby number $\widetilde{Ro} =$

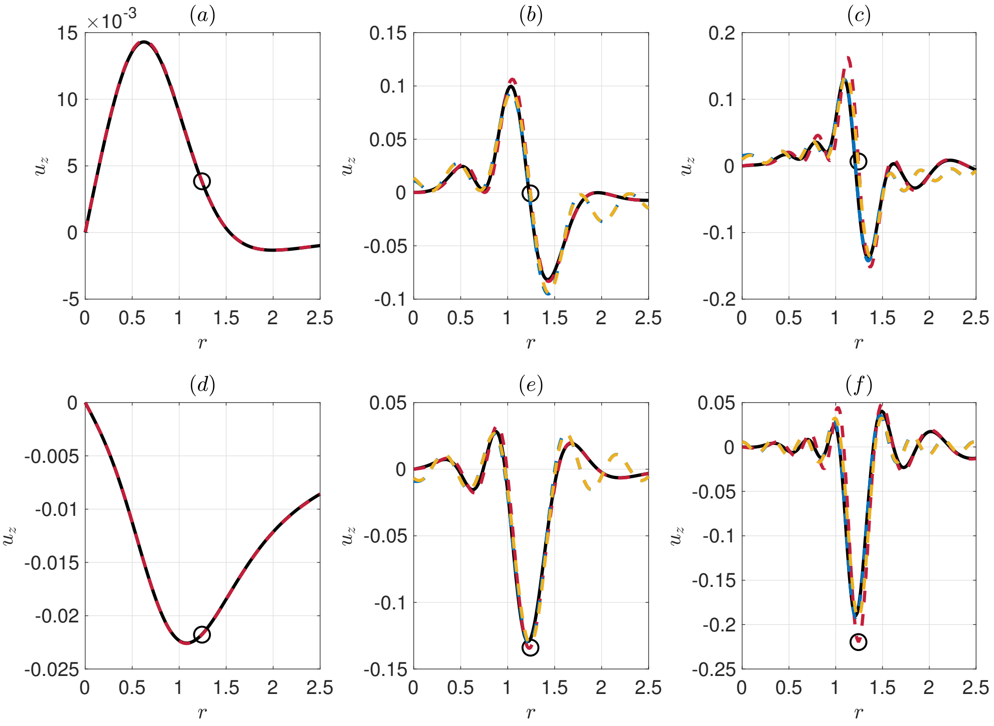

Fig. 3.10: Comparison between the vertical velocity at $\theta = 0$ (top row) and $\theta = \pi/2$ (bottom row) in the DNS (black solid line), predicted by the unsteady inviscid solution (3.19a) (red dashed line), by the unsteady viscous solution (3.30) (yellow dashed line) and by the non-linear equations (3.54,3.56) (blue dashed line) at (a,d) $t = 5$, (b,e) $t = 25$ and (c,f) $t = 40$ for $Re = 10000$, $F_h = 2$, $Ro = 20.3$, $\phi = 80°$ ($\widetilde{Ro} = 115.2$). The circle symbols represent the location of the critical radius in the unsteady inviscid solution (3.19a).

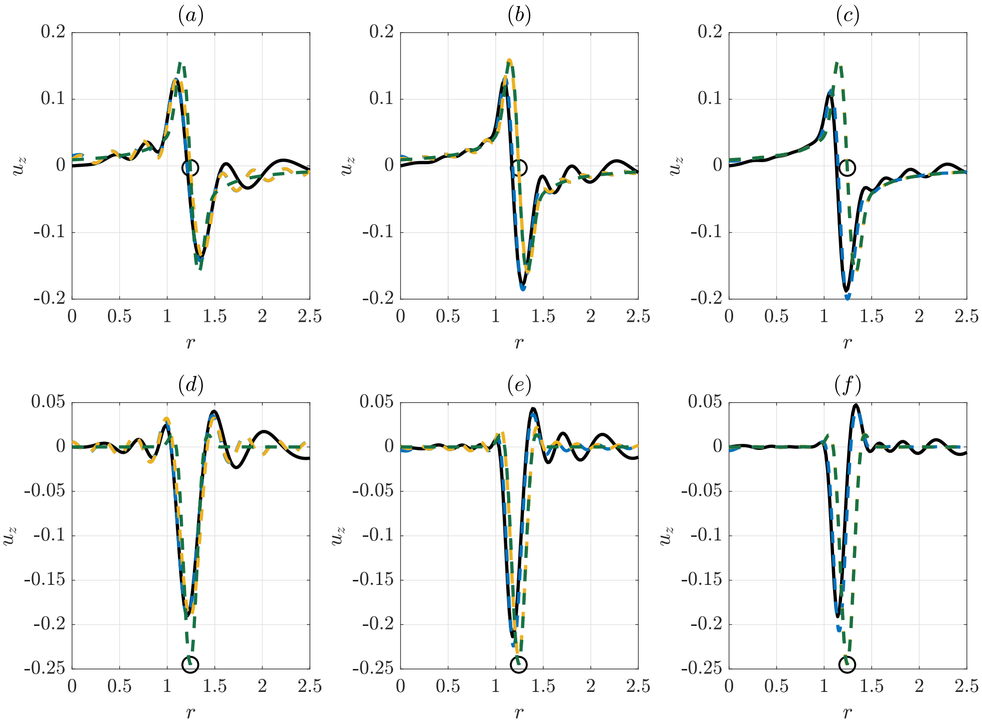

Fig. 3.11: Comparison between the vertical velocity at $\theta = 0$ (top row) and $\theta = \pi/2$ (bottom row) in the DNS (black solid line), predicted by the unsteady viscous solution (3.25a,3.30) (yellow dashed line), by the steady viscous solution (3.25a,3.32) (green dashed line) and by the non-linear equations (3.54,3.56) (blue dashed line) at (a, d) $t = 40$, (b, e) $t = 60$, (c, f) $t = 80$ for $Re = 10000$, $F_h = 2$, $Ro = 20.3$, $\phi = 80°$ ($\widetilde{Ro} = 115.2$). The circle symbols represent the location of the critical radius in the unsteady viscous solution (3.25a).

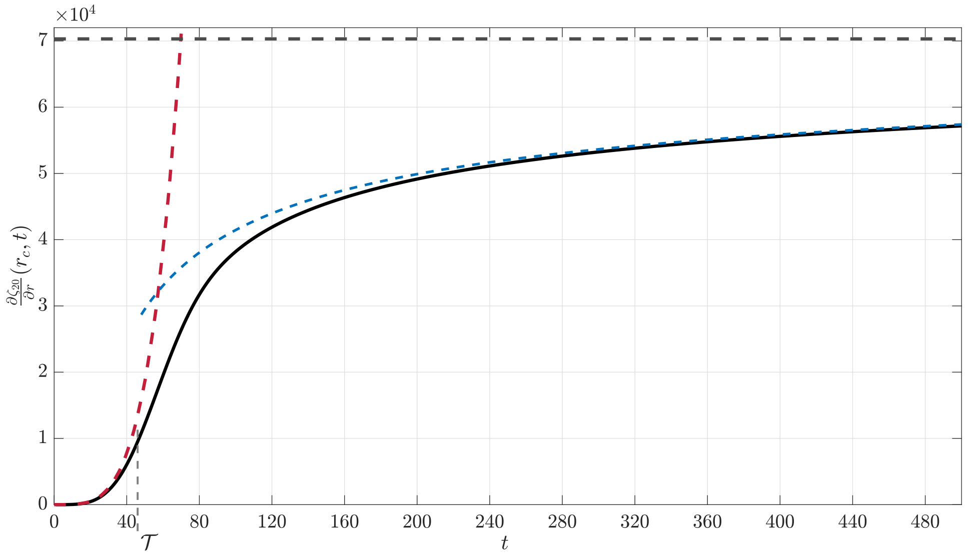

Fig. 3.12: Comparison between the evolution of $\partial\zeta_{20}/\partial r(r_c, t)$ from the theoretical expressions: the unsteady viscous solution (3.44) (Black solid line), the unsteady inviscid solution (3.40) (red dashed line), the viscous solutions (3.45) (blue dashed line) and (3.46a) (black dashed line) for $Re = 10000$, $F_h = 2$.

500, the other parameters being identical. The vortex remains then quasi-axisymmetric in the DNS (figure 3.8) allowing us to see the late evolution of the vorticity without the non-axisymmetric perturbations. Figure 3.15 shows that the deformation of the vorticity profile near r_c is weak but well predicted by (3.45) although there is a shift for $t \geq 300$. In this case, the predictions from the non-linear equations (3.54,3.56) (not shown) are identical to those from (3.45) indicating that the non-linear effects are weak. However, if we take also into account the global viscous decay of the leading order vorticity ζ_0 which is significant for these large times, then the agreement with the DNS is perfect (yellow dashed line).

Besides, a feature of high interest is that the vertical vorticity profile exhibits two extrema near r_c, $d\zeta/dr = 0$, as soon as $t \geq 40$ (figures 3.13(*c*) and 3.14). According to the Rayleigh's inflectional criterion (Rayleigh, 1880), this is a necessary condition for the shear instability. However, only the first extremum, where ζ has a local minimum, satisfies the stiffer Fjørtoft (1950) instability condition $[\Omega(r) - \Omega(r_I)]\partial\zeta/\partial r < 0$, where r_I is the extremum. This gives us hindsight on the possible origin of the late non-axisymmetric evolution of the vertical vorticity. The next section will investigate whether or not this hypothesis is correct.

3.6 Analysis of the non-axisymmetric evolution

As seen in the previous sections, a ring of anomalous vertical vorticity develops near the critical radius and, subsequently, this ring may become non-axisymmetric when the non-traditional Rossby number $\widetilde{Ro}$ is below a critical value depending on the Reynolds

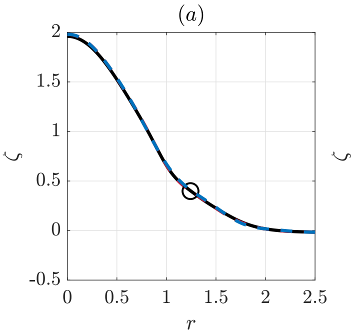

Fig. 3.13: Comparison between the vertical vorticity at $\theta = \pi/2$ in the DNS (black solid line) and the asymptotic expressions $\zeta = \zeta_0 + \varepsilon^2\zeta_{20}$ where ζ_{20} follows the unsteady inviscid solution (3.40) (red dashed line) and $\zeta = \zeta_0 + \zeta_1$ with ζ_1 given by the non-linear equations (3.54,3.56) (blue dashed line) at (*a*) $t = 25$, (*b*) $t = 35$ and (*c*) $t = 40$ for $Re = 10000$, $F_h = 2$, $Ro = 20.3$, $\phi = 80°$ ($\widetilde{Ro} = 115.2$). The circle symbols represent the location of the critical radius in the unsteady inviscid solution (3.40).

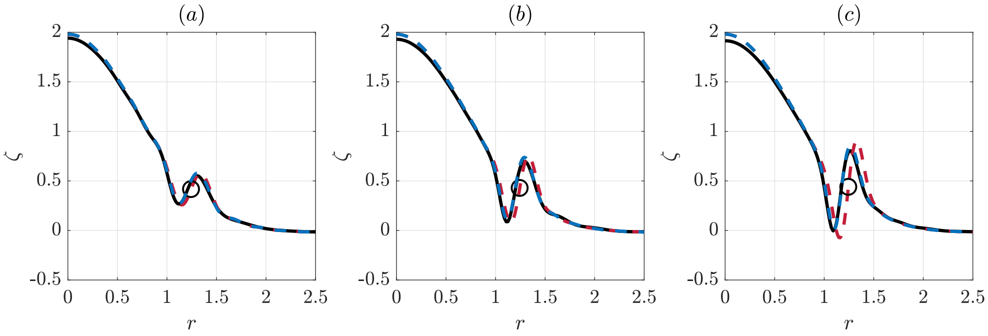

Fig. 3.14: Comparison between the vertical vorticity at $\theta = \pi/2$ in the DNS (black solid line) and the asymptotic expressions $\zeta = \zeta_0 + \varepsilon^2\zeta_{20}$ where ζ_{20} follows the unsteady viscous solution (3.44) (red dashed line) and $\zeta = \zeta_0 + \zeta_1$ with ζ_1 given by the non-linear equations (3.54,3.56) (blue dashed line) at (*a*) $t = 50$, (*b*) $t = 65$ and (*c*) $t = 85$ for $Re = 10000$, $F_h = 2$, $Ro = 20.3$, $\phi = 80°$ ($\widetilde{Ro} = 115.2$). The circle symbols represent the location of the critical radius in the unsteady inviscid solution (3.44).

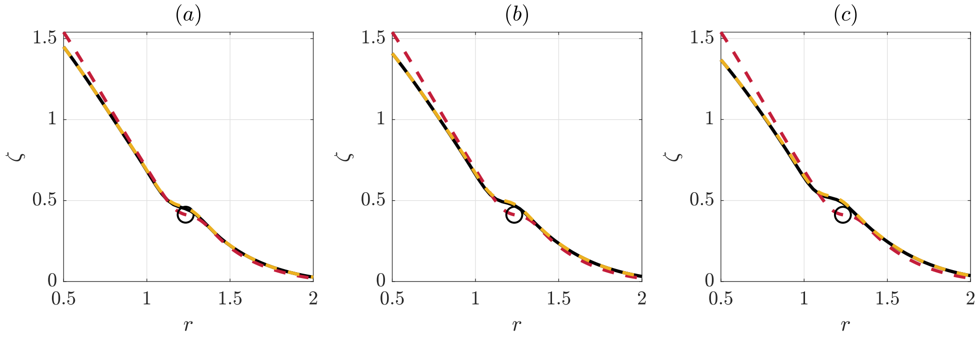

Fig. 3.15: Comparison between the vertical vorticity at $\theta = \pi/2$ in the DNS (black solid line) and the asymptotic expressions $\zeta = \zeta_0 + \varepsilon^2\zeta_{20}$ where ζ_{20} follows the viscous solution (3.45) (red dashed line) and $\zeta = \zeta_0 + \zeta_1$ with ζ_1 given by the non-linear equations (3.54,3.56) and the viscous decay of ζ_0 also taken into account (yellow dashed line) at (*a*) $t = 200$, (*b*) $t = 300$ and (*c*) $t = 400$ for $Re = 10000$, $F_h = 2$, $Ro = 20.0$, $\phi = 87.7°$ ($\widetilde{Ro} = 500$). The circle symbols represent the location of the critical radius in the viscous solution (3.45).

number (figure 3.8). In this section, the main question is: what is the origin of this non-axisymmetric evolution? Is it due to a shear instability associated to the inflection point in the vertical vorticity profile (see figure 3.14)? or is it an intrinsic behaviour of the vortex under the complete Coriolis force? Regarding the latter hypothesis, we have seen indeed from (3.36-3.38) that the vertical velocity field forces not only an axisymmetric vertical vorticity field but also a non-axisymmetric one with an azimuthal wavenumber $m = 2$.

3.6.1 Azimuthal decomposition of ζ and u_z

In order to better understand the onset of non-axisymmetric vertical vorticity, we have first decomposed ζ thanks to an azimuthal Fourier transform

$$\hat{\zeta}_m(r,t) = \int_0^{2\pi} \zeta(r,\theta,t)e^{-im\theta}\mathrm{d}\theta, \tag{3.58}$$

where $\zeta(x,y,t)$ has been first interpolated on a grid of cylindrical coordinates (r,θ). The same transform has been applied to u_z in order to obtain $\hat{u}_{z_m}$. The mean power in each azimuthal wavenumber is then defined as

$$E_\zeta(m,t) = \frac{\displaystyle\int_0^{l_x/2} \hat{\zeta}_m^2(r,t)r\mathrm{d}r}{\displaystyle\int_0^{l_x/2} r\mathrm{d}r} = \frac{8}{l_x^2}\int_0^{l_x/2} \hat{\zeta}_m^2(r,t)r\mathrm{d}r, \tag{3.59}$$

and

$$E_{u_z}(m,t) = \frac{8}{l_x^2}\int_0^{l_x/2} \hat{u}_{z_m}^2(r,t)r\mathrm{d}r. \tag{3.60}$$

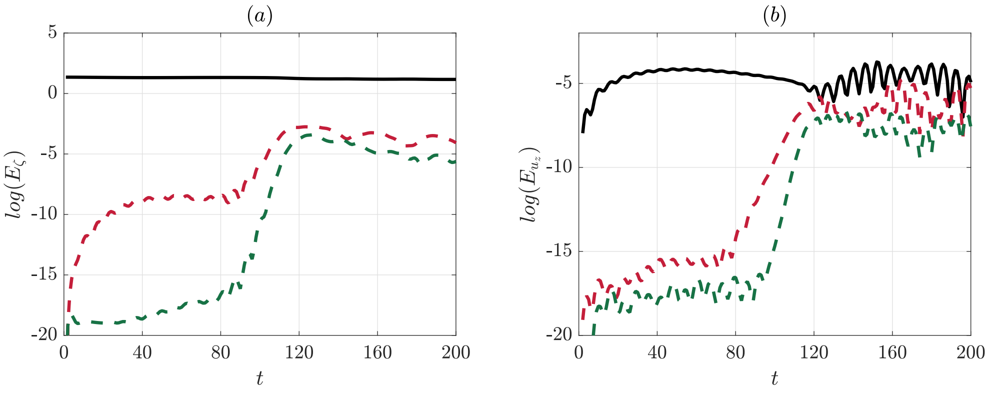

Fig. 3.16: Evolution of the power (a) $E_\zeta(m,t)$ for the azimuthal wavenumbers $m=0$ (black solid line), $m=2$ (red dashed line) and $m=4$ (green dashed line) and the power (b) $E_{u_z}(m,t)$ for the azimuthal wavenumbers $m=1$ (black solid line), $m=3$ (red dashed line) and $m=5$ (green dashed line) for $Re=10000$, $F_h=2$, $Ro=20.3$ and $\phi=80°$ ($\widetilde{Ro}=115.2$).

Figure 3.16(a) displays the evolution of the logarithm of the power of the first three azimuthal wavenumbers of the vertical vorticity. These are only even, i.e. $m=0$, $m=2$, $m=4$. Similarly, figure 3.16(b) shows the logarithm of the power of the first three azimuthal wavenumbers of u_z. They are odd in this case: $m=1$, $m=3$, $m=5$. It can be seen that $E_\zeta(0,t)$ and $E_{u_z}(1,t)$ (black solid lines) remain approximately constant except that $E_{u_z}(1,t)$ sustains large oscillation after $t\simeq 120$.

It is also worth to point out that $E_\zeta(2,t)$ starts to grow at the beginning of the simulation since ζ_{22} increases like t^2 due to the forcing by the vertical velocity as shown in §3.4.3 (figure 3.16 (b)). However, when $t\leq 80$, its power remains negligible compared to the one of the axisymmetric mode, $E_\zeta(0,t)$. In contrast, after $t\simeq 80$, $E_\zeta(2,t)$ grows exponentially before saturating at $t\geq 120$. There is therefore a clear transition towards an exponential growth, a feature consistent with the instability hypothesis. Nevertheless, we can see that the azimuthal mode $m=3$ of u_z (figure 3.16(b)) grows also exponentially at the same time. The higher modes, $m=4$ of ζ and $m=5$ of u_z, start to increase also exponentially but somewhat later. Thus, it is unclear if the growth of $E_{u_z}(3,t)$ is a consequence of the growth of $E_\zeta(2,t)$, if it is the opposite, or if the exponential growth is due to a coupling between $E_{u_z}(3,t)$ and $E_\zeta(2,t)$.

3.6.2 Truncated model

To answer the latter question, we have derived a truncated model taking into account only the first azimuthal wavenumbers of each quantity. More precisely, the different variables have been written as

$$u_r=\hat{u}_{r_{2c}}(r,t)\cos(2\theta)+\hat{u}_{r_{2s}}(r,t)\sin(2\theta), \tag{3.61a}$$

$$u_\theta=\hat{u}_{\theta_0}(r,t)+\hat{u}_{\theta_{2c}}(r,t)\cos(2\theta)+\hat{u}_{\theta_{2s}}(r,t)\sin(2\theta), \tag{3.61b}$$

$$p(r,\theta) = \hat{p}_0(r,t) + \hat{p}_{2c}(r,t)\cos(2\theta) + \hat{p}_{2s}(r,t)\sin(2\theta), \tag{3.61c}$$

$$\zeta = \hat{\zeta}_0(r,t) + \hat{\zeta}_{2c}(r,t)\cos(2\theta) + \hat{\zeta}_{2s}(r,t)\sin(2\theta), \tag{3.61d}$$

$$u_z = \hat{u}_{z_{1c}}(r,t)\cos(\theta) + \hat{u}_{z_{1s}}(r,t)\sin(\theta), \tag{3.61e}$$

$$b = \hat{b}_{1c}(r,t)\cos(\theta) + \hat{b}_{1s}(r,t)\sin(\theta). \tag{3.61f}$$

These decompositions have been introduced in (3.10a-3.10e) and the following governing equations have been obtained for the vertical velocity and buoyancy by truncating all the higher modes:

$$\begin{aligned}\frac{\partial \hat{u}_{z_{1c}}}{\partial t} =& -\frac{1}{2}\left(\hat{u}_{r_{2c}}\frac{\partial \hat{u}_{z_{1c}}}{\partial r} + \hat{u}_{r_{2s}}\frac{\partial \hat{u}_{z_{1s}}}{\partial r}\right) - \frac{1}{r}\left(\hat{u}_{\theta_0}\hat{u}_{z_{1s}} + \frac{1}{2}(\hat{u}_{\theta_{2c}}\hat{u}_{z_{1s}} - \hat{u}_{\theta_{2s}}\hat{u}_{z_{1c}})\right)\\ &+ \hat{b}_{1c} + \frac{1}{Re}\nabla^2\hat{u}_{z_{1c}} + \frac{1}{\widetilde{Ro}}(\hat{u}_{r_{2c}} - \hat{u}_{\theta_{2s}}),\end{aligned} \tag{3.62a}$$

$$\begin{aligned}\frac{\partial \hat{u}_{z_{1s}}}{\partial t} =& \frac{1}{2}\left(\hat{u}_{r_{2c}}\frac{\partial \hat{u}_{z_{1s}}}{\partial r} - \hat{u}_{r_{2s}}\frac{\partial \hat{u}_{z_{1c}}}{\partial r}\right) + \frac{1}{r}\left(\hat{u}_{\theta_0}\hat{u}_{z_{1c}} - \frac{1}{2}(\hat{u}_{\theta_{2c}}\hat{u}_{z_{1c}} + \hat{u}_{\theta_{2s}}\hat{u}_{z_{1s}})\right)\\ &+ \hat{b}_{1s} + \frac{1}{Re}\nabla^2\hat{u}_{z_{1s}} + \frac{1}{\widetilde{Ro}}(\hat{u}_{r_{2s}} + \hat{u}_{\theta_{2c}} - 2\hat{u}_{\theta_0}),\end{aligned} \tag{3.62b}$$

$$\begin{aligned}\frac{\partial \hat{b}_{1c}}{\partial t} =& -\frac{1}{2}\left(\hat{u}_{r_{2c}}\frac{\partial \hat{b}_{1c}}{\partial r} + \hat{u}_{r_{2s}}\frac{\partial \hat{b}_{1s}}{\partial r}\right) - \frac{1}{r}\left(\hat{u}_{\theta_0}\hat{b}_{1s} + \frac{1}{2}(\hat{u}_{\theta_{2c}}\hat{b}_{1s} - \hat{u}_{\theta_{2s}}\hat{b}_{1c})\right)\\ &- \frac{\hat{u}_{z_{1c}}}{F_h^2} + \frac{1}{ReSc}\nabla^2\hat{b}_{1c},\end{aligned} \tag{3.62c}$$

$$\begin{aligned}\frac{\partial \hat{b}_{1s}}{\partial t} =& \frac{1}{2}\left(\hat{u}_{r_{2c}}\frac{\partial \hat{b}_{1s}}{\partial r} - \hat{u}_{r_{2s}}\frac{\partial \hat{b}_{1c}}{\partial r}\right) + \frac{1}{r}\left(\hat{u}_{\theta_0}\hat{b}_{1c} - \frac{1}{2}(\hat{u}_{\theta_{2c}}\hat{b}_{1c} + \hat{u}_{\theta_{2s}}\hat{b}_{1s})\right)\\ &- \frac{\hat{u}_{z_{1s}}}{F_h^2} + \frac{1}{ReSc}\nabla^2\hat{b}_{1s}.\end{aligned} \tag{3.62d}$$

Applying the same truncation approach for the vertical vorticity gives

$$\begin{aligned}\frac{\partial \hat{\zeta}_0}{\partial t} =& -\frac{1}{2}\left(\hat{u}_{r_{2c}}\frac{\partial \hat{\zeta}_{2c}}{\partial r} + \hat{u}_{r_{2s}}\frac{\partial \hat{\zeta}_{2s}}{\partial r}\right) - \frac{1}{r}\left(\hat{u}_{\theta_{2c}}\hat{\zeta}_{2s} - \hat{u}_{\theta_{2s}}\hat{\zeta}_{2c}\right) + \frac{1}{Re}\nabla^2\hat{\zeta}_0,\\ &+ \frac{1}{\widetilde{Ro}}\left(\frac{\partial \hat{u}_{z_{1s}}}{\partial r} + \frac{\hat{u}_{z_{1s}}}{r}\right)\end{aligned} \tag{3.63a}$$

$$\frac{\partial \hat{\zeta}_{2c}}{\partial t} = -\hat{u}_{r_{2c}}\frac{\partial \hat{\zeta}_0}{\partial r} - \frac{2\hat{u}_{\theta_0}}{r}\hat{\zeta}_{2s} + \frac{1}{Re}\nabla^2\hat{\zeta}_{2c} - \frac{1}{\widetilde{Ro}}\left(\frac{\partial \hat{u}_{z_{1s}}}{\partial r} - \frac{\hat{u}_{z_{1s}}}{r}\right), \tag{3.63b}$$

$$\frac{\partial \hat{\zeta}_{2s}}{\partial t} = -\hat{u}_{r_{2s}}\frac{\partial \hat{\zeta}_0}{\partial r} + \frac{2\hat{u}_{\theta_0}}{r}\hat{\zeta}_{2c} + \frac{1}{Re}\nabla^2 + \frac{1}{\widetilde{Ro}}\left(\frac{\partial \hat{u}_{z_{1c}}}{\partial r} - \frac{\hat{u}_{z_{1c}}}{r}\right), \tag{3.63c}$$

where

$$\hat{\zeta}_0 = \frac{1}{r}\frac{\partial r\hat{u}_{\theta_0}}{\partial r}, \tag{3.64a}$$

$$\hat{\zeta}_{2c} = \frac{1}{r}\frac{\partial r\hat{u}_{\theta_{2c}}}{\partial r} - \frac{2}{r}\hat{u}_{r_{2s}}, \tag{3.64b}$$

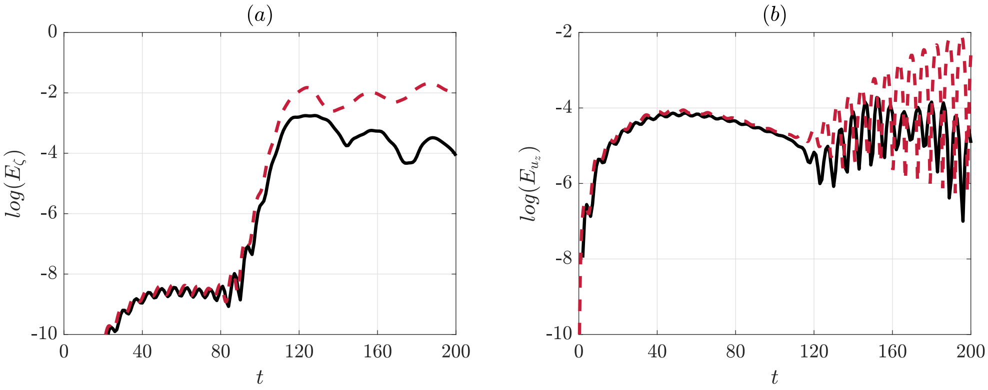

Fig. 3.17: Evolution of the power (a) $E_\zeta(2,t)$ and (b) $E_{u_z}(1,t)$ in the DNS (black solid line) and in the truncated model (red dashed line) for $Re = 10000$, $F_h = 2$, $Ro = 20.3$ and $\phi = 80°$ $(\widetilde{Ro} = 115.2)$.

$$\hat{\zeta}_{2s} = \frac{1}{r}\frac{\partial r \hat{u}_{\theta_{2s}}}{\partial r} + \frac{2}{r}\hat{u}_{r_{2c}}. \tag{3.64c}$$

The divergence equation also implies

$$\frac{1}{r}\frac{\partial r \hat{u}_{r_{2c}}}{\partial r} + \frac{2}{r}\hat{u}_{\theta_{2s}} = 0, \tag{3.65a}$$

$$\frac{1}{r}\frac{\partial r \hat{u}_{r_{2s}}}{\partial r} - \frac{2}{r}\hat{u}_{\theta_{2c}} = 0. \tag{3.65b}$$

Such truncated model can be seen as a heuristic extension of the asymptotic analyses. Indeed, it takes into account both time dependence and diffusive effects in the evolution of the vertical velocity and buoyancy (3.62). Moreover, the modifications of the axisymmetric flow field $(\hat{u}_{\theta_0})$ and the generated $m = 2$ mode $(\hat{u}_{r_{2c}}, \hat{u}_{r_{2s}}, \hat{u}_{\theta_{2c}}, \hat{u}_{\theta_{2s}})$ are also taken into account. The latter is governed by (3.63b-3.63c) and it appears also in the evolution of the axisymmetric flow field (3.63a). However, like in the asymptotic analyses, only the first azimuthal wavenumber of u_z and b are considered, i.e. the mode $m = 3$, $m = 5$, ... are neglected. Similarly, the higher modes $m = 4$, $m = 6$, ... are neglected in the evolution of the horizontal flow field (3.63).

Figures 3.17 (a, b) compares the power $E_\zeta(2,t)$ and $E_{u_z}(1,t)$, respectively, obtained in the DNS and in the truncated model. There are some differences for $t \geq 100$ but, qualitatively, the same type of evolution as in the DNS is obtained with the truncated model. This is remarkable since the truncated model crudely neglects many azimuthal modes and, in particular, the azimuthal mode $m = 3$ in the vertical velocity and buoyancy fields. Hence, this proves that the growth of $E_{u_z}(3,t)$ in figure 3.16(b) does not play a key role in the onset of non-axisymmetry in the vertical vorticity.

We can make a step further in the understanding of this phenomenon by freezing the axisymmetric velocity field. In other words, the time evolution of $(\hat{u}_{\theta_0}, \hat{\zeta}_0)$ is suppressed after a given time t_f. We also set the forcing terms due to the non-traditional Coriolis force to be zero in (3.63b) and (3.63c). Hence, the latter equations become

$$\frac{\partial \hat{\zeta}_{2c}}{\partial t} = -\hat{u}_{r_{2c}}\frac{\partial \hat{\zeta}_0(r,t_f)}{\partial r} - \frac{2\hat{u}_{\theta_0}(r,t_f)}{r}\hat{\zeta}_{2s} + \frac{1}{Re}\nabla^2\hat{\zeta}_{2c}, \tag{3.66a}$$

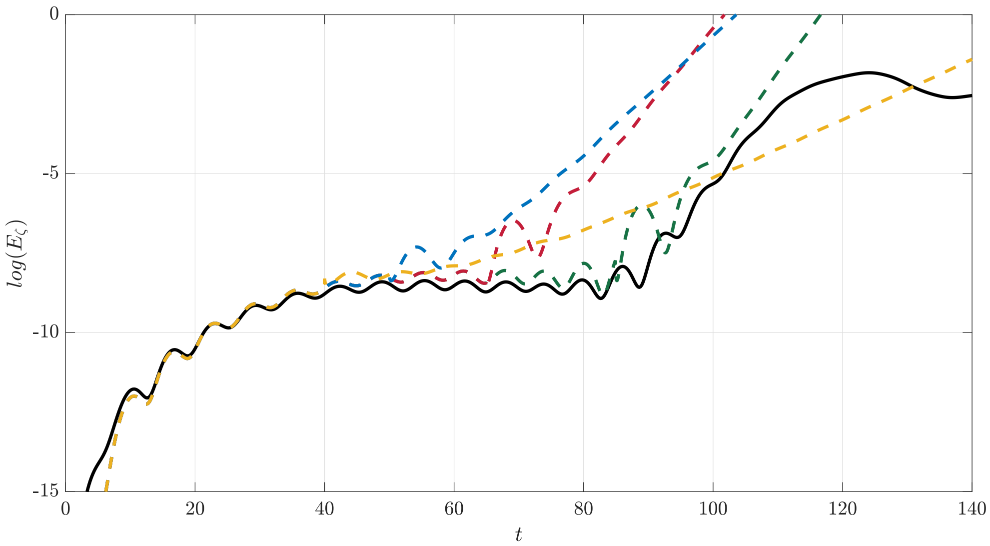

Fig. 3.18: Evolution of the power $E_\zeta(2,t)$ in the truncated model (black solid line) or using (3.66) for different freezing times: $t_f = 85$ (green dashed line), $t_f = 65$ (red dashed line), $t_f = 50$ (blue dashed line) and $t_f = 40$ (yellow dashed line) for $Re = 10000$, $F_h = 2$, $Ro = 20.3$ and $\phi = 80°$ ($\widetilde{Ro} = 115.2$).

$$\frac{\partial \hat{\zeta}_{2s}}{\partial t} = -\hat{u}_{r_{2s}} \frac{\partial \hat{\zeta}_0(r,t_f)}{\partial r} + \frac{2\hat{u}_{\theta_0}(r,t_f)}{r}\hat{\zeta}_{2c} + \frac{1}{Re}\nabla^2 \hat{\zeta}_{2s}. \tag{3.66b}$$

These equations describe simply the linear evolution of perturbations with azimuthal wavenumber $m = 2$ on a steady axisymmetric vortex with azimuthal velocity $\hat{u}_{\theta_0}(r,t_f)$. The perturbations $(\hat{u}_{r_{2c}}, \hat{u}_{\theta_{2c}})$ and $(\hat{u}_{r_{2s}}, \hat{u}_{\theta_{2s}})$ are initialized by a white noise whose amplitude is adjusted so as to have a power of the same order as $E_\zeta(2,t_f)$. Figure 3.18 shows the evolution of the power $E_\zeta(2,t)$ for different freezing time t_f; $t_f = 40$ (yellow dashed line), $t_f = 50$ (blue dashed line), $t_f = 65$ (red dashed line), $t_f = 85$ (green dashed line) compared to the evolution of $E_\zeta(2,t)$ in the truncated model (black solid line). Strikingly, we see that $E_\zeta(2,t)$ grows also exponentially regardless of the value of t_f investigated. Furthermore, the growth rate, i.e. the slope, increases with t_f. Most interestingly, the growth rate for $t_f = 85$ is close to the one observed in the truncated model (black solid line). This demonstrates that the onset of non-axisymmetry in the vertical vorticity is due to an instability of the vortex profile. When the anomaly of vertical vorticity is sufficient to have an extremum, a shear instability with an azimuthal wavenumber $m = 2$ develops. Subsequently, this triggers the growth of higher azimuthal modes through the coupling with the non-traditional Coriolis force.

3.6.3 Equivalent vortex with piecewise uniform vorticity

A simple model of the instability can be obtained by considering the inviscid limit and by using a vortex with piecewise uniform vorticity with four concentric regions as considered by Carton & Legras (1994) and Kossin *et al.* (2000). As shown by two examples in figure 3.19, the vorticity profile in the DNS can be crudely approximated by four levels of constant vorticity:

$$\zeta = \begin{cases} \zeta_1 = 2 & 0 < r < r_1 \\ \zeta_2 = \zeta_c - \delta_v/2 & r_1 < r < r_2 \\ \zeta_3 = \zeta_c + \delta_v/2 & r_2 < r < r_3 \\ \zeta_4 = 0 & r_3 < r \end{cases} \tag{3.67}$$

where $r_1 = r_c - \delta_h$, $r_2 = r_c$ and $r_3 = r_c + \delta_h$ where δ_v and δ_h are the amplitude and size of the vorticity anomaly in the vicinity of the critical radius r_c. More explicitly, δ_v is the difference between the local maximum and minimum of the vorticity and δ_h is the distance between these two extrema. The corresponding angular velocity of the vortex is continuous and given by

$$\Omega(r) = \frac{1}{2}\begin{cases} \zeta_1 & 0 < r < r_1 \\ \zeta_2 - (\zeta_2 - \zeta_1)(r_1/r)^2 & r_1 < r < r_2 \\ \zeta_3 - (\zeta_2 - \zeta_1)(r_1/r)^2 - (\zeta_3 - \zeta_2)(r_2/r)^2 & r_2 < r < r_3 \\ -(\zeta_2 - \zeta_1)(r_1/r)^2 - (\zeta_3 - \zeta_2)(r_2/r)^2 + \zeta_3(r_3/r)^2 & r_3 < r \end{cases} \tag{3.68}$$

For a given Froude number F_h, the position of the critical radius r_c and the value of ζ_c are fixed. Hence, the problem has only two control parameters: δ_v and δ_h. The stability of such vortex with respect to perturbations of the form $\psi e^{im\theta+\sigma t}$ is governed by the eigenvalue problem (Carton & Legras, 1994; Kossin *et al.*, 2000)

$$\begin{pmatrix} m\Omega(r_1) + \frac{1}{2}(\zeta_2 - \zeta_1) & \frac{1}{2}(\zeta_2 - \zeta_1)(r_1/r_2)^m & \frac{1}{2}(\zeta_2 - \zeta_1)(r_1/r_3)^m \\ \frac{1}{2}(\zeta_3 - \zeta_2)(r_1/r_2)^m & m\Omega(r_2) + \frac{1}{2}(\zeta_3 - \zeta_2) & \frac{1}{2}(\zeta_3 - \zeta_2)(r_2/r_3)^m \\ -\frac{1}{2}\zeta_3(r_1/r_3)^m & -\frac{1}{2}\zeta_3(r_2/r_3)^m & m\Omega(r_3) - \frac{1}{2}\zeta_3 \end{pmatrix} \begin{pmatrix} \psi_1 \\ \psi_2 \\ \psi_3 \end{pmatrix} = \sigma \begin{pmatrix} \psi_1 \\ \psi_2 \\ \psi_3 \end{pmatrix}. \tag{3.69}$$

Figure 3.20 (*a*) shows the growth rate contours for the $m = 2$ perturbations for $F_h = 2$ as a function of (δ_v, δ_h). We see that the growth rate is positive only when δ_v and δ_h are sufficiently away from zero in the ranges investigated. The symbols in figure 3.20(*a*) indicate the parameters (δ_v, δ_h) estimated by fitting (3.67) to the vorticity field $\hat{\zeta}_0(r, t_f)$ at different times t_f for $F_h = 2$, for two different latitudes $\phi = 80°$ (red circles) and $\phi = 75°$ (black squares). For example, for $\phi = 80°$, the time t_f varies from $t_f = 45$ (leftmost point) to $t_f = 85$ (rightmost point). The size of the vorticity anomaly δ_h does not vary very much and is around $\delta_h \simeq 0.2$ for both latitudes. In contrast, the amplitude of the anomaly δ_v increases with t_f as expected. Figure 3.20(*b*) displays the growth rate as a function of δ_v (circle and square symbols). The dashed lines show the corresponding growth rate computed from (3.66), i.e. by considering the continuous vorticity profile $\hat{\zeta}_0(r, t_f)$ and with the perturbations initialized by white noise. This shows that the piecewise vortex model is able to predict quite well the growth rate of

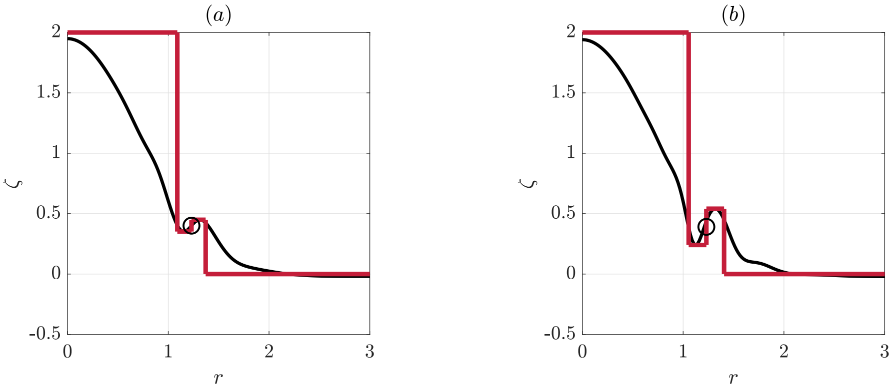

Fig. 3.19: Examples of the piecewise uniform vorticity (red line) fitting the continuous vertical vorticity profiles (black line) at (a) $t = 40$, (b) $t = 50$ for $Re = 10000$, $F_h = 2$, $Ro = 20.3$ and $\phi = 80°$ ($\widetilde{Ro} = 115.2$). The circle symbols represent the location of the critical radius.

the instability observed in the truncated model, which is itself in good agreement with the DNS.

Using (3.69), we have also computed the growth rate of higher azimuthal wavenumbers $m > 2$. The results show that the most unstable wavenumber is not $m = 2$ but is between $m = 3$ and $m = 5$ for the parameters indicated by the symbols in figure 3.20(a). Three reasons might explain the actual dominance of $m = 2$. First, the velocity jumps in the piecewise vortex model could favor larger wavenumbers compared to a continuous vorticity profile. Second, we have seen from (3.36-3.37) that the non-traditional Coriolis force generates not only an axisymmetric vorticity at order $1/\widetilde{Ro}^2$ but also a vorticity field with with an azimuthal wavenumber $m = 2$. Figure 3.17(a) shows that the latter is weak before the onset of the instability. However, it is not zero and, therefore, this small amplitude could favor its dominance over more unstable higher wavenumbers whose initial amplitudes are much lower (see $m = 4$ in figure 3.17(a)). Third, the vortex profile is continuously evolving with time while, in the stability problems (3.66) or (3.69), we have frozen this evolution. Hence, the $m = 2$ wavenumber could be selected first when the vortex becomes slightly unstable. This early selection would then ensure its subsequent dominance even if it is no longer the most unstable wavenumber. Such effect has been evidenced by Wang & Balmforth (2021) in their study of the evolution of the wavenumber selection as the critical layer becomes finer.

3.6.4 Theoretical criterion

Even if the Rayleigh-Fjørtoft criterion is only a necessary condition for the shear instability in inviscid fluids, we can try to use it to establish a theoretical criterion for the onset of the shear instability in the DNS for finite Reynolds numbers. Since the radial derivative of the vorticity is maximum at $r = r_c$ and is negative away from the critical

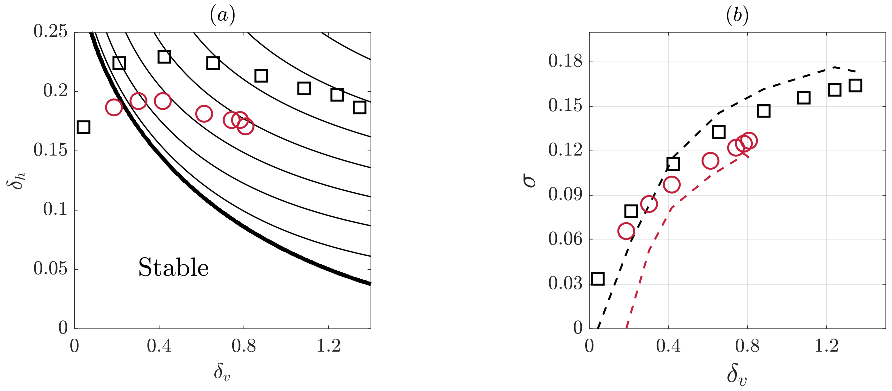

Fig. 3.20:
(a) Growth rates contours of the piecewise vortex model as a function of δ_h and δ_v for $F_h = 2$. The contour interval is 0.03. The bold line indicates the growth rate $\sigma = 0$. The symbols correspond to the values of δ_h and δ_v estimated at different freezing times for $\phi = 80°$ ($\widetilde{Ro} = 115.2$) (red circles) and $\phi = 75°$ ($\widetilde{Ro} = 77.27$) (black squares) for $Re = 10000$, $F_h = 2$.
(b) Growth rates as a function of δ_v obtained by the truncated model at different freezing times (symbols) and given by (3.69) for $m = 2$ (dashed lines) for $\phi = 75°$ ($\widetilde{Ro} = 77.27$) (black) and $\phi = 80°$ ($\widetilde{Ro} = 115.2$) (red), $Re = 10000$ and $F_h = 2$.

radius, a necessary condition ensuring that there exists extrema, $d\zeta/dr = 0$, reads

$$\frac{\mathrm{d}\zeta(r_c, t_s)}{\mathrm{d}r} \geq c, \tag{3.70}$$

where $c = 0$ is the minimum requirement for the existence of an inflection point, but we have explored also the consequences of larger values of c. Besides, the time t_s will be set as $t_s = a\mathcal{T}$, where a is a constant larger than unity. Indeed, the onset of the shear instability always occurs after the time $\mathcal{T}$. Therefore, the vorticity ζ will be taken as the asymptotic axisymmetric vorticity $\zeta = \zeta_0 + \varepsilon^2\zeta_{20}$ where ζ_{20} is given by (3.45). As seen in figure 3.12, $\partial\zeta_{20}/\partial r(r_c, t)$ is indeed well predicted by (3.45) for large times. Then, (3.70) becomes

$$\frac{Re^{2/3}}{\widetilde{Ro}} \geq \left|2\Omega_c'\right|^{1/3}\left(1+\frac{1}{Sc}\right)^{1/6}\sqrt{\frac{c-3\Omega_c'-r_c\Omega_c''}{2\pi r_c\Omega_c\left(\mathrm{Hi}(0)-\left(\frac{1+1/Sc}{8a\pi^2\mathrm{Hi}(0)}\right)^{1/2}\right)}}. \tag{3.71}$$

Remarkably, the right-hand side depends only on the Froude number through r_c, the Schmidt number S_c and the constants a and c. The criterion (3.71) when $c = 0$ and $a = \infty$ is represented by a solid line in figure 3.8. It delimits quite well the quasi-axisymmetric/non-axisymmetric domains observed in the DNS, except for the lowest Reynolds number investigated $Re = 2000$. Such difference for moderate Reynolds and Rossby numbers is not surprising since the asymptotics have been derived for high Reynolds number and large Rossby number $\widetilde{Ro}$. Furthermore, viscous effects might damp the shear instability growth when the Reynolds number is moderate.

As seen from the piecewise vortex model, the shear instability for $m = 2$ does not appear when $\delta_h \simeq 0.2$ as soon as $\delta_v > 0$. It can be roughly estimated that the instability arises only when δ_v such that $\delta_v/\delta_h \gtrsim 0.4$ (figure 3.20(a)). Therefore, we can estimate $\partial\zeta/\partial r = c \simeq \delta_v/\delta_h = 0.4$. The criterion (3.71) with this value of c and $a = \infty$ is represented by a dashed line in figure 3.8. The agreement with the DNS is as good as the criterion (3.71) with $c = 0$. The actual threshold is likely to be in between these two curves, i.e. in the hatched region (figure 3.8). Finally, we stress that the criterion (3.71) applies only to the shear instability due to an inflection point and not to other types of instability that may exist in viscous shear flows.

3.7 Late evolution of the vortex

Finally, figures 3.21 and 3.22 show the late evolution of the angular velocity profile (bottom row) when the instability develops or not, respectively. The DNS are the same as those already presented in section §3.3 for $Re = 2000$, $F_h = 2$ and different latitudes: $\phi = 60°$ ($\widetilde{Ro} = 40$) (figures 3.4 and 3.21) and $\phi = 80°$ ($\widetilde{Ro} = 115.2$) (figures 3.6 and 3.22). The corresponding vorticity fields are also shown again in the top row of figures 3.21 and 3.22 for convenience. In figures 3.21(c, d, g, h), we see that the instability ceases when the angular velocity is almost everywhere below $1/F_h$ (horizontal green dashed line), i.e. when a critical radius no longer exists. Due to the development of the critical layer and resulting instability, the decay of the angular velocity in the vortex core is accelerated compared to a pure viscous decay $\Omega = \frac{1}{r^2}(1 - \exp(\frac{-r^2}{1+4t/Re}))$ (shown by red dashed lines in figures 3.21(e, f, g, h)). When there is no instability (figure 3.22), the evolution of the angular velocity is slower and follows more closely a pure viscous diffusion law except in the vicinity of the critical radius where the decay is also slightly enhanced.

3.8 Conclusion

We have studied numerically and theoretically the evolution of a Lamb-Oseen vortex in a stratified-rotating fluid under the complete Coriolis force on the f-plane. The problem is governed mainly by the Froude number F_h, the Reynolds number Re and the non-traditional Rossby number $\widetilde{Ro}$ based on the horizontal component of the background rotation.

Starting from a purely two-dimensional axisymmetric vortex, the DNS shows that a strong vertical velocity field with an azimuthal wavenumber $m = 1$ is generated at a particular radius when the Froude number is larger than unity. This radius increases with the Froude number. Simultaneously, the vertical vorticity develops a quasi-axisymmetric anomaly near the same radius. Later, this anomalous ring may become fully non-axisymmetric with an azimuthal wavenumber $m = 2$ when the Reynolds number is sufficiently large and the non-traditional Rossby number $\widetilde{Ro}$ not too large. At late time, the vorticity returns to a quasi-axisymmetric shape. Even if the vertical velocity is non-zero, all the fields remain independent of the vertical coordinate. In other words, the flow is 2D3C, i.e. two dimensional but with 3 velocity components.

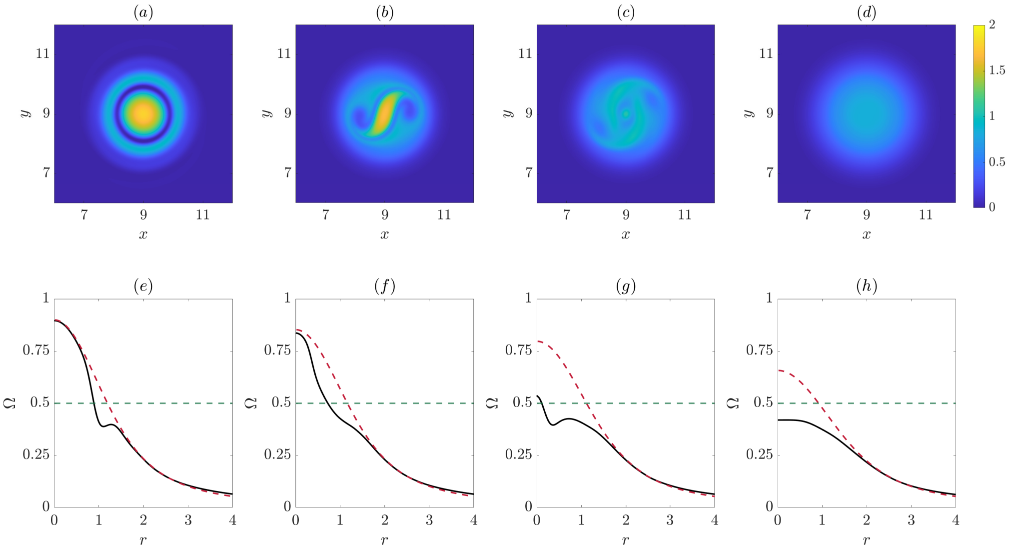

Fig. 3.21: Vertical vorticity (top) and angular velocity profile (bottom) obtained from DNS (black line) at (a, e) $t = 50$, (b, f) $t = 80$, (c, g) $t = 120$ and (d, h) $t = 250$ for $Re = 2000$, $F_h = 2$, $Ro = 23.1$, $\phi = 60°$ ($\widetilde{Ro} = 40$). The red dashed lines show the angular velocity profile if only viscous diffusion were active. The horizontal green dashed line represents the critical angular velocity value $1/F_h$.

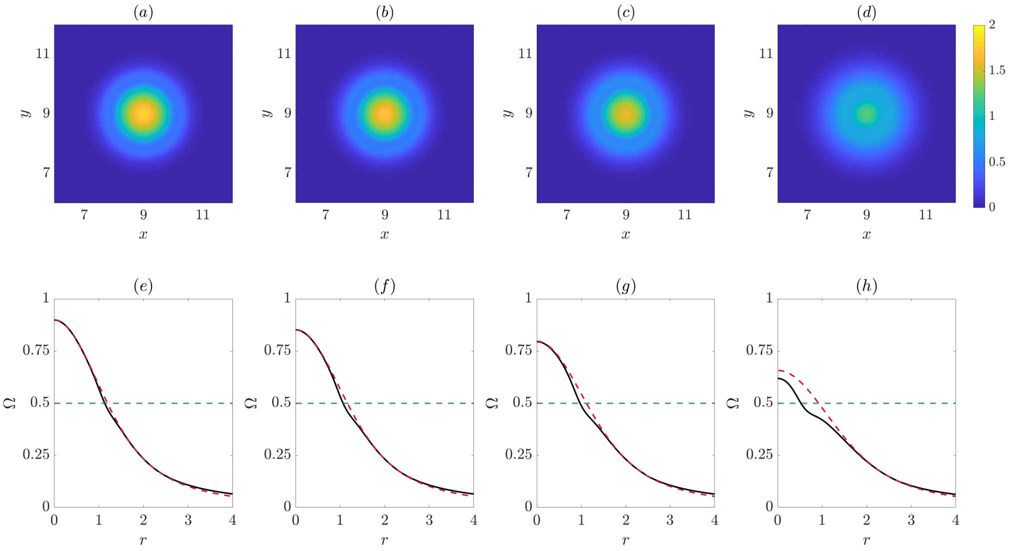

Fig. 3.22: Vertical vorticity (top) and angular velocity profile (bottom) obtained from DNS (black line) at (a, e) $t = 80$, (b, f) $t = 80$, (c, g) $t = 120$ and (d, h) $t = 250$ for $Re = 2000$, $F_h = 2$, $Ro = 23.1$, $\phi = 80°$ ($\widetilde{Ro} = 115.2$). The red dashed lines show the angular velocity profile if only viscous diffusion were active. The horizontal green dashed line represents the critical angular velocity value $1/F_h$.

For this reason, the dynamics is independent of the traditional Rossby number Ro based on the vertical component of the background rotation.

An asymptotic analysis for large non-traditional Rossby number $\widetilde{Ro}$ has allowed us to unravel this evolution. First, it shows that the non-traditional Coriolis force generates a vertical velocity and buoyancy fields at order $1/\widetilde{Ro}$ which are invariant along the vertical. When the Froude number F_h is larger than unity and in the absence of time dependence and viscous effects, these fields present a singularity at the radius where the angular velocity is equal to the Brunt–Väisälä frequency (i.e. the inverse of the Froude number in non-dimensional form). The asymptotic analyses show that this singularity is first regularized by the time dependence. This leads to a linear increase of the amplitude of the vertical velocity while the width of the critical layer shrinks at a rate inversely proportional to time. After a certain time, viscous effects saturate this evolution. The vertical velocity field is then steady with an amplitude proportional to $Re^{1/3}$ and a critical layer width scaling like $Re^{-1/3}$ as found by Boulanger *et al.* (2007) in the case of a tilted vortex in a stratified fluid. These asymptotic predictions are all in very good agreement with the DNS.

In turn, the non-traditional Coriolis force due to the vertical velocity modifies the vertical vorticity field at order $1/\widetilde{Ro}^2$. The dominant effect is the development of an axisymmetric ring of anomalous vorticity near the critical radius. This leads to the development of extrema in the vorticity profile. Again, the asymptotic predictions for the axisymmetric component of the vorticity are in good agreement with the DNS. Following Wang & Balmforth (2020, 2021), we have further carried out a non-linear asymptotic analysis that takes into account the effect of the anomaly of axisymmetric vorticity back on the evolution of the vertical velocity. The predictions of this non-linear analysis are in better agreement with the DNS than those of the linear analysis indicating that both viscous and nonlinear effects operate in the critical layer.

In order to understand the origin of the subsequent non-axisymmetric evolution of the vorticity field, we have first decomposed the vertical velocity and vorticity in the DNS by an azimuthal Fourier transform. This analysis shows that several azimuthal modes grow exponentially during the onset of non-axisymmetry: the odd modes $m = 3$, $m = 5$, etc for the vertical velocity and the even modes $m = 2$, $m = 4$, etc for the vertical vorticity. We have then introduced a highly truncated model which keeps only the $m = 1$ azimuthal wavenumber of the vertical velocity and the $m = 0$ and $m = 2$ wavenumbers of the vertical vorticity. Such truncated model exhibits also an onset of non-axisymmetry like in the DNS demonstrating that this behavior is not due to an unstable coupling between azimuthal modes. Furthermore, we have shown that if we freeze the profile of the axisymmetric component of the vertical vorticity at the time where the non-axisymmetry starts to appear and initializes the $m = 2$ mode by white noise, the latter mode grows exponentially at a rate comparable to the one observed in the DNS. In addition, the stability of an equivalent piecewise vortex model with four levels of vorticity has been investigated and have been found to give growth rates for $m = 2$ in agreement with those of the truncated model. Altogether, this proves that the onset of non-axisymmetry comes from a two-dimensional shear instability related to the presence of a minimum in the vorticity profile. Finally, using the asymptotic expression of the axisymmetric component of the vorticity at late time at leading orders, the necessary condition for the shear instability has been converted into an instability condition in terms of $(Re, \widetilde{Ro})$. This condition delimits well the quasi-axisymmetric/non-axisymmetric domains in the parameter space $(Re, \widetilde{Ro})$.

The overall effect of the instability is to accelerate the decay of the angular velocity compared to a pure viscous diffusion. The instability ceases when the angular velocity is everywhere lower than the Brunt–Väisälä frequency (i.e. the inverse of the Froude number in non-dimensional form).

In summary, we have seen that the dynamics of a vortex for large Reynolds number can be strongly affected by the non-traditional Coriolis force even if the non-traditional Rossby number $\widetilde{Ro}$ is large, i.e. even for a small value of the horizontal component of the background rotation. Since the typical Reynolds number of geophysical vortices is generally huge, this means that the non-traditional Coriolis force might have much more impact than expected by just considering its order of magnitude through the non-traditional Rossby number $\widetilde{Ro}$. It should be reminded however that another crucial condition is $F_h > 1$ that ensures the presence of a critical layer. Hence, such process might affect intense but not too large vortices in geophysical flows.

In the future, we will investigate the effect of three-dimensional perturbations on this phenomenon. Indeed, the vertical velocity is also responsible for an axial shear that might lead to another kind of shear instability if small three-dimensional perturbations are present as observed by Boulanger *et al.* (2007) for the case of a tilted vortex. It could be interesting also to study the configurations where the vortex is initially aligned with the background rotation vector or not columnar.

Appendix

A Approximation of the solution of (3.43) for large time

The solution (3.44) can be simplified for large time $T \gg 1$, i.e. $t \gg Re^{1/3}$. It is first convenient to derive ζ_{20} with respect to $\tilde{r}$.

$$\frac{\partial \zeta_{20}}{\partial \tilde{r}} = \frac{ReA}{2\gamma\pi} \int_0^{\left|\Omega_c'\right| T} \exp\left(\frac{-q^3}{3\gamma^3} + iq\tilde{r}\right)\left(1 - \exp\left(q^3/\left|\Omega_c'\right| - q^2 T\right)\right) \mathrm{d}q + c.c. \tag{3.72}$$

By using the change of variable $z = q/\gamma$ for the first part of the integrand and $x = q\sqrt{T}$ for the second part, (3.72) can be rewritten

$$\begin{aligned} \frac{\partial \zeta_{20}}{\partial \tilde{r}} =& \frac{ReA}{2\pi} \int_0^{\left|\Omega_c'\right| T/\gamma} \exp\left(\frac{-z^3}{3} + i\gamma z\tilde{r}\right) \mathrm{d}z \\ & - \frac{ReA}{2\gamma\pi\sqrt{T}} \int_0^{\left|\Omega_c'\right| T^{3/2}} \exp\left(\frac{-x^3}{3\gamma^3 T^{3/2}} + i\frac{x\tilde{r}}{\sqrt{T}} + \frac{x^3}{|\Omega_c'| T^{3/2}} - x^2\right) \mathrm{d}x + c.c. \quad . \end{aligned} \tag{3.73}$$

When $T \gg 1$, the first integral tends to the Scorer's function (Abramowitz & Stegun, 1972) whereas the terms proportional to $1/T^{3/2}$ can be neglected compared to the other terms in the second integral. This yields

$$\frac{\partial \zeta_{20}}{\partial \tilde{r}} \simeq \frac{ReA}{2}\mathrm{Hi}(i\gamma\tilde{r}) - \frac{ReA}{2\gamma\pi\sqrt{T}}\int_0^{\left|\Omega_c'\right|T^{3/2}} \exp\left(-x^2 + i\frac{x\tilde{r}}{\sqrt{T}}\right)\mathrm{d}x + c.c. \quad . \tag{3.74}$$

By introducing another change of variable

$$U = x - \frac{i\tilde{r}}{2\sqrt{T}}, \tag{3.75}$$

(3.74) becomes

$$\frac{\partial \zeta_{20}}{\partial \tilde{r}} \simeq \frac{ReA}{2}\mathrm{Hi}(i\gamma\tilde{r}) - \frac{ReA}{2\gamma\pi\sqrt{T}}\exp\left(\frac{-\tilde{r}^2}{4T}\right)\int_{-i\tilde{r}/(2\sqrt{T})}^{\left|\Omega_c'\right|T^{3/2}-i\tilde{r}/(2\sqrt{T})} \mathrm{e}^{-U^2}\mathrm{d}U + c.c. \quad . \tag{3.76}$$

The imaginary terms in the integral cancel with those of the complex conjugate giving

$$\frac{\partial \zeta_{20}}{\partial \tilde{r}} = \frac{ReA}{2}\left[\mathrm{Hi}(i\gamma\tilde{r}) + \mathrm{Hi}^*(i\gamma\tilde{r})\right] - \frac{ReA}{\gamma\pi\sqrt{T}}\exp\left(\frac{-\tilde{r}^2}{4T}\right)\int_0^{\left|\Omega_c'\right|T^{3/2}} \mathrm{e}^{-U^2}\mathrm{d}U. \tag{3.77}$$

The remaining integral can be approximated by $\sqrt{\pi}/2$ since $T \gg 1$, leading finally to

$$\frac{\partial \zeta_{20}}{\partial \tilde{r}} = \frac{ReA}{2}\left[\mathrm{Hi}(i\gamma\tilde{r}) + \mathrm{Hi}^*(i\gamma\tilde{r})\right] - \frac{ReA}{2\gamma\sqrt{\pi T}}\exp\left(\frac{-\tilde{r}^2}{4T}\right). \tag{3.78}$$

Integrating back in $\tilde{r}$ gives the approximation (3.46).

Chapter 4

Three-dimensional evolution of the vortex

Dynamics of a stratified vortex under the complete Coriolis force: three-dimensional evolution

Iman Toghraei[1], and Paul Billant[1]
[1]LadHyX, CNRS, École polytechnique, Institut Polytechnique de Paris, 91120 Palaiseau, France
(Ready for submission)

Abstract: The three-dimensional evolution of a Lamb-Oseen vortex is studied in a stratified rotating fluid under the complete Coriolis force. In a companion paper, it was shown that the non-traditional Coriolis force generates a vertical velocity field and a vertical vorticity anomaly at a critical radius when the Froude number is larger than unity. Below a critical non-traditional Rossby number $\widetilde{Ro}$ (based on the horizontal component of background rotation), a two-dimensional shear instability was next triggered by the vorticity anomaly. Here, we test the robustness of this pure two-dimensional evolution with respect to small three-dimensional perturbations. Direct numerical simulations (DNS) show that the two-dimensional shear instability then develops only in an intermediate range of non-traditional Rossby numbers. For lower $\widetilde{Ro}$, the instability is three-dimensional and resembles the one observed by Boulanger *et al.* (2008) on a stratified tilted vortex. Stability analyses of the flows in the DNS prior to the onset of the instability fully confirm the existence of these two competing instabilities. In addition, stability analyses of the local linear and non-linear theoretical flows at leading order in the vicinity of the critical layer demonstrate that the three-dimensional instability is due to the shear of the vertical velocity field. However, the growth rate of the three-dimensional instability obtained from such local stability analysis agrees quantitatively with the stability analyses of the DNS flows only if second order effects due to the traditional Coriolis force (related to the vertical component of background rotation) and the buoyancy force are taken into account. The latter effects tend to damp the three-dimensional instability. For this reason, the two-dimensional instability becomes dominant over the three-dimensional instability when the traditional Rossby number is decreased keeping the other parameters fixed.

4.1 Introduction

A common approximation in geophysical fluid dynamics is the traditional approximation that ignores the horizontal component of the planetary rotation when considering a local Cartesian frame at a given latitude. The Coriolis force then takes into account only the vertical component of the planetary rotation. However, as reviewed by Gerkema *et al.* (2008), several recent studies examining geophysical flows beyond the traditional approximation suggest that the complete Coriolis force, i.e. with a background rotation along both vertical and horizontal axes, plays a non-negligible role for flows where significant vertical motions or a weak stratification are present. These studies show that the non-traditional Coriolis force generates horizontal asymmetry for horizontally symmetrical flows (Semenova & Slezkin, 2003; Sheremet, 2004), modifies and enhances instabilities (Tort *et al.*, 2016; Zeitlin, 2018; Park *et al.*, 2021; Chew *et al.*, 2022), and changes wave dynamics (Gerkema *et al.*, 2008; Zhang & Yang, 2021).

Toghraei & Billant (2022) have recently studied the evolution of an initially two-dimensional vortex in a stratified fluid under the complete Coriolis force by means of direct numerical simulations (DNS). Due to the horizontal background rotation, a critical layer appears at the radius where the angular velocity of the vortex is equal to the Brunt–Väisälä frequency (i.e. the inverse of the Froude number in non-dimensional form). Such radius exists only if the Froude number is larger than unity. The critical layer induces a vertical velocity field and a vertical vorticity anomaly that first grow linearly with time while being more and more concentrated around the critical radius until they finally saturate. In parallel to the DNS, Toghraei & Billant (2022) have performed a linear asymptotic analysis for large non-traditional Rossby numbers (based on the horizontal component of the background rotation). It shows that the singularity of the critical layer is smoothed by both viscosity and unsteadiness, like for the baroclinic critical layer in a horizontal shear flow studied by Wang & Balmforth (2020, 2021). A non-linear asymptotic analysis has been also conducted following Wang & Balmforth (2020, 2021) to obtain the velocity and vorticity fields in the critical layer when their amplitude is large. The linear and non-linear asymptotic solutions for the vertical velocity and the vertical vorticity anomaly have been found to be in excellent agreement with the DNS. Finally, it has been shown that the critical layer generates an inflection point in the vertical vorticity profile which triggers a two-dimensional shear instability for sufficiently high Reynolds numbers and low non-traditional Rossby numbers. A theoretical criterion predicting the occurrence of the two-dimensional instability has been derived from the inflection point condition.

The vortex dynamics described by Toghraei & Billant (2022) is purely two-dimensional but with three velocity components. It can be indeed shown from the governing equations that if the initial conditions are two-dimensional, all the velocity fields remain two-dimensional throughout their evolutions. In the present paper, we will test the robustness of such evolution with respect to infinitesimal three-dimensional perturbations added at the beginning of the DNS. We will see that the dynamics remains two-dimensional as in Toghraei & Billant (2022) for some parameters, while for other parameters, a three-dimensional instability develops. This newly observed instability resembles the three-dimensional instability reported by Boulanger *et al.* (2007, 2008) in their experimental study of an inclined vortex in a stratified fluid. To some extent, such configuration is similar to the present one, since in both cases, there is a tilt with respect to the gravity forces. A critical layer develops in the tilted vortex at the radius where the angular velocity of the vortex is equal to the Brunt–Väisälä frequency and induces an intense vertical velocity field. For sufficiently large tilt angle and Reynolds number, a three-dimensional instability leads to the formation of rows of vortices with a zig-zag structure. In order to determine the origin of the instability, Boulanger *et al.* (2008) have performed a local stability analysis of the critical layer using the vertical velocity field derived theoretically by means of a linear viscous analysis of the critical layer. Considering only the leading-order terms when the vertical velocity is large, they have shown that the local stability problem reduces to a Rayleigh equation around the vertical velocity field as for the stability of inviscid parallel shear flows. The growth rate predictions obtained by neglecting the azimuthal dependence of the vertical velocity field, are in good agreement with the experimentally measured growth rates. Hence, Boulanger *et al.* (2008) have concluded that the three-dimensional instability comes from a shear instability of the vertical velocity field generated in the critical layer. Here, we will follow their local approach in order to determine if the characteristics of the three-dimensional and two-dimensional instabilities can be predicted.

The paper is organized as follows. The initial conditions, governing equations and numerical methods are first presented in §4.2. §4.3 describes qualitatively the two distinct instabilities observed in DNS when the non-traditional Rossby number is varied while the other parameters are kept constant. Linear stability analyses of the flows in the DNS prior to the onset of the instabilities are carried out in §4.4. This is completed in §4.5 by linear stability analyses of the local theoretical flows in the critical layer. The results of both types of stability analysis are then compared in §4.6. Finally, §4.7 studies the effects of the Reynolds number and of the traditional Rossby number. Conclusions are drawn in §4.8.

4.2 Formulation of the problem

4.2.1 Initial conditions

A single vertical Lamb-Oseen vortex with vorticity

$$\boldsymbol{\omega}(\boldsymbol{x}, t=0) = \zeta_0 \boldsymbol{e_z} = \frac{\Gamma}{\pi a_0^2} e^{-r^2/a_0^2} \boldsymbol{e_z}, \tag{4.1}$$

where Γ is the circulation and a_0 the radius, is considered as initial conditions accompanied by small random perturbations. In the following, we will use either Cartesian (x, y, z) or cylindrical (r, θ, z) coordinates. The associated unit vectors are denoted $(\boldsymbol{e_x}, \boldsymbol{e_y}, \boldsymbol{e_z})$ and $(\boldsymbol{e_r}, \boldsymbol{e_\theta}, \boldsymbol{e_z})$, respectively. The geometry of the flow is sketched in figure 4.1. The vortex is located at the center of a box with dimensions of $l_x \times l_y \times l_z$. The background rotation vector $\boldsymbol{\Omega_b}$ is decomposed into two vertical and horizontal components: $2\boldsymbol{\Omega_b} = \tilde{f}\boldsymbol{e_y} + f\boldsymbol{e_z}$ where $f = 2\Omega_b \sin(\phi)$ and $\tilde{f} = 2\Omega_b \cos(\phi)$, where ϕ is the angle between the background rotation vector and the unit vector in the y direction, $\boldsymbol{e_y}$. The fluid is stably stratified with a constant Brunt–Väisälä frequency $N = \sqrt{-(g/\rho_0)\partial\bar{\rho}/\partial z}$, where g is the gravity, ρ_0 a constant reference density and $\bar{\rho}(z)$ the mean density profile.

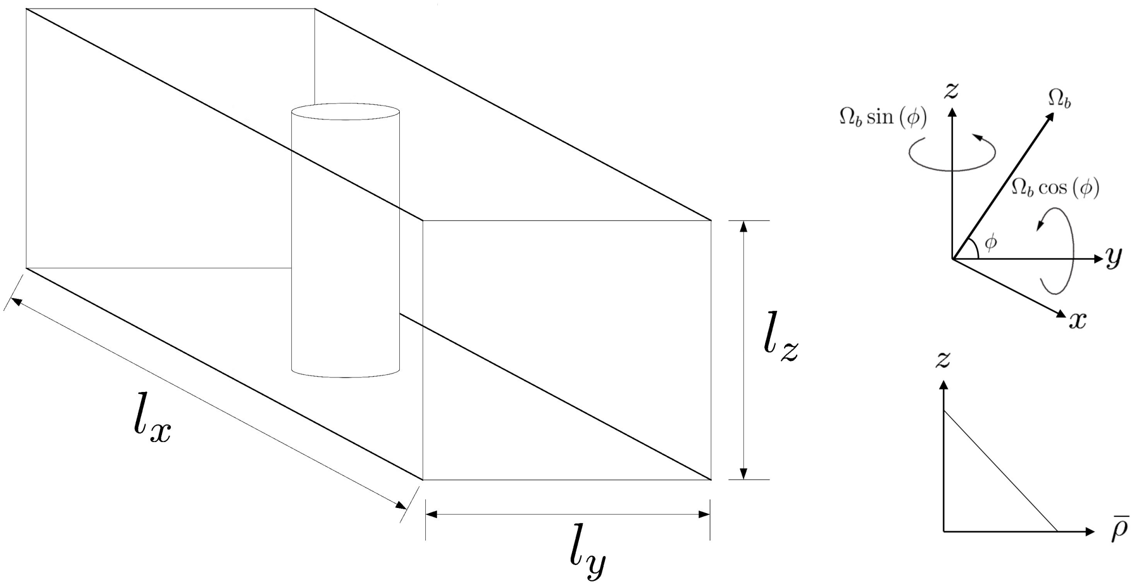

Fig. 4.1: Sketch of the initial vortex in a stratified rotating fluid with a background rotation Ω_b inclined with an angle ϕ.

4.2.2 Governing equations

The governing equations are non-dimensionalized by using $2\pi a_0^2/\Gamma$ and a_0 as time and length units:

$$\boldsymbol{\nabla} \boldsymbol{.} \boldsymbol{u} = 0, \tag{4.2}$$

$$\frac{\partial \boldsymbol{u}}{\partial t} + (\boldsymbol{u} \boldsymbol{.} \boldsymbol{\nabla})\, \boldsymbol{u} = -\boldsymbol{\nabla} p + b\boldsymbol{e_z} - 2\left(\frac{1}{Ro}\boldsymbol{e_z} + \frac{1}{\widetilde{Ro}}\boldsymbol{e_y}\right) \times \boldsymbol{u} + \frac{1}{Re}\boldsymbol{\nabla}^2 \boldsymbol{u}, \tag{4.3}$$

$$\frac{\partial b}{\partial t} + \boldsymbol{u} \boldsymbol{.} \boldsymbol{\nabla} b + \frac{1}{F_h^2} u_z = \frac{1}{ReSc} \nabla^2 b, \tag{4.4}$$

where $\boldsymbol{u}$, b and p are the non-dimensional velocity, buoyancy and pressure, respectively. The problem is controlled by five non-dimensional numbers: the Reynolds, Froude, Rossby and Schmidt numbers defined as follows

$$Re = \frac{\Gamma}{2\pi\nu}, \qquad F_h = \frac{\Gamma}{2\pi a_0^2 N}, \qquad Ro = \frac{\Gamma}{\pi a_0^2 f}, \qquad \widetilde{Ro} = \frac{\Gamma}{\pi a_0^2 \tilde{f}}, \qquad Sc = \frac{\nu}{\kappa}. \tag{4.5}$$

where ν is the viscosity and κ the diffusivity of the stratifying agent. The two Rossby numbers– traditional Rossby number Ro and non-traditional Rossby number $\widetilde{Ro}$– measure the two components of the rotation vector. The Schmidt number will be always set to unity. In the following, all the results will be presented in a non-dimensional form.

4.2.3 Numerical methods

A pseudo-spectral method with periodic boundary conditions and fourth-order Runge–Kutta time integration is used as in Toghraei & Billant (2022). The horizontal sizes of the computational domain have been set to $l_x = l_y = 18$, to minimize the effect of the periodic boundary conditions (see Toghraei & Billant (2022) for details). The vertical size has been set to $l_z = 8$ in order to adequately accommodate several vertical wavelengths of the dominant three-dimensional instability. For all the DNS, the Reynolds number will be kept constant and set to $Re = 2000$. As shown by Toghraei & Billant (2022), the horizontal resolution required for this value of Re is $n_x = n_y = 512$. Accordingly, the vertical resolution has been set to $n_z = 256$. The time step is $\delta t = 0.01$. A number of DNS have been conducted to test the accuracy of the configurations. In particular, the tests have shown that the velocity differs by less than 0.2% when the vertical resolution is increased from $n_z = 256$ to $n_z = 512$. Random three-dimensional perturbations are added initially to the vortex. They consist in a divergence-free white noise with amplitude 0.001.

4.3 Typical examples of the vortex dynamic

The objective of this section is to present qualitatively the different vortex evolutions observed in the DNS. Figure 4.2 shows the evolution of the vertical velocity at three different times for the set of parameters $Re = 2000$, $F_h = 4$, $Ro = 23.1$, $\widetilde{Ro} = 40$. In this figure, three planes are displayed: a horizontal cross-section at the middle plane $z = l_z/2$ (first row) and two vertical cross-sections at the planes $y = l_y/2$ (second row) and $x = l_x/2$ (third row) going through the initial vortex center. Figure 4.3 shows the corresponding evolution of the vertical vorticity. Since the vertical vorticity remains predominantly quasi-asymmetric, only two planes are displayed: a horizontal cross-section in the plane $z = l_z/2$ (first row) and a vertical cross-section at the plane $y = l_y/2$ (second row).

As previously reported by Toghraei & Billant (2022), the presence of the non-traditional Coriolis force generates a vertical velocity field with azimuthal wavenumber $m = 1$ (figure 4.2(a, d, g)). This vertical velocity field concentrates at the critical radius r_c where the non-dimensional angular velocity of the vortex Ω equals the inverse of the Froude number $\Omega(r_c) = 1/F_h$. A ring of vertical vorticity anomaly also develops at r_c (figure 4.3(a, d)). The vortex appears still two-dimensional at $t = 40$. However, later on (figures 4.2(b, e, h) and 4.3(b, e)), three-dimensional variations become visible in both the vertical velocity field and the vertical vorticity anomaly. At $t = 56$ (figures 4.2(c, f, i) and 4.3(c, f)), the amplitude of the deformations along the vertical has grown and the vertical cross-section of the vertical vorticity (figure 4.3(f)) exhibits a structure similar to the one observed by Boulanger *et al.* (2007, 2008) on a stratified tilted vortex. Although there are some irregularities due to the randomness of the initial three-dimensional perturbations, we can distinguish five wavelengths along the vertical, i.e. a dominant wavenumber $k \approx 4$. We can also see that the deformations are in opposite phases on the two sides of the vortex (figure 4.3 (f)). In the horizontal cross-sections (figures 4.2(c) and 4.3(c)), non-axisymmetric deformations can be also seen but they are irregular and weak compared to those of the two-dimensional instability reported by Toghraei & Billant (2022).

A similar three-dimensional instability has been observed when the non-traditional Rossby number is increased to $\widetilde{Ro} = 60$ or $\widetilde{Ro} = 80$ while keeping the other parameters fixed (see figures 4.24-4.27 in appendix A). Note that the corresponding traditional Rossby number Ro varies also slightly from $Ro = 23.1$ to $Ro = 20.7$ when $\widetilde{Ro}$ is increased since it is ϕ that is varied whereas $\Omega_b = 0.1$ is kept constant. However, when the non-traditional Rossby number is further increased to $\widetilde{Ro} = 115$ (figures 4.4 and 4.5), three-dimensional deformations are no longer visible while two-dimensional non-axisymmetric disturbances with an azimuthal mode $m = 2$ can be seen in the horizontal cross-sections at late times $t = 167$ and $t = 175$ (figures 4.4(b, c) and 4.5(b, c)) as observed by Toghraei & Billant (2022).

The nature of the dominant instability, therefore, depends on the parameters. The vertical velocity and vorticity fields observed before the instability have a similar shape for $\widetilde{Ro} = 40$ (figures 4.2(a, d, g) and 4.3(a, d)) and $\widetilde{Ro} = 115$ (figures 4.4(a, d, g) and 4.5(a, d)). However, we can notice that the maximum vertical velocity is larger by 50% for $\widetilde{Ro} = 40$ than for $\widetilde{Ro} = 115$ and the vertical vorticity anomaly is also much stronger for $\widetilde{Ro} = 40$ than for $\widetilde{Ro} = 115$.

4.4 Linear stability analysis of the flows in the DNS

In order to further describe the competition between the two-dimensional and three-dimensional instabilities, we have carried out linear stability analyses of the flows in the DNS at different times before the onset of the instability.

4.4.1 Methods

To do so, a two-dimensional simulation was first run for each set of parameters. Then, the velocity and buoyancy fields $\boldsymbol{U} = (U_x, U_y, U_z)$ and B have been frozen at a given time $t = t_b$. They are next perturbed by infinitesimal perturbations

$$[\boldsymbol{u}, b](\boldsymbol{x}, t) = [\boldsymbol{U}, B](x, y, t_b) + [\boldsymbol{u}', b'](\boldsymbol{x}, t), \tag{4.6}$$

denoted with a prime. The perturbations are governed by the equations (4.2-4.4) linearized around $(\boldsymbol{U}, B)$:

$$\boldsymbol{\nabla.u}' = 0, \tag{4.7}$$

$$\frac{\partial \boldsymbol{u}'}{\partial t} + (\boldsymbol{U.\nabla})\,\boldsymbol{u}' + \left(\boldsymbol{u}'\boldsymbol{.\nabla}\right)\boldsymbol{U} = -\boldsymbol{\nabla} p' + b'\boldsymbol{e_z} - 2\left(\frac{1}{Ro}\boldsymbol{e_z} + \frac{1}{\widetilde{Ro}}\boldsymbol{e_y}\right)\times\boldsymbol{u}' + \frac{1}{Re}\boldsymbol{\nabla}^2\boldsymbol{u}', \tag{4.8}$$

$$\frac{\partial b'}{\partial t} + \boldsymbol{U.\nabla} b' + \boldsymbol{u}'\boldsymbol{.\nabla} B + \frac{1}{F_h^2} u_z' = \frac{1}{ReSc}\nabla^2 b', \tag{4.9}$$

Such "freezing" method is expected to give reliable results if the time evolution of the flow $(\boldsymbol{U}, B)$ is slow compared to the growth rate of the perturbations.

The equations (4.7-4.9) are integrated with $[\boldsymbol{u}', b']$ initialized by white noise using the same numerical code and the same resolution and domain size in the horizontal directions as for the DNS. Since the base flow $(\boldsymbol{U}, B)$ is uniform along the vertical and

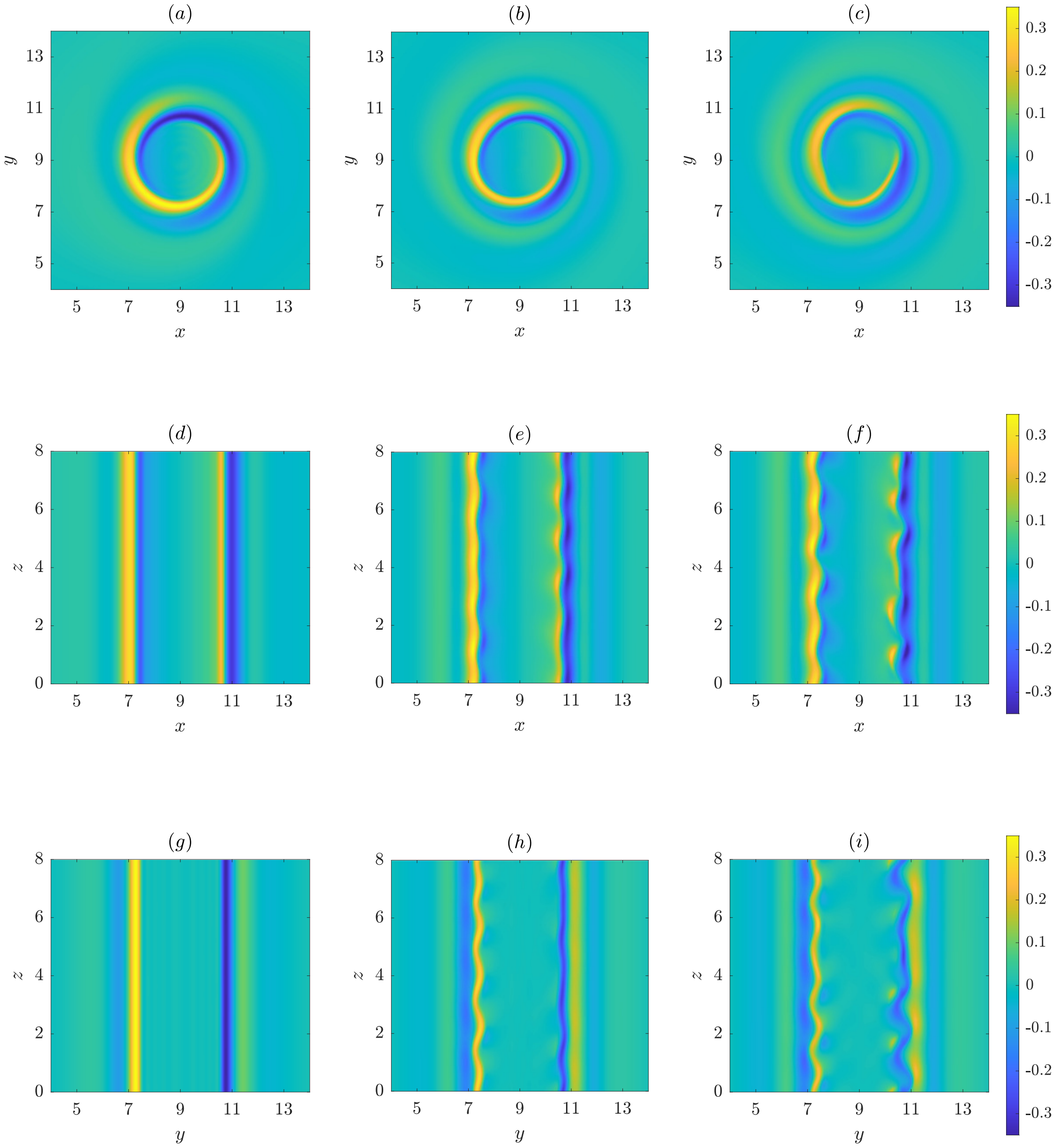

Fig. 4.2: Vertical velocity field in a horizontal cross-section at $z = l_z/2$ (first row) and two vertical cross sections at $y = l_y/2$ (second row) and $x = l_x/2$ (third row) at three different times: (a, d, g) $t = 40$, (b, e, h) $t = 53$, (c, f, i) $t = 56$ for $Re = 2000$, $F_h = 4$, $Ro = 23.1$ and $\widetilde{Ro} = 40$.

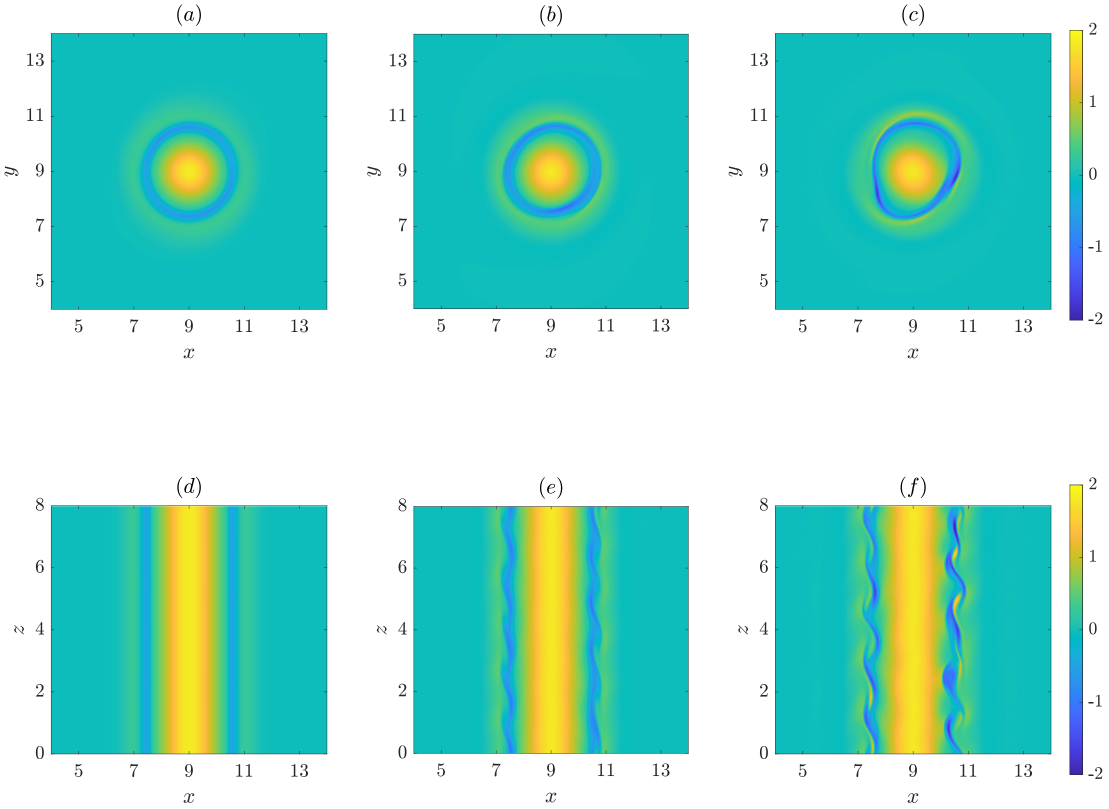

Fig. 4.3: Vertical vorticity field in a horizontal cross-section at $z = l_z/2$ (first row) and a vertical cross sections at $y = l_y/2$ (second row) at three different times: (a, d) $t = 40$, (b, e) $t = 53$, (c, f) $t = 56$ for $Re = 2000$, $F_h = 4$, $Ro = 23.1$ and $\widetilde{Ro} = 40$.

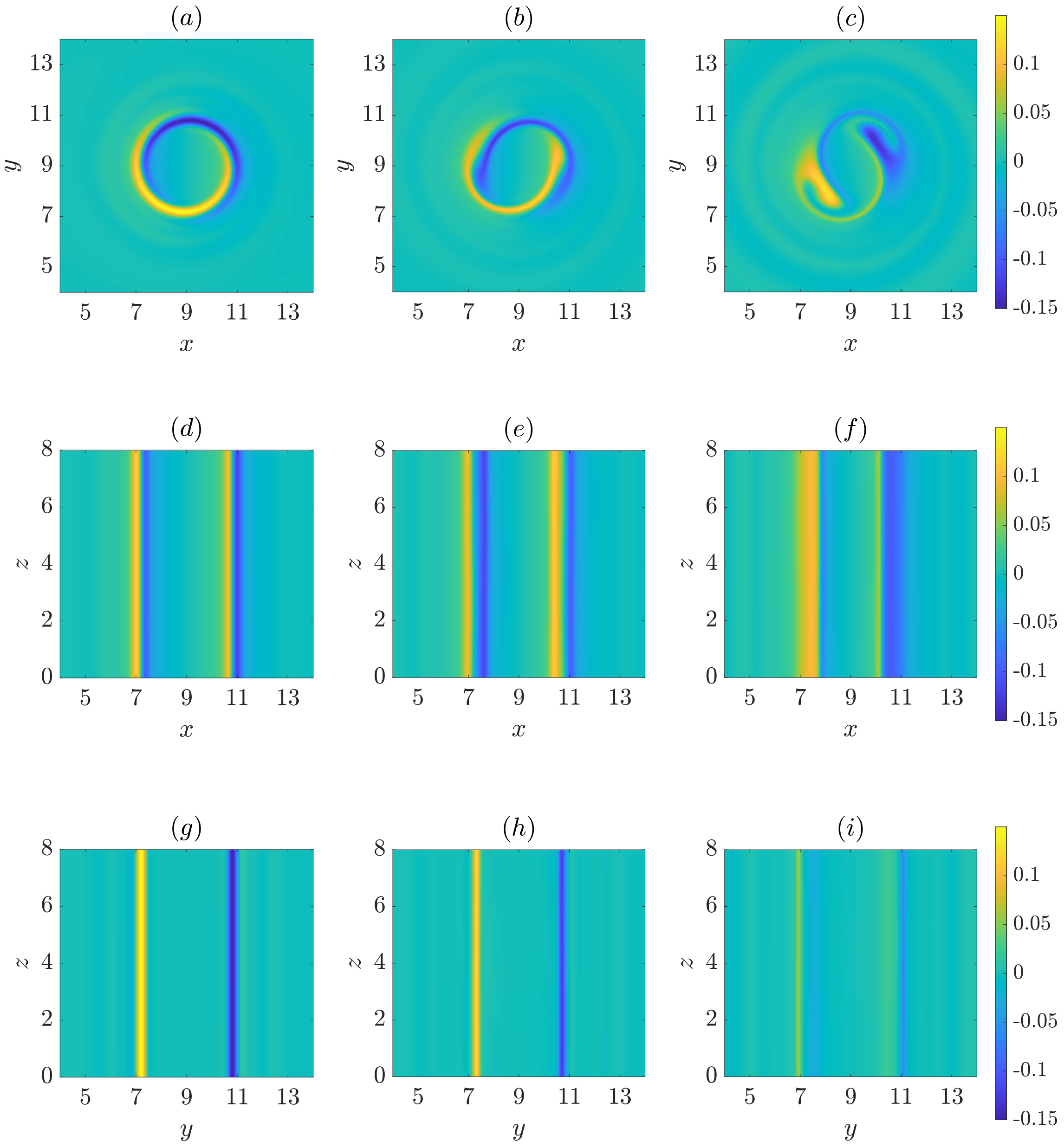

Fig. 4.4: Same as figure 4.2 but for $\widetilde{Ro} = 115$ and $Ro = 20.3$: (a, d, g) $t = 100$, (b, e, h) $t = 152$, (c, f, i) $t = 167$.

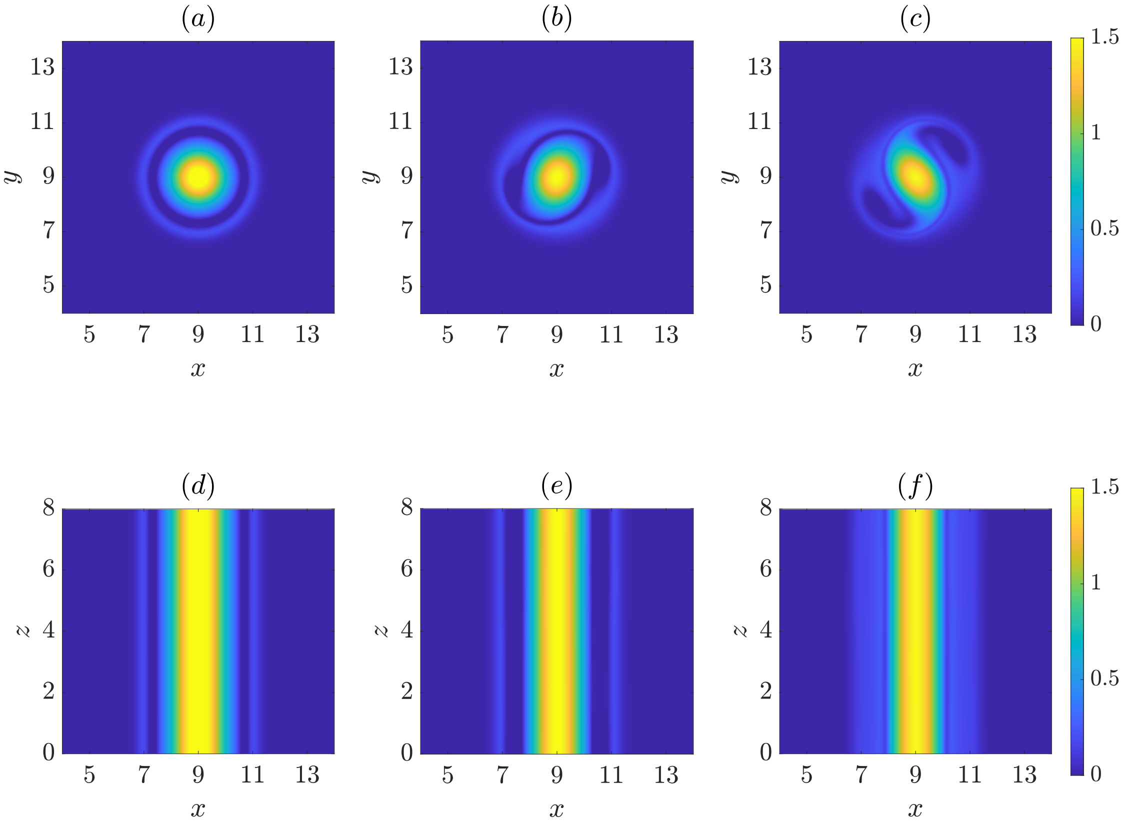

Fig. 4.5: Same as figure 4.3 but for $\widetilde{Ro} = 115$ and $Ro = 20.3$: (a, d) $t = 100$, (b, e) $t = 152$, (c, f) $t = 167$.

the equations (4.7-4.9) are linear, the amplitude $[\hat{\boldsymbol{u}}_{\boldsymbol{k}}, \hat{b}_k]$ of each vertical wavenumber of the perturbation:

$$[\boldsymbol{u}', b'] = \sum_{k=-k_{max}}^{k_{max}} [\hat{\boldsymbol{u}}_{\boldsymbol{k}}, \hat{b}_k](x, y, t)\mathrm{e}^{\mathrm{i}kz} \tag{4.10}$$

evolve independently of the others. Hence, by integrating (4.7-4.9) for a sufficiently long time, the perturbations $[\hat{\boldsymbol{u}}_{\boldsymbol{k}}, \hat{b}_k]$ for each vertical wavenumber will be dominated by the most unstable mode. The vertical size and resolution have been set to $l_z = 32$ and $n_z = 64$ in order to cover the wavenumber band $-2\pi \leq k \leq 2\pi$ with the resolution $\Delta k = \pi/16$.

In practice, the growth rate for each vertical wavenumber $\sigma_r(k)$ is retrieved from the total kinetic energy $E_k(t) = \int\int 1/2\left(\hat{u}_x^2 + \hat{u}_y^2 + \hat{u}_z^2\right) \mathrm{d}x\mathrm{d}y$ by means of the formula

$$\sigma_r(k) = \frac{1}{2(t_f - t_i)} \log\left(\frac{E_k(t_f)}{E_k(t_i)}\right), \tag{4.11}$$

where the two times t_i and t_f are chosen to be large and sufficiently separated in order to eliminate the oscillations of E_k when the instability is oscillating (Typically, $t_i = 140$ and $t_f = 190$). The pulsation $\sigma_i(k)$ of the instability can be also retrieved by searching the successive times t_n for which the relative kinetic energy $E_k(t)/(E_k(t_i)\mathrm{e}^{2\sigma_r(t=t_i)})$ is maximum. An estimation of the pulsation is then given by

$$\sigma_i(k) = \sum_{n=1}^{n_{max}-1} \frac{1}{(n_{max} - 1)} \frac{2\pi}{2(t_{n+1} - t_n)}, \tag{4.12}$$

where n_{max} is the number of maxima detected. In the following, only positive wavenumber k will be presented since negative ones are identical owing to the symmetry $z \to -z$.

4.4.2 Results

Figure 4.6 shows the growth rate as a function of the vertical wavenumber k for the four different values of $\widetilde{Ro}$ investigated in §4.3 for $Re = 2000$ and $F_h = 4$. For each case, we have computed the stability of the flows at four different times t_b prior to the time at which the instabilities become visible in the DNS. Globally, the growth rate levels increase with t_b and decrease with $\widetilde{Ro}$. For $\widetilde{Ro} = 40$ (figure 4.6(a)), all the wavenumbers are strongly unstable but there is a growth rate peak at $k \approx 4 - 5$ in agreement with the dominant wavenumber $k \approx 4$ observed in the DNS (figures 4.2 and 4.3). Figure 4.7(a) shows the pulsation σ_i corresponding to this peak (circle symbols) as a function of t_b. It is nearly constant $\sigma_i \approx 0.2$ when $t_b \geq 40$ and clearly differs from the pulsation of the two-dimensional instability (i.e. $k = 0$) which is also plotted by square symbols. The vertical velocity of the eigenmodes corresponding to the dominant three-dimensional instability and to the two-dimensional instability have also a different structure (figure 4.8) even if they are both concentrated around the critical radius. The two-dimensional eigenmode (figure 4.8(a)) exhibits a well-defined azimuthal wavenumber $m = 3$ which rotates with little change of shape. In contrast, the thee-dimensional eigenmode (figure 4.8(b)) presents an irregular azimuthal dependence which is modulated over the oscillation period of the instability.

As the non-traditional Rossby number is increased to $\widetilde{Ro} = 60$ (figure 4.6(b)) and $\widetilde{Ro} = 80$ (figure 4.6(c)), a peak continues to be observed around $k \approx 4-5$ but it is less pronounced relative to the growth rate at $k = 0$. In other words, the three-dimensional instability is still dominant for these values of $\widetilde{Ro}$ as observed in the DNS but its strength weakens comparatively to the two-dimensional instability. The pulsation corresponding to the growth rate peak is still around $\sigma_i \approx 0.2$ (figure 4.7(b, c)). However, the pulsation of the two-dimensional instability switches from $\sigma_i \approx 0.5$ at early times to $\sigma_i \approx 0.8$ at late times.

For $\widetilde{Ro} = 115$ (figure 4.6(d)), the growth rate is then maximum at $k = 0$ in agreement with the observation of a two-dimensional instability in the DNS (figures 4.4 and 4.5). A local peak around $k \approx 4-5$ is however still observed when $t_b \leq 80$ whereas it is less apparent for $t_b \geq 100$. The present linear stability analysis, therefore, confirms that there is a cross-over of the dominant instability from three-dimensional to two-dimensional as $\widetilde{Ro}$ increases. As seen in figure 4.7(d), the pulsations of the three-dimensional and two-dimensional instabilities are now $\sigma_i \approx 0.2$ and $\sigma_i \approx 0.5$, respectively, independently of t_b. Interestingly, figure 4.9(a) shows that the eigenmode of the two-dimensional instability exhibits now a $m = 2$ azimuthal structure, as observed in the DNS (figures 4.4 and 4.5), instead of $m = 3$ for $\widetilde{Ro} = 40$ (figure 4.8(a)). This change of the dominant azimuthal wavenumber of the two-dimensional instability explains why the pulsation switches from $\sigma_i \approx 0.8$ for $\widetilde{Ro} = 40$ to $\sigma_i \approx 2/3 \times 0.8 \approx 0.5$ for $\widetilde{Ro} = 115$. The three-dimensional eigenmode for $\widetilde{Ro} = 115$ (figure 4.9(b)) looks somewhat different from the one for $\widetilde{Ro} = 40$ (figure 4.8(b)) because they do not correspond to the same phase of the oscillation cycle.

Although the stability analysis has been performed by freezing a time-evolving flow $[\boldsymbol{U}, B]$, we can notice in figure 4.6 that the growth rate curves for the two last times t_b (red and blue lines) are very close for each plot. This indirectly suggests that the flow $[\boldsymbol{U}, B]$ has little evolved between these two times, legitimating the present analysis. The slow evolution of the base flow $[\boldsymbol{U}, B]$ when the instability develops will be confirmed in the next section.

4.5 Local stability analysis of the theoretical solutions in the critical layer

In order to further shed light on the competition between the three-dimensional and two-dimensional instabilities, we will now turn to a stability analysis of the local solutions in the critical layer that have been derived analytically for large Reynolds numbers and small non-traditional Rossby numbers in Toghraei & Billant (2022).

We first briefly recall the asymptotic analyses and the resulting solutions. Then, the stability of these solutions will be investigated.

4.5.1 Local base flow in the critical layer

Toghraei & Billant (2022) have solved (4.2-4.4) by assuming $\varepsilon = 2/\widetilde{Ro} \ll 1$ and $Re \gg 1$ and by considering the vicinity of the critical radius r_c by means of the variable

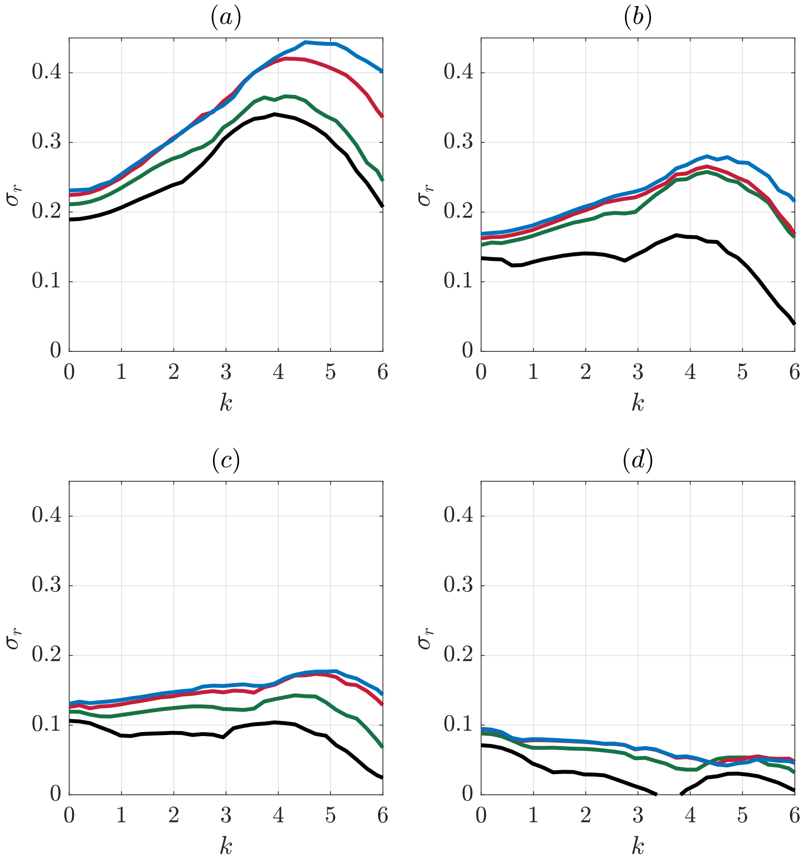

Fig. 4.6: Growth rate σ_r obtained from the stability analysis of the DNS flow as a function of the vertical wavenumber k for Re = 2000, $F_h = 4$, $\Omega_b = 0.1$ ($Ro \approx 20$) and (a) $\widetilde{Ro} = 40$, (b) $\widetilde{Ro} = 60$, (c) $\widetilde{Ro} = 80$ and (d) $\widetilde{Ro} = 115$. The colored lines corresponds to different times t_b:
(a) $t_b = 35$ (black line), $t_b = 40$ (green line), $t_b = 45$ (red line), $t_b = 50$ (blue line), (b) $t_b = 40$ (black line), $t_b = 50$ (green line), $t_b = 55$ (red line), $t_b = 60$ (blue line), (c) $t_b = 45$ (black line), $t_b = 55$ (green line), $t_b = 65$ (red line), $t_b = 75$ (blue line), (d) $t_b = 50$ (black line), $t_b = 70$ (green line), $t_b = 90$ (red line), $t_b = 100$ (blue line).

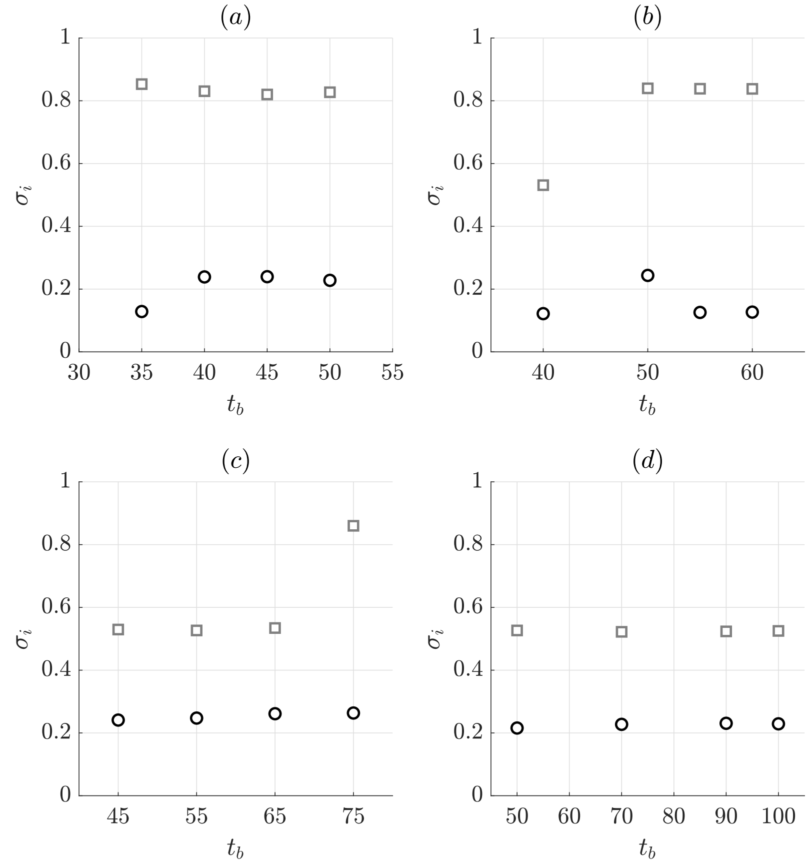

Fig. 4.7: Pulsation σ_i obtained from the stability analysis of the DNS flow for $k = 0$ (squares) and at the most amplified wavenumber in the range $k > 4$ (circles) as a function of the time t_b for Re $= 2000$, $F_h = 4$, $\Omega_b = 0.1$ ($Ro \approx 20$) and (a) $\widetilde{Ro} = 40$, (b) $\widetilde{Ro} = 60$, (c) $\widetilde{Ro} = 80$ and (d) $\widetilde{Ro} = 115$.

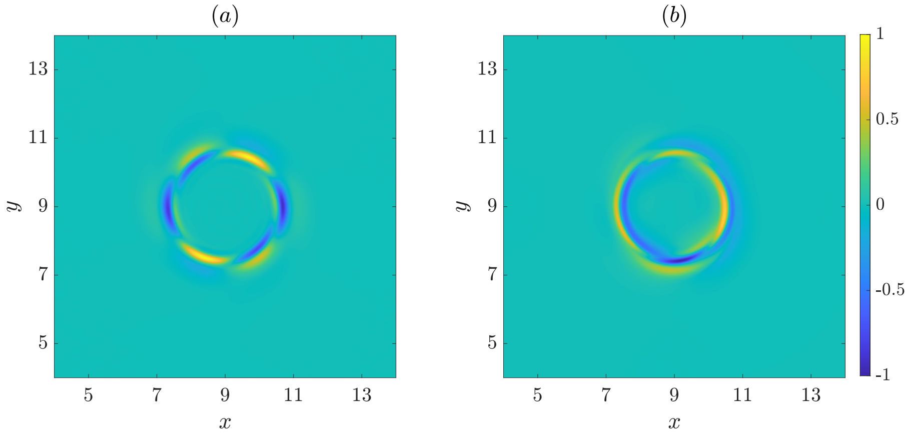

Fig. 4.8: Vertical velocity field of the eigenmode for (a) $k = 0$ and (b) $k = 4.5$ for $\widetilde{Ro} = 40$ and $Re = 2000$, $F_h = 4$, $Ro = 23.1$ at $t_b = 50$.

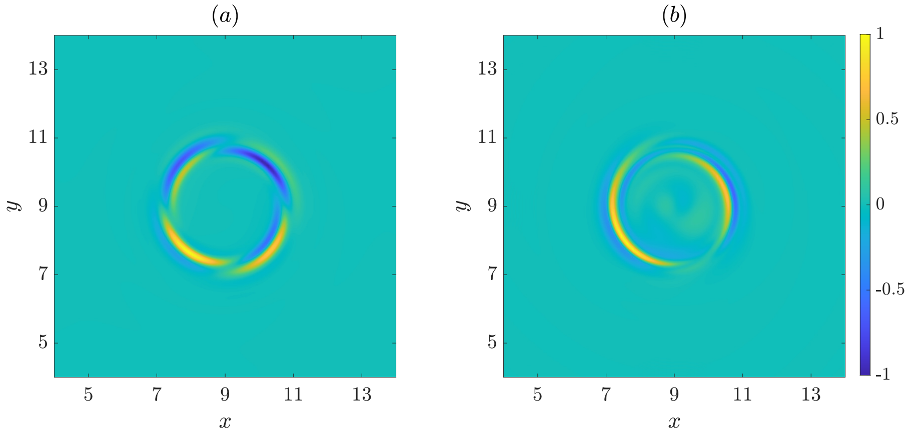

Fig. 4.9: Same as figure 4.8 but for (a) $k = 0$ and (b) $k = 5.3$ for $\widetilde{Ro} = 115$ and $Ro = 20.3$ at $t_b = 100$.

$\tilde{r} = Re^{1/3}(r - r_c)$. A slow time $T = Re^{-1/3}t$ has been also introduced. Both linear and non-linear analyses have been carried out following Boulanger *et al.* (2007) and Wang & Balmforth (2020, 2021). The latter assumes the distinguished scaling $Re = \widetilde{Re}/\varepsilon^2$ where $\widetilde{Re}$ is of order unity. The solutions for the vertical velocity, buoyancy, angular velocity and vertical vorticity then read at leading order in ε:

$$U_z = \varepsilon^{1/3}\widetilde{Re}^{1/3}\tilde{U}_z + ..., \tag{4.13a}$$

$$B = \varepsilon^{1/3}\widetilde{Re}^{1/3}\tilde{B} + ..., \tag{4.13b}$$

$$\Omega = \Omega_0 + \varepsilon^{2/3}\widetilde{Re}^{2/3}\Omega_1 + ..., \tag{4.13c}$$

$$\zeta = \zeta_0 + \widetilde{Re}\zeta_1 + ..., \tag{4.13d}$$

where $\tilde{U}_z = \tilde{U}_{z1}\mathrm{e}^{\mathrm{i}\theta} + c.c.$ and $\tilde{B} = \tilde{B}_1\mathrm{e}^{\mathrm{i}\theta} + c.c.$. At the leading order, Ω_0 and ζ_0, are the non-dimensional angular velocity and vertical vorticity corresponding to (4.1). In the vicinity of r_c, they can be expanded as

$$\Omega_0 = \Omega_c + \tilde{r}\Omega_c'\varepsilon^{2/3}\widetilde{Re}^{-1/3} + ..., \tag{4.14a}$$

$$\zeta_0 = \zeta_c + \tilde{r}\zeta_c'\varepsilon^{2/3}\widetilde{Re}^{-1/3} + ..., \tag{4.14b}$$

where the subscript c denotes the value at $r = r_c$. The vertical velocity $\tilde{U}_{z1}$ and angular velocity correction Ω_1 have been found to be governed by the following coupled equations:

$$\frac{\partial \tilde{U}_{z1}}{\partial T} + \mathrm{i}\Omega_c'\tilde{r}\tilde{U}_{z1} + \mathrm{i}\widetilde{Re}\Omega_1\tilde{U}_{z1} = \frac{\mathrm{i}}{4}r_c\Omega_c + \frac{1}{2}\left(1 + \frac{1}{Sc}\right)\frac{\partial^2\tilde{U}_{z1}}{\partial\tilde{r}^2}, \tag{4.15a}$$

$$\frac{\partial\Omega_1}{\partial T} = -\frac{\mathrm{i}}{2r_c}\left(\tilde{U}_{z1}^* - \tilde{U}_{z1}\right) + \frac{\partial^2\Omega_1}{\partial\tilde{r}^2}. \tag{4.15b}$$

The equation (4.15a) describes the evolution of the vertical velocity $\tilde{U}_{z1}$ near r_c due to viscous and diffusive effects (last term) and the effect of the angular velocity correction Ω_1 (last term of the left-hand side). The viscous effects and the time derivative smooth the solution $\tilde{U}_{z1}$, which without these terms would be $\tilde{U}_{z1} = r_c\Omega_c/(4\Omega_c'\tilde{r})$ and would be therefore singular at r_c. The equation (4.15b) shows that the vertical velocity $\tilde{U}_{z1}$ forces the angular velocity correction Ω_1. This comes from the non-traditional Coriolis force in the horizontal momentum equation. The corresponding buoyancy and vertical vorticity corrections are given by $\tilde{B}_1 = i\Omega_c\tilde{U}_{z1}$ and $\zeta_1 = r_c\partial\Omega_1/\partial\tilde{r}$.

The linear solutions derived by Toghraei & Billant (2022) can be most simply obtained from (4.15) by neglecting the third term in the left-hand side of (4.15a). Indeed, the linear solutions are expected to be valid when $\widetilde{Re} \ll 1$, i.e. when $Re/\widetilde{Ro}^2 \ll 1$. In this case, (4.15a) can be integrated analytically

$$\tilde{U}_{z1} = \mathrm{i}\frac{\mathcal{A}}{\pi}\int_0^{|\Omega_c'|T/\gamma} \exp\left(-\frac{z^3}{3} + \mathrm{i}\gamma\tilde{r}z\right)\mathrm{d}z, \tag{4.16}$$

where

$$\mathcal{A} = \frac{\pi r_c \Omega_c}{2\left|2\Omega_c'\right|^{2/3}\left(1+\dfrac{1}{Sc}\right)^{1/3}}, \qquad \gamma = \frac{\left|2\Omega_c'\right|^{1/3}}{\left(1+\dfrac{1}{Sc}\right)^{1/3}}. \tag{4.17}$$

Then, the solution of (4.15b) can be found in the form

$$\Omega_1 = -\frac{\mathcal{A}}{2\gamma\pi r_c}\int_0^{\left|\Omega_c'\right|T} \exp\left(\frac{-q^3}{3\gamma^3}+\mathrm{i}q\tilde{r}\right)\left(\frac{1-\exp\left(q^3/\left|\Omega_c'\right|-q^2T\right)}{q^2}\right)\mathrm{d}q + c.c.. \tag{4.18}$$

These theoretical solutions are compared in figure 4.10 to the flows observed in the DNS prior to the onset of the instability for the four values of $\widetilde{Ro}$ investigated previously for $Re = 2000$ and $F_h = 4$. This figure displays the maximum vertical velocity $U_{zm}(\theta, t)$ for $\theta = 0$ (figure 4.10(a)) and $\theta = \pi/2$ (figure 4.10(b)). The solid lines correspond to the DNS for $\widetilde{Ro} = 40$ (grey), $\widetilde{Ro} = 60$ (green), $\widetilde{Ro} = 80$ (red) and $\widetilde{Ro} = 115$ (blue) whereas the corresponding linear and non-linear solutions (4.13,4.16) and (4.13,4.15) are plotted with dashed lines and dotted dashed lines, respectively, with the same color.

Both the linear (4.13,4.16) and the non-linear (4.13,4.15) solutions predict well the initial increase of $U_{zm}(\theta, t)$ in the DNS for all values of $\widetilde{Ro}$ despite missing the initial oscillations observed in the DNS. These oscillations are due to inertia-gravity waves excited at $t = 0$. However, since their amplitude remains constant whereas the rest of the solution grows linearly with time, their relative importance becomes negligible for large times. They are absent in (4.16) and (4.15) because these solutions are valid only for $T \gtrsim \mathcal{O}(1)$, i.e. large time: $t \gg \varepsilon^{-2/3}\widetilde{Re}^{1/3}$.

After the linear increase, there is a saturation of $U_{zm}(\theta, t)$ towards a level which is inversely proportional to $\widetilde{Ro}$. While the linear solution (4.13,4.16) saturates to constant values, the non-linear solution (4.13,4.15) exhibits transient oscillations towards a mean value. The amplitude of these oscillations increases as $\widetilde{Ro}$ decreases. The difference between the linear and non-linear solutions also increases as $\widetilde{Ro}$ decreases for a constant Re since non-linear effects scale like $\widetilde{Re} = Re/\widetilde{Ro}^2$.

Figures 4.11 and 4.12 display a detailed comparison between the radial profiles of the vertical velocity in the DNS and from the asymptotic solutions for $\widetilde{Ro} = 40$ and $\widetilde{Ro} = 115$, respectively. The comparison has been conducted at $\theta = 0$ (left column) and $\theta = \pi/2$ (middle column) and at two different times denoted t_{b1} and t_{b2}. The first time t_{b1} is approximately when $U_{zm}(\theta = 0, t)$ given by the non-linear equations (4.13,4.15) reaches the saturation level of $U_{zm}(\theta = 0, t)$ given by the linear solution (4.16) (circles in figure 4.10(a)). The time t_{b2} is when $U_{zm}(\theta = 0, t)$ given by the non-linear solution (4.13,4.15) reaches its first peak (squares in figure 4.10(a)). These two times are sufficiently large for the theoretical solutions to be valid. For both values of $\widetilde{Ro}$, there is a good agreement between $U_z(r, \theta, t)$ in the DNS (black solid lines) and predicted by the linear solutions (green dashed lines) and non-linear solutions (red dashed lines). However, the linear solution for $\widetilde{Ro} = 40$ (figure 4.11(a, b, d, e)) is shifted along the radius compared to the DNS whereas the non-linear solution is in

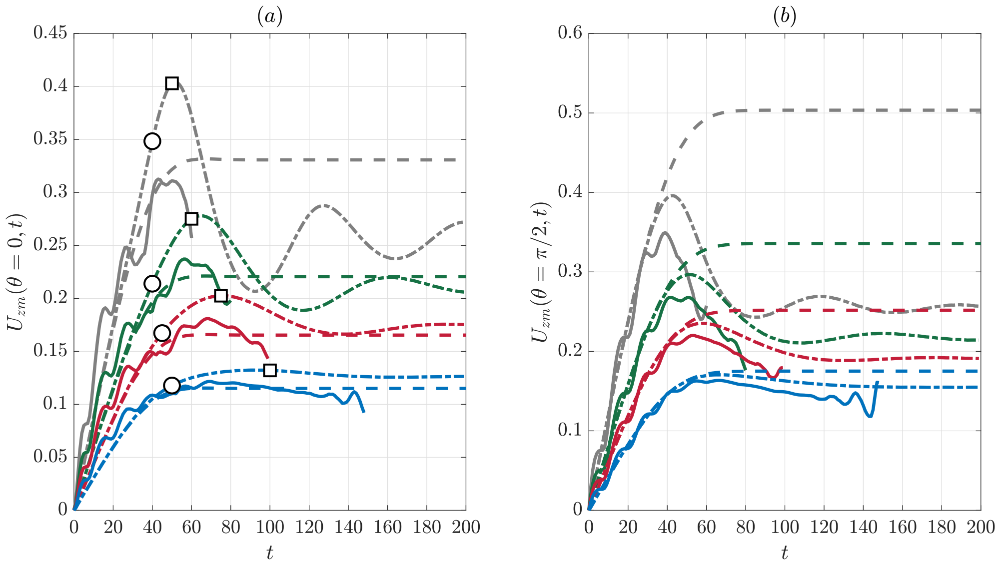

Fig. 4.10: Comparison between the maximum vertical velocity in the DNS (solid line), predicted by the linear solution (4.13,4.16) (dashed line) and by the non-linear equations (4.13,4.15) (dotted dashed line) for (a) $\theta = 0$ and (b) $\theta = \pi/2$ for $Re = 2000$, $F_h = 4$, $\Omega_b = 0.1$ $(Ro \approx 20)$ and $\widetilde{Ro} = 40$ (grey lines), $\widetilde{Ro} = 60$ (green lines), $\widetilde{Ro} = 80$ (red lines) and $\widetilde{Ro} = 115$ (blue lines). The circle and square symbols in (a) indicate the times t_{b1} and t_{b2}, respectively.

better agreement. This is due to the non-linear effect involving the angular velocity correction Ω_1 in (4.15a) that effectively moves the location of the critical radius. For $\widetilde{Ro} = 115$ (figure 4.12), there is also a slight shift between the linear and non-linear vertical velocity profiles at $t_b = 100$ (figure 4.12(d, e)). It is however smaller since non-linear effects are weaker for $\widetilde{Ro} = 115$.

The corresponding profiles of vertical vorticity at the same times are compared in figure 4.11(c, f) $(\widetilde{Ro} = 40)$ and figure 4.12(c, f) $(\widetilde{Ro} = 115)$. We see that there is also a good agreement between the asymptotic solutions and the DNS. The non-linear solution is, again, more accurate than the linear one for $\widetilde{Ro} = 40$ (figure 4.11(c, f)).

Similar comparisons are displayed in appendix A for $\widetilde{Ro} = 60$ (figure 4.28) and $\widetilde{Ro} = 80$ (figure 4.29).

4.5.2 Local stability analysis of the base flow in the critical layer

Having shown that the asymptotic solutions (4.13) are in good agreement with the flows observed in the DNS before the onset of the instabilities, we will now study the stability of these theoretical solutions in order to further understand the competition between the two-dimensional and three-dimensional instabilities. To do so, the equations (4.2-4.4), written in cylindrical coordinates, are linearized around the flow (4.13) and are expressed in terms of the local coordinate $\tilde{r}$ and with the vertical coordinate rescaled

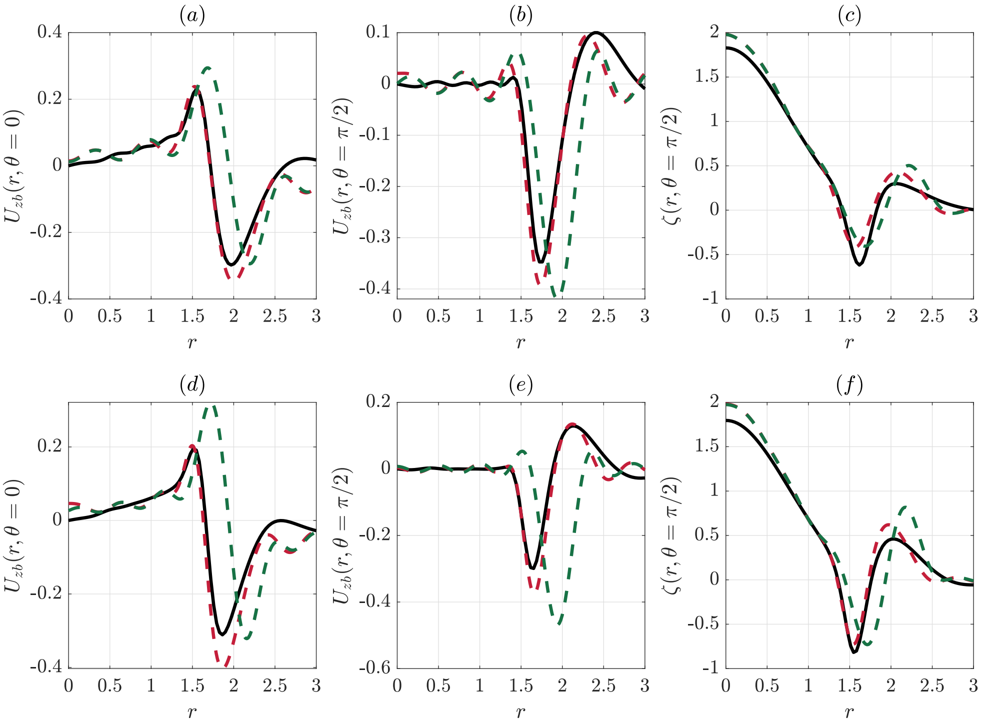

Fig. 4.11: Comparison between the vertical velocity at $\theta = 0$ (left column) and $\theta = \pi/2$ (middle column) in the DNS (black solid line), predicted by the linear solution (4.13,4.16) (green dashed line) and by the non-linear equations (4.13,4.15) (red dashed line) at $t_{b1} = 40$ (top row) and $t_{b2} = 50$ (bottom row) for $\widetilde{Ro} = 40$ and $Re = 2000$, $F_h = 4$, $Ro = 23.1$.

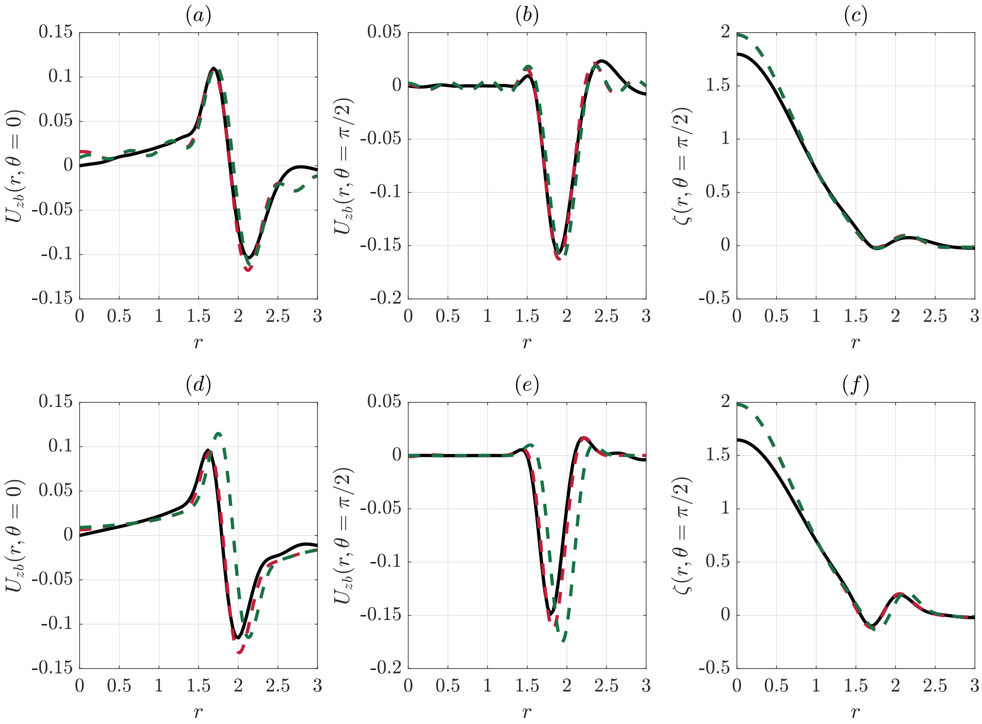

Fig. 4.12: Comparison between the vertical velocity at $\theta = 0$ (left column) and $\theta = \pi/2$ (middle column) in the DNS (black solid line), predicted by the linear solution (4.13,4.16) (green dashed line) and by the non-linear equations (4.13,4.15) (red dashed line) at $t_{b1} = 50$ (top row) and $t_{b2} = 100$ (bottom row) for $\widetilde{Ro} = 115$ and $Re = 2000$, $F_h = 4$, $Ro = 20.3$.

similarly: $\tilde{z} = \varepsilon^{-2/3}\widetilde{Re}^{1/3} z$. They read at leading orders in ε:

$$\varepsilon^{-2/3}\widetilde{Re}^{1/3}\frac{\partial u_r}{\partial \tilde{r}} + \frac{1}{r_c}\frac{\partial u_\theta}{\partial \theta} + \varepsilon^{-2/3}\widetilde{Re}^{1/3}\frac{\partial u_z}{\partial \tilde{z}} = 0, \tag{4.19a}$$

$$\begin{aligned}&\frac{\partial u_r}{\partial t} + \Omega\frac{\partial u_r}{\partial \theta} + \varepsilon^{-1/3}\widetilde{Re}^{2/3}\tilde{U}_z\frac{\partial u_r}{\partial \tilde{z}} - \left(2\Omega + \frac{2}{Ro}\right)u_\theta = -\varepsilon^{-2/3}\widetilde{Re}^{1/3}\frac{\partial p}{\partial \tilde{r}}\\ &- \varepsilon u_z\cos(\theta) + \varepsilon^{2/3}\widetilde{Re}^{-1/3}\left(\frac{\partial^2 u_r}{\partial \tilde{r}^2} + \frac{\partial^2 u_r}{\partial \tilde{z}^2}\right),\end{aligned} \tag{4.19b}$$

$$\begin{aligned}&\frac{\partial u_\theta}{\partial t} + \Omega\frac{\partial u_\theta}{\partial \theta} + \varepsilon^{-1/3}\widetilde{Re}^{2/3}\tilde{U}_z\frac{\partial u_\theta}{\partial \tilde{z}} + \left(\zeta + \frac{2}{Ro}\right)u_r = -\frac{1}{r_c}\frac{\partial p}{\partial \theta} + \varepsilon u_z\sin(\theta)\\ &+ \varepsilon^{2/3}\widetilde{Re}^{-1/3}\left(\frac{\partial^2 u_\theta}{\partial \tilde{r}^2} + \frac{\partial^2 u_\theta}{\partial \tilde{z}^2}\right),\end{aligned} \tag{4.19c}$$

$$\begin{aligned}&\frac{\partial u_z}{\partial t} + \Omega\frac{\partial u_z}{\partial \theta} + \varepsilon^{1/3}\widetilde{Re}^{1/3}\frac{u_\theta}{r_c}\frac{\partial \tilde{U}_z}{\partial \theta} + \varepsilon^{-1/3}\widetilde{Re}^{2/3}\tilde{U}_z\frac{\partial u_z}{\partial \tilde{z}} + \varepsilon^{-1/3}\widetilde{Re}^{2/3}u_r\frac{\partial \tilde{U}_z}{\partial \tilde{r}} =\\ &- \varepsilon^{-2/3}\widetilde{Re}^{1/3}\frac{\partial p}{\partial \tilde{z}} + b + \varepsilon u_r\cos(\theta) - \varepsilon u_\theta\sin(\theta) + \varepsilon^{2/3}\widetilde{Re}^{-1/3}\left(\frac{\partial^2 u_z}{\partial \tilde{r}^2} + \frac{\partial^2 u_z}{\partial \tilde{z}^2}\right),\end{aligned} \tag{4.19d}$$

$$\begin{aligned}&\frac{\partial b}{\partial t} + \Omega\frac{\partial b}{\partial \theta} + \varepsilon^{1/3}\widetilde{Re}^{1/3}\frac{u_\theta}{r_c}\frac{\partial \tilde{B}}{\partial \theta} + \varepsilon^{-1/3}\widetilde{Re}^{2/3}\tilde{U}_z\frac{\partial b}{\partial \tilde{z}} + \varepsilon^{-1/3}\widetilde{Re}^{2/3}u_r\frac{\partial \tilde{B}}{\partial \tilde{r}} =\\ &- \frac{u_z}{F_h^2} + \frac{\varepsilon^{2/3}}{\widetilde{Re}^{1/3}Sc}\left(\frac{\partial^2 b}{\partial \tilde{r}^2} + \frac{\partial^2 b}{\partial \tilde{z}^2}\right),\end{aligned} \tag{4.19e}$$

where

$$\Omega = \Omega_c + \varepsilon^{2/3}\widetilde{Re}^{-1/3}[\tilde{r}\Omega_c' + \widetilde{Re}\Omega_1] + ..., \tag{4.20a}$$

$$\zeta = \zeta_c + \widetilde{Re}\zeta_1 + \varepsilon^{2/3}\widetilde{Re}^{-1/3}\tilde{r}\zeta_c' + ... \tag{4.20b}$$

Local three-dimensional stability analysis

We see that the leading terms in (4.19) scale as $\varepsilon^{-1/3}\widetilde{Re}^{2/3}$ provided that $\partial/\partial\tilde{z}$ is of order unity. Hence, in order to study the three-dimensional instability, we rescale the time as follows $t = \tau\tilde{t}$ where $\tau = \varepsilon^{1/3}\widetilde{Re}^{-2/3}$ and the pressure as $p = \tau\widetilde{Re}\tilde{p}$ such that the time derivatives and the pressure gradient are of the same order as the dominant terms. Then, (4.19) reduces at first and second order in ε to:

$$\frac{\partial u_r}{\partial \tilde{t}} + \tilde{U}_z\frac{\partial u_r}{\partial \tilde{z}} + \tau\Omega_c\frac{\partial u_r}{\partial \theta} - \tau\left(2\Omega_c + \frac{2}{Ro}\right)u_\theta = -\frac{\partial \tilde{p}}{\partial \tilde{r}} \tag{4.21a}$$

$$\frac{\partial u_\theta}{\partial \tilde{t}} + \tilde{U}_z\frac{\partial u_\theta}{\partial \tilde{z}} + \tau\Omega_c\frac{\partial u_\theta}{\partial \theta} + \tau\left(\zeta_c + \widetilde{Re}\zeta_1 + \frac{2}{Ro}\right)u_r = 0, \tag{4.21b}$$

$$\frac{\partial u_z}{\partial \tilde{t}} + \tilde{U}_z \frac{\partial u_z}{\partial \tilde{z}} + u_r \frac{\partial \tilde{U}_z}{\partial \tilde{r}} + \tau \Omega_c \frac{\partial u_z}{\partial \theta} = -\frac{\partial \tilde{p}}{\partial \tilde{z}} + \tau b, \tag{4.21c}$$

$$\frac{\partial b}{\partial \tilde{t}} + \tilde{U}_z \frac{\partial b}{\partial \tilde{z}} + u_r \frac{\partial \tilde{B}}{\partial \tilde{r}} + \tau \Omega_c \frac{\partial b}{\partial \theta} = -\tau \frac{u_z}{F_h^2}, \tag{4.21d}$$

$$\frac{\partial u_r}{\partial \tilde{r}} + \frac{\partial u_z}{\partial \tilde{z}} = 0, \tag{4.21e}$$

whereas terms of order $\varepsilon^{2/3}$ and higher are neglected. If only the leading order terms are retained, then all the terms proportional to τ can be neglected and (4.21) reduces simply to

$$\frac{\partial u_r}{\partial \tilde{r}} + \frac{\partial u_z}{\partial \tilde{z}} = 0, \tag{4.22a}$$

$$\frac{\partial u_r}{\partial \tilde{t}} + \tilde{U}_z \frac{\partial u_r}{\partial \tilde{z}} = -\frac{\partial \tilde{p}}{\partial \tilde{r}}, \tag{4.22b}$$

$$\frac{\partial u_z}{\partial \tilde{t}} + \tilde{U}_z \frac{\partial u_z}{\partial \tilde{z}} + u_r \frac{\partial \tilde{U}_z}{\partial \tilde{r}} = -\frac{\partial \tilde{p}}{\partial \tilde{z}}, \tag{4.22c}$$

whereas the equations (4.21b) and (4.21d) for u_θ and b do not need to be considered since these two quantities do not appear in (4.22).

Hence, as shown previously by Boulanger *et al.* (2008), the local stability problem (4.22) corresponds at leading order to the two-dimensional stability of a parallel non-stratified shear flow $\tilde{U}_z$. However, a difference with the classical configuration is that the base flow $\tilde{U}_z$ does not depend only on $\tilde{r}$ but also on θ. Boulanger *et al.* (2008) have solved (4.22) by writing the perturbations in the form $(u_r, u_z, \tilde{p}) = [\hat{u}_r, \hat{u}_z, \hat{p}]\,(\tilde{r}, \theta)\mathrm{e}^{\tilde{\sigma}\tilde{t} + \mathrm{i}\tilde{k}\tilde{z}} + c.c.$. Then, (4.22) recovers the classical Rayleigh equation

$$\left[\tilde{\sigma} + \mathrm{i}\tilde{k}\tilde{U}_z\right]\left[\frac{\mathrm{d}^2}{\mathrm{d}\tilde{r}^2} - \tilde{k}^2\right]\hat{u}_r = \mathrm{i}\tilde{k}\frac{\mathrm{d}^2\tilde{U}_z}{\mathrm{d}\tilde{r}^2}\hat{u}_r, \tag{4.23}$$

where θ can be considered as an external parameter. The solution is then thought as a local eigenmode around the particular value of θ investigated.

If we consider also the next order terms in ε in (4.21), the previous local approach can be still used only if we neglect the advection terms in the azimuthal direction, i.e. $\Omega_c \partial/\partial\theta = 0$. Without this strong assumption, (4.21) would correspond to a full three-dimensional stability problem of a base flow varying in both $\tilde{r}$ and θ directions. Hence, it would be as complicated to solve as the stability analysis of the DNS flow performed in section §4.4.

In contrast, the simplifying assumption $\partial/\partial\theta = 0$ allows us to still consider θ as an external parameter. Hence, by writing perturbations in the form $(u_r, u_z, \tilde{p}, b) = \left[\hat{u}_r, \hat{u}_z, \hat{p}, \hat{b}\right](\tilde{r}, \theta)\mathrm{e}^{\tilde{\sigma}\tilde{t} + \mathrm{i}\tilde{k}\tilde{z}} + c.c.$, (4.21) can be reduced to a single equation

$$\begin{aligned}\tilde{s}\left[\left(1 + \frac{\tilde{N}^2}{\tilde{s}^2}\right)\frac{\mathrm{d}^2\hat{u}_r}{\mathrm{d}\tilde{r}^2} - \tilde{k}^2\left(1 + \frac{\tilde{\phi}}{\tilde{s}^2}\right)\hat{u}_r\right] &= \mathrm{i}\tilde{k}\left[\frac{\mathrm{d}^2\tilde{U}_z}{\mathrm{d}\tilde{r}^2} + \frac{\tilde{N}}{\tilde{s}}\frac{\mathrm{d}^2\tilde{B}'}{\mathrm{d}\tilde{r}^2} - \mathrm{i}\frac{\tilde{k}\tilde{N}}{\tilde{s}^2}\frac{\mathrm{d}\tilde{U}_z}{\mathrm{d}\tilde{r}}\frac{\mathrm{d}\tilde{B}'}{\mathrm{d}\tilde{r}}\right]\hat{u}_r \\ &+ \mathrm{i}\tilde{k}\left[\frac{\tilde{N}}{\tilde{s}}\frac{\mathrm{d}\tilde{B}'}{\mathrm{d}\tilde{r}} + \frac{\tilde{N}^2}{\tilde{s}^2}\frac{\mathrm{d}\tilde{U}_z}{\mathrm{d}\tilde{r}}\right]\frac{\mathrm{d}\hat{u}_r}{\mathrm{d}\tilde{r}},\end{aligned} \tag{4.24}$$

where $\tilde{s} = \tilde{\sigma} + \mathrm{i}\tilde{k}\tilde{U}_z$, $\tilde{B}' = \tilde{B}/\Omega_c$ and

$$\tilde{N} = \frac{\tau}{F_h}, \qquad \tilde{\phi} = \tau^2 \left(2\Omega_c + \frac{2}{Ro}\right)\left(\zeta_c + \frac{2}{Ro}\right) \tag{4.25}$$

are the inverse of the Froude number and the Rayleigh discriminant. The Rayleigh equation (4.23) is recovered by (4.24) when $\tau = 0$, i.e. $\tilde{N} = 0$ and $\tilde{\phi} = 0$. Since (4.24) is still one-dimensional, it will allow us to study simply the second order effects. This equation is effectively solved by means of a pseudo-spectral Chebyshev method and the function *eig* from Matlab.

The dependence of $\tilde{U}_z$ and $\tilde{B}'$ on the parameters r_c and Sc can be further eliminated for a large time by the additional rescaling

$$\begin{aligned} &\tilde{U}_z = \hat{U}_z\mathcal{A}, \quad \tilde{B}' = \hat{B}\mathcal{A}, \quad \tilde{r} = \frac{\hat{r}}{\gamma}, \quad \tilde{k} = \hat{k}\gamma, \quad \tilde{\sigma} = \hat{\sigma}\gamma\mathcal{A}, \quad \tau = \hat{\tau}\gamma\mathcal{A}, \\ &\tilde{N} = \hat{N}\gamma\mathcal{A}, \quad \tilde{\phi} = \hat{\phi}(\gamma\mathcal{A})^2, \end{aligned} \tag{4.26}$$

where $\mathcal{A}$ and γ are defined in (4.17). Then, the equation has the same form as (4.24) but with tildes replaced by hats.

Figure 4.13 shows the normalized growth rate $\hat{\sigma}_r$ as a function of the normalized wavenumber $\hat{k}$ given by (4.24) for different $\hat{N}$ and $\hat{\phi}$. The linear solution (4.13,4.16) for $T = Re^{-1/3}t = \infty$ is taken as base flow for two angles $\theta = 0$ (solid line) and $\theta = \pi/2$ (dashed line). For $\hat{N} = \hat{\phi} = 0$ (black line) corresponding to the Rayleigh equation (4.23), the maximum growth rate $\hat{\sigma}_{rmax}$ is $\hat{\sigma}_{rmax} \approx 0.116$ for $\hat{k}_{max} \approx 0.54$ when $\theta = 0$ and $\hat{\sigma}_{rmax} \approx 0.107$ for $\hat{k}_{max} \approx 0.59$ when $\theta = \pi/2$. The flow is therefore slightly more unstable for $\theta = 0$ in agreement with the results of Boulanger *et al.* (2008). Since the time has been scaled by τ, this implies that the maximum unscaled growth rate is proportional to $\sigma_r \sim 1/\tau = \varepsilon^{-1/3}\widetilde{Re}^{2/3}$.

The effect of $\hat{N}$ for $\hat{\phi} = 0$ is investigated in figure 4.13(a). When $\hat{N}$ is increased to $\hat{N} = 0.1$ (red lines) and then to $\hat{N} = 0.2$ (green lines), there is a significant decrease of the maximum growth rate both for $\theta = 0$ (solid lines) and $\theta = \pi/2$ (dashed lines). Similarly, when $\hat{\phi}$ is varied while $\hat{N}$ is kept to zero (figure 4.13(b)), the maximum growth rates drop dramatically as soon as $\hat{\phi}$ becomes non-zero: $\hat{\phi} = 0.005$ (red line), $\hat{\phi} = 0.02$ (green line). In terms of the original parameters, the control parameters $\hat{N}$ and $\hat{\phi}$ are proportional to $\widetilde{Ro}/Re^{2/3}$ and $\widetilde{Ro}^2/Re^{4/3}$, respectively. When the non-traditional Rossby number $\widetilde{Ro}$ is increased or the Reynolds number is decreased, we expect therefore the growth rate to deviate more and more from the one given by the Rayleigh equation (4.23). Similarly, the dependencies of $\hat{N}$ on the Froude number or of $\hat{\phi}$ on the traditional Rossby number imply a decrease of the growth rate as F_h decreases, or as Ro decreases.

In summary, the maximum unscaled growth rate σ_r of three-dimensional disturbances scales at leading order as $\varepsilon^{-1/3}\widetilde{Re}^{2/3} = \varepsilon Re^{2/3}$ but second order effects measured by the parameters $\hat{N}$ and $\hat{\phi}$ can reduce significantly σ_r.

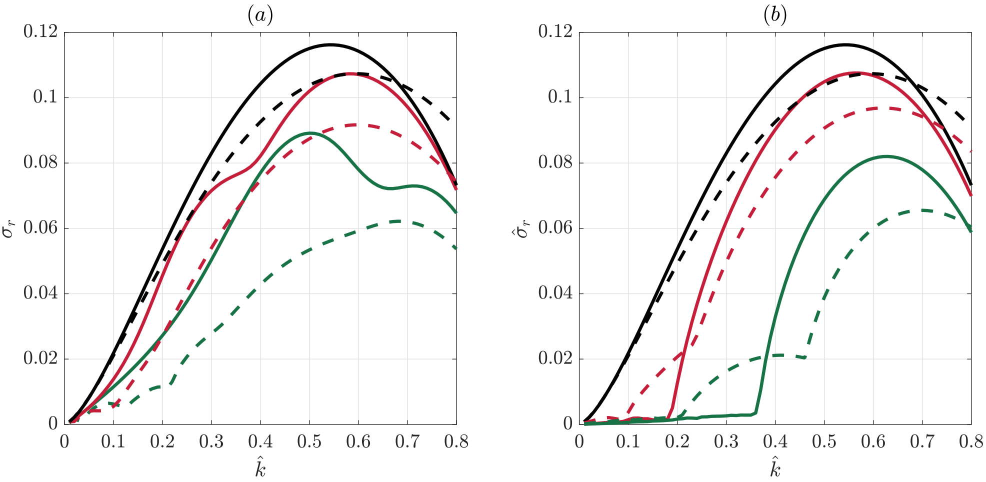

Fig. 4.13: Normalized growth rate $\hat{\sigma}_r$ obtained from (4.24) as a function of the normalized vertical wavenumber $\hat{k}$. The linear base flow (4.13,4.16) is taken at $T = \infty$ for $\theta = 0$ (solid line) and $\theta = \pi/2$ (dashed line). The different colored curves correspond to: (*a*) $\hat{N} = 0$, $\hat{\phi} = 0$ (black line), $\hat{N} = 0.1$, $\hat{\phi} = 0$ (red line) and $\hat{N} = 0.2$, $\hat{\phi} = 0$ (green line) and (*b*) $\hat{N} = 0$, $\hat{\phi} = 0$ (black line), $\hat{N} = 0$, $\hat{\phi} = 0.005$ (red line) and $\hat{N} = 0$, $\hat{\phi} = 0.02$ (green line).

Local two-dimensional stability analysis

The equations (4.21) have been obtained thanks to the assumption $\partial/\partial z = \mathcal{O}(\varepsilon^{-2/3}\widetilde{Re}^{1/3})$, i.e. that the perturbations vary along the vertical as rapidly as along the radius. In other words, the dimensional vertical wavenumber k should be large.

These equations are therefore not valid when k is small and in particular in the two-dimensional limit $\partial/\partial z = 0$. To treat this limit, we introduce the different scaling

$$p = \widetilde{Re}^{-1/3}\varepsilon^{2/3}\bar{p}, \tag{4.27a}$$

$$\frac{\partial}{\partial\theta} = \widetilde{Re}^{1/3}\varepsilon^{-2/3}\frac{\partial}{\partial\bar{\theta}}, \tag{4.27b}$$

$$\frac{\partial}{\partial\bar{t}} = \frac{\partial}{\partial t} + \Omega_c\widetilde{Re}^{1/3}\varepsilon^{-2/3}\frac{\partial}{\partial\bar{\theta}}, \tag{4.27c}$$

where the new time $\bar{t}$ is introduced to conveniently simplify the following calculations. Then, (4.19) reduces at leading order in ε to

$$\frac{\partial u_r}{\partial\bar{t}} + \left(\tilde{r}\Omega_c' + \widetilde{Re}\Omega_1\right)\frac{\partial u_r}{\partial\bar{\theta}} - \left(2\Omega_c + \frac{2}{Ro}\right)u_\theta = -\frac{\partial\bar{p}}{\partial\tilde{r}} \tag{4.28a}$$

$$\frac{\partial u_\theta}{\partial\bar{t}} + \left(\tilde{r}\Omega_c' + \widetilde{Re}\Omega_1\right)\frac{\partial u_\theta}{\partial\bar{\theta}} + \left(\zeta_c + \widetilde{Re}\zeta_1 + \frac{2}{Ro}\right)u_r = -\frac{1}{r_c}\frac{\partial\bar{p}}{\partial\bar{\theta}} \tag{4.28b}$$

$$\frac{\partial u_r}{\partial\tilde{r}} + \frac{1}{r_c}\frac{\partial u_\theta}{\partial\bar{\theta}} = 0, \tag{4.28c}$$

whereas the equations (4.19d,4.19e) for u_z and b do not need to be considered since they are decoupled from (4.28). By introducing perturbations of the form $(u_r, u_\theta, \bar{p}) = (\hat{u}_r(r), \hat{u}_\theta(r), \hat{p}(r))\mathrm{e}^{\sigma\bar{t} + \mathrm{i}\bar{m}\bar{\theta}}$, a Rayleigh equation is again recovered

$$\left[\frac{\sigma}{\widetilde{Re}} + \mathrm{i}\bar{m}\left(\frac{\tilde{r}\Omega_c'}{\widetilde{Re}} + \Omega_1\right)\right]\left[\frac{\partial^2}{\partial\tilde{r}^2} - \frac{\bar{m}^2}{r_c^2}\right]\hat{u}_r = \mathrm{i}\frac{\bar{m}}{r_c}\frac{\partial\zeta_1}{\partial\tilde{r}}\hat{u}_r. \tag{4.29}$$

It is the same as (4.23) with $r_c\left(\tilde{r}\Omega_c'/\widetilde{Re} + \Omega_1\right)$ and $\bar{m}/r_c$ replacing $\tilde{U}_z$ and k, respectively. This equation governs the growth rate of azimuthal disturbances on the local azimuthal velocity profile near the critical layer.

In contrast to the three-dimensional case, the dependence on $\widetilde{Re}$ can not be completely eliminated from (4.29). This is because the angular velocity correction Ω_1 is of the same order as the term $\tilde{r}\Omega_c'/\widetilde{Re}$ of the pre-existing angular velocity Ω_0. However, most of the dependence of Ω_1 on r_c can be eliminated by the further rescaling $\tilde{r} = \hat{r}/\gamma$, $\Omega_1 = \hat{\Omega}_1\mathcal{A}/(r_c\gamma^2)$, $\zeta_1 = \hat{\zeta}_1\mathcal{A}/\gamma$, $\bar{m} = \hat{m}r_c\gamma$, $\sigma = \hat{\sigma}\widetilde{Re}\mathcal{A}/\gamma$. Then, (4.29) becomes

$$\left[\hat{\sigma} + \mathrm{i}\hat{m}\left(-\hat{r}\chi + \hat{\Omega}_1\right)\right]\left[\frac{\partial^2}{\partial\hat{r}^2} - \hat{m}^2\right]\hat{u}_r = \mathrm{i}\hat{m}\frac{\partial^2\hat{\Omega}_1}{\partial\hat{r}^2}\hat{u}_r, \tag{4.30}$$

where the control parameter χ is

$$\chi = \frac{|\Omega_c'|\gamma r_c}{\widetilde{Re}\mathcal{A}}. \tag{4.31}$$

This parameter depends on the Froude number F_h through the position of the critical layer, the Reynolds number Re and the non-traditional Rossby number $\widetilde{Ro}$ through $\widetilde{Re}$. Figure 4.14(a) shows the normalized growth rate $\hat{\sigma}_r$ obtained from (4.30) for three values of χ. The angular velocity correction $\hat{\Omega}_1$ has been taken as the linear solution (4.18) for $F_h = 4$, $Re = 2000$ at two different times $T = Re^{-1/3}t = 4$ (dashed line) and $T = 8$ (solid line). Since the angular velocity correction increases with time and saturates only when T is very large, the growth rates increase significantly when T varies from $T = 4$ to $T = 8$. These times correspond to $t = 50$ and $t = 100$ for $Re = 2000$. Figure 4.14(a) shows also that the maximum growth rate $\hat{\sigma}_{rmax}$ increases as χ increases from $\chi = 0.06$ (black line) to $\chi = 0.5$ (blue line). Such variation of χ corresponds to $\widetilde{Ro}$ varying from $\widetilde{Ro} = 40$ to $\widetilde{Ro} = 115$ for $F_h = 4$ and $Re = 2000$. Figure 4.14(b) displays the corresponding unscaled growth rate $\sigma_r = \hat{\sigma}_r \widetilde{Re} \mathcal{A}/\gamma$, as a function of the unscaled wavenumber $m = \hat{m}\widetilde{Re}^{1/3}\varepsilon^{-2/3}r_c\gamma$. The curves are now in reverse order compared to figure 4.14(a) since σ_r is proportional to $\widetilde{Re}\hat{\sigma}_r$. Hence, if $\hat{\sigma}_r$ were independent of $\widetilde{Re}$ and T, the maximum growth rate of the two-dimensional instability would simply scale as $\widetilde{Re} = Re\varepsilon^2$. However, since $\hat{\sigma}_r$ decreases via χ as $\widetilde{Re}$ increases, the dependence of σ_r on $\widetilde{Re}$ is slower than a linear relationship. Furthermore, since the instability appears earlier as $\widetilde{Re}$ increases, the time t_{b2} corresponds to approximately $T = 8$ for $\widetilde{Ro} = 115$ ($\widetilde{Re} = 0.6$) and $T = 4$ for $\widetilde{Ro} = 40$ ($\widetilde{Re} = 5$). Therefore, this effect also reduces the linear scaling of σ_r on $\widetilde{Re}$. It is also interesting to notice in figure 4.14(b) that the most unstable azimuthal wavenumber ranges from $m = 2$ to $m = 4$ depending on χ (i.e. $\widetilde{Re}$).

In summary, the unscaled growth rates of the two-dimensional and three-dimensional instabilities scale at leading order in ε like $\widetilde{Re} = \varepsilon^2 Re$ and $\varepsilon^{-1/3}\widetilde{Re}^{2/3} = \varepsilon Re^{2/3}$, respectively. From these scalings, one would therefore expect that the two-dimensional instability is dominant at large ε (i.e. small $\widetilde{Ro}$) and the three-dimensional instability at small ε for a given Reynolds number in contradiction with the results of the DNS (section §4.3) and the stability analysis (section §4.4). However, we will see in the next section that the additional dependencies of the growth rates on the parameters, discussed above, can account for the observations.

4.6 Comparison between the stability analyses of the DNS flows and the theoretical solutions in the critical layer

We now compare the predictions of the local stability analyses to the results of the stability analysis of the DNS flows performed in section §4.4. For each value of $\widetilde{Ro}$, the comparisons are conducted at the two different times t_{b1} and t_{b2} indicated in figure 4.10. In addition, the local three-dimensional stability analysis considers that $\theta = 0$ since the maximum growth rate is always larger than for $\theta = \pi/2$ (figure 4.13). We remind also that this analysis is expected to be valid only for large vertical wavenumbers.

Figure 4.15 compares the growth rate of the DNS flow (black line) for $\widetilde{Ro} = 40$ at $t_{b1} = 40$ (figure 4.15(a)) and $t_{b1} = 50$ (figure 4.15(b)) to the growth rate predicted

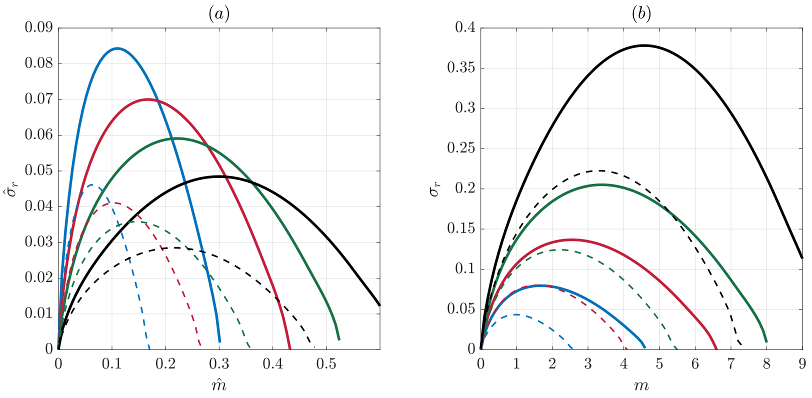

Fig. 4.14: (a) Normalized growth rate $\hat{\sigma}_r$ obtained from (4.30) as a function of the normalized azimuthal wavenumber $\hat{m}$ and (b) growth rate σ_r as a function of the azimuthal wavenumber m. The linear base flow (4.13,4.18) has been taken at $T = 4$ (dashed line) and $T = 8$ (solid line) for $Re = 2000$ and $F_h = 4$. The different colored curves correspond to: $\chi = 0.06$ (black line), $\chi = 0.13$ (green line), $\chi = 0.24$ (red line) and $\chi = 0.5$ (blue line).

by the local two-dimensional (square symbols) and three-dimensional (lines) analyses. The dashed and solid lines show the prediction of the leading order equation (4.23) and of the second order equation (4.24), respectively. The green and red colors correspond to the linear solution (4.13,4.16,4.18) and to the non-linear solution (4.13,4.15) as base flow, respectively.

The local three-dimensional stability analysis predicts a growth rate peak around $k \simeq 3 - 5$ whatever the base flow and the stability equation used, in good agreement with the stability analysis of the DNS flow at both times. Although there are some differences between the various predictions depending on which stability equation and which base flow solution are used, it is difficult to say that one is particularly in better agreement with the stability analysis of the DNS flow than the others. Away from the three-dimensional growth rate peak, the local stability analyses depart from the stability analysis of the DNS flow since the former neglect any azimuthal variations of the disturbances and of the base flow. However, at $k = 0$, the local two-dimensional stability analysis, that does take into account azimuthal disturbances, predicts a growth rate (square symbols) in good agreement with the growth rate computed at $k = 0$ for the DNS flow.

For $\widetilde{Ro} = 60$ (figure 4.16) and $\widetilde{Ro} = 80$ (figure 4.17), there are large differences between the growth rates obtained from the Rayleigh equation (4.23) and the second order equation (4.24). For both $\widetilde{Ro}$, the predictions of (4.24) are in much better agreement with the stability analysis of the DNS flow, especially the maximum growth rate values. The locations of the growth rate peak are also in good agreement except for $\widetilde{Ro} = 80$ at $t_{b1} = 45$ (figure 4.17(a)). We can also notice that there are much fewer differences between the green and red curves than for $\widetilde{Ro} = 40$ (figure 4.15) since the linear and non-linear solutions become closer as $\widetilde{Re} = 4Re/\widetilde{Ro}^2$ decreases, i.e. as $\widetilde{Ro}$ increases for a fixed Reynolds number Re. The local two-dimensional stability analysis (square symbols) is also in very good agreement with the stability analysis of the DNS flow at $k = 0$ and $t = t_{b2}$. For $t = t_{b1}$, the agreement is less good probably because the vorticity anomaly is less concentrated around the critical radius at this early time so that the local assumption is not well verified.

Finally figure 4.18 displays the comparison for $\widetilde{Ro} = 115$. Again, we can see that the local two-dimensional stability analysis agrees well with the stability analysis of the DNS flow at $t = t_{b2}$. There is again a large departure between the predictions of (4.23) and (4.24) but the maximum growth rate obtained from the second order equation (4.24) is in fair agreement with the black curves. However, the locations of the growth rate peaks are not well predicted. In appendix B, we have tested the effect of the assumption $\partial/\partial\theta = 0$ in the local three-dimensional stability analysis by considering perturbations comprising several azimuthal modes, i.e. $\boldsymbol{u} = \sum_{n=-N_m}^{N_m} \boldsymbol{u}_n \mathrm{e}^{in\theta}$ in (4.21), where N_m is the maximum azimuthal wavenumber considered. The growth rate peaks are then no longer located at the same wavenumbers but the maximum growth rate is approximately the same. In addition, some of the discrepancies might come from the next order terms in (4.19) which are neglected in (4.21). While in (4.19), the leading order terms that scale as $\varepsilon^{-1/3}\widetilde{Re}^{2/3} = Re^{2/3}/\widetilde{Ro}$ actually decrease as the non-traditional Rossby number $\widetilde{Ro}$ increases for a given Re, the third-order terms (in particular dissipation terms) that scale as $\varepsilon^{2/3}\widetilde{Re}^{-1/3} = 1/Re$ remain unchanged. Hence, the third-order terms could become important for large non-traditional Rossby numbers.

Figure 4.19 summarizes the figures 4.15, 4.16, 4.17 and 4.18 by showing the growth rate of the two-dimensional instability at $k = 0$ (dashed lines with square symbols) and the maximum growth rate of the three-dimensional instability (lines with circle symbols) as a function of the non-traditional Rossby number $\widetilde{Ro}$. The latter growth rate is taken as the maximum growth rate in the wavenumber range $k > 4$. For simplicity, only the results for the time $t = t_{b2}$ and the results of the local stability analyses of the non-linear flow (4.13,4.15) are plotted. The black curves represent again the growth rate obtained from the stability analysis of the DNS flows.

The growth rates of the two instabilities clearly decrease at different rates as the non-traditional Rossby number increases. From the stability analysis of the DNS flow, the two-dimensional instability is expected to become dominant for $\widetilde{Ro} \gtrsim 100$. A similar trend can also be seen in growth rates given by the local stability analyses, even if the cross-over between the two-dimensional and three-dimensional instabilities occurs for a somewhat larger non-traditional Rossby number: $\widetilde{Ro} \gtrsim 120$. Figure 4.19 demonstrates also that the growth rate predicted by the pure three-dimensional Rayleigh equation (4.23) (red dashed line with squares) decays slower than predicted by (4.24) as $\widetilde{Ro}$ increases and remains always well above the growth rate of the two-dimensional instability. It is therefore only the second order local stability equation (4.24) that can explain the transition between the two instabilities as $\widetilde{Ro}$ increases.

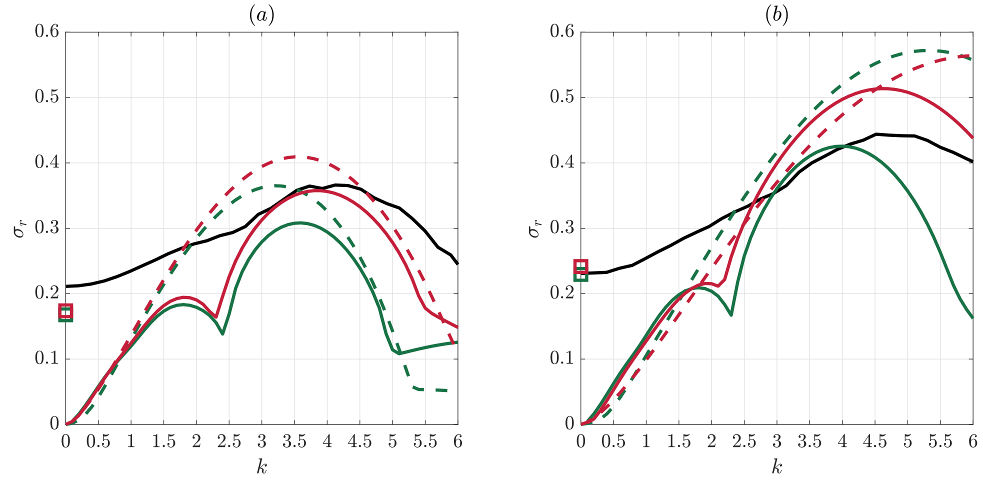

Fig. 4.15: Growth rate σ_r of the DNS flow (black solid line) and predicted by the local stability analyses (colored curves) as a function of the vertical wavenumber k for $\widetilde{Ro} = 40$ and $\mathrm{Re} = 2000$, $F_h = 4$, $Ro = 23.1$ at (a) $t_{b1} = 40$ and (b) $t_{b2} = 50$. The dashed and solid lines have been obtained from (4.23) and (4.24), respectively. The square symbols show the maximum growth rate obtained from the two-dimensional Rayleigh equation (4.29). Green and red colors correspond to the linear solution (4.13,4.16,4.18) and the non-linear solution (4.13,4.15), respectively.

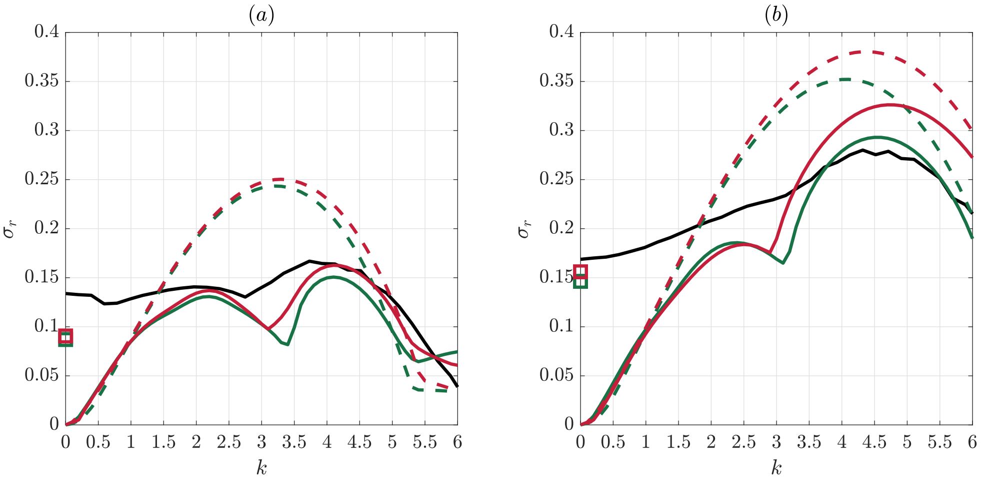

Fig. 4.16: Same as figure 4.15 but for $\widetilde{Ro} = 60$ and $Ro = 21.2$ at (a) $t_{b1} = 40$ and (b) $t_{b2} = 60$.

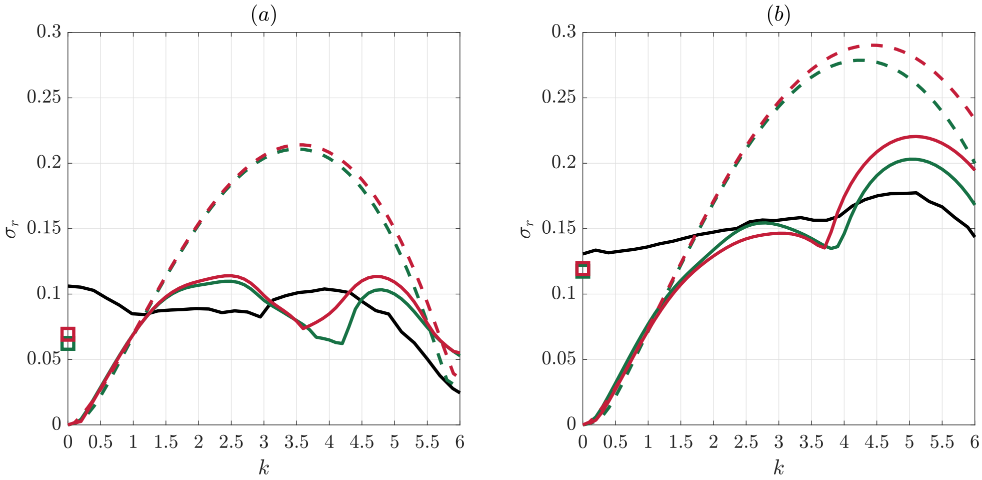

Fig. 4.17: Same as figure 4.15 but for $\widetilde{Ro} = 80$ and $Ro = 20.7$ at (a) $t_{b1} = 45$ and (b) $t_{b2} = 75$.

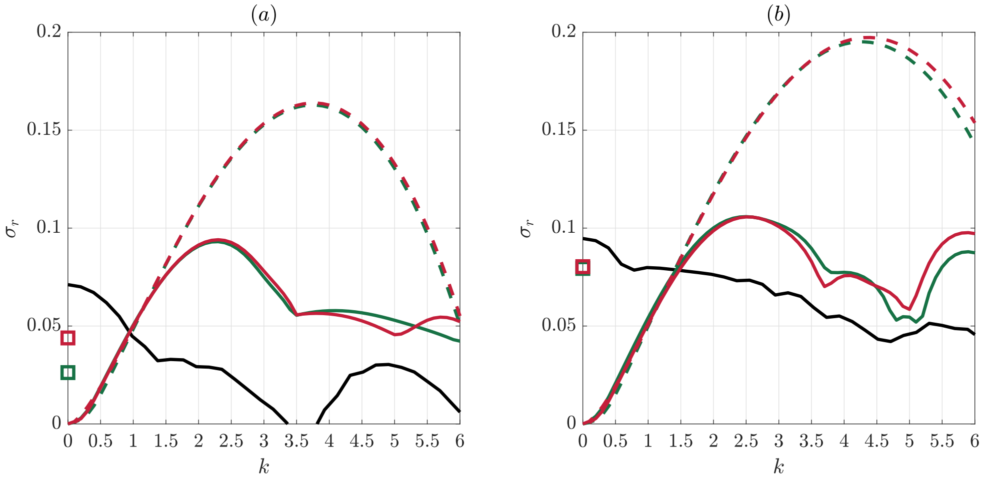

Fig. 4.18: Same as figure 4.15 but for $\widetilde{Ro} = 115$ and $Ro = 20.3$ at (a) $t_{b1} = 50$ and (b) $t_{b2} = 100$.

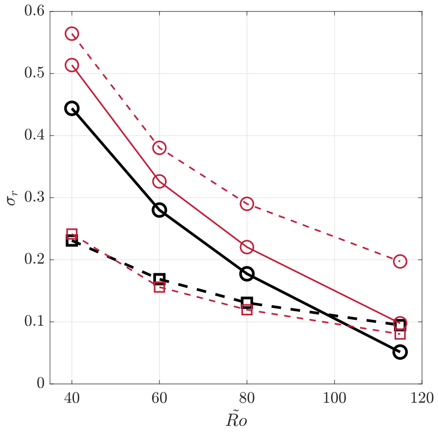

Fig. 4.19: Growth rates of the two-dimensional instability (lines with square symbols) and of the three-dimensional instability (lines with circle symbols) at $t = t_{b2}$ as a function of $\widetilde{Ro}$ for $Re = 2000$, $F_h = 4$ and $\Omega_b = 0.1$ ($Ro \approx 20$). The different colors correspond to the stability analysis of the DNS flow (black) and to the local stability equations (4.23) (red dashed line with circles), (4.24) (red solid line with circles) and (4.29) (red dashed line with squares) using the non-linear solution (4.13,4.15).

4.7 Parametric study

4.7.1 Effect of the Reynolds number

So far the Reynolds number has been fixed to $Re = 2000$, we now investigate the effect of a larger Reynolds number in the range $4000 \leq Re \leq 10000$ on the critical non-traditional Rossby number between the three-dimensional and two-dimensional instabilities. However, three-dimensional DNS for such Reynolds numbers would require very high resolutions. Since the maximum growth rates provided by the local stability analyses are in reasonable agreement with the stability analysis of the DNS flow (figure 4.19), the present study will be therefore based only on the local analyses.

Figure 4.20 displays the domain in the parameter space $(Re, \widetilde{Ro})$ where the two-dimensional instability (open light blue circles) and three-dimensional instability (open dark blue circles) are dominant. The open yellow circles represent the parameters for which the two-dimensional instability is stable for any azimuthal wavenumber larger than unity. The filled circles with the same color represent the observations made from the DNS for $Re = 2000$. The Froude number and background rotation rate are fixed to $F_h = 4$ and $\Omega_b = 0.1$ (i.e. $Ro \approx 20$) as before. The grey dashed line shows the theoretical critical non-traditional Rossby number for the existence of the two-dimensional instability derived in Toghraei & Billant (2022) (equation (3.71) for $F_h = 4$, $a = \infty$ and $c = 0.4$).

Figure 4.20 is therefore similar to figure 3.8 from chapter 3 except that the Froude number was lower $F_h = 2$ in the latter figure. We see in figure 4.20 that the two-dimensional instability should be the most dangerous instability in an intermediate region of $\widetilde{Ro}$ for each Reynolds number investigated. Three-dimensional instability is

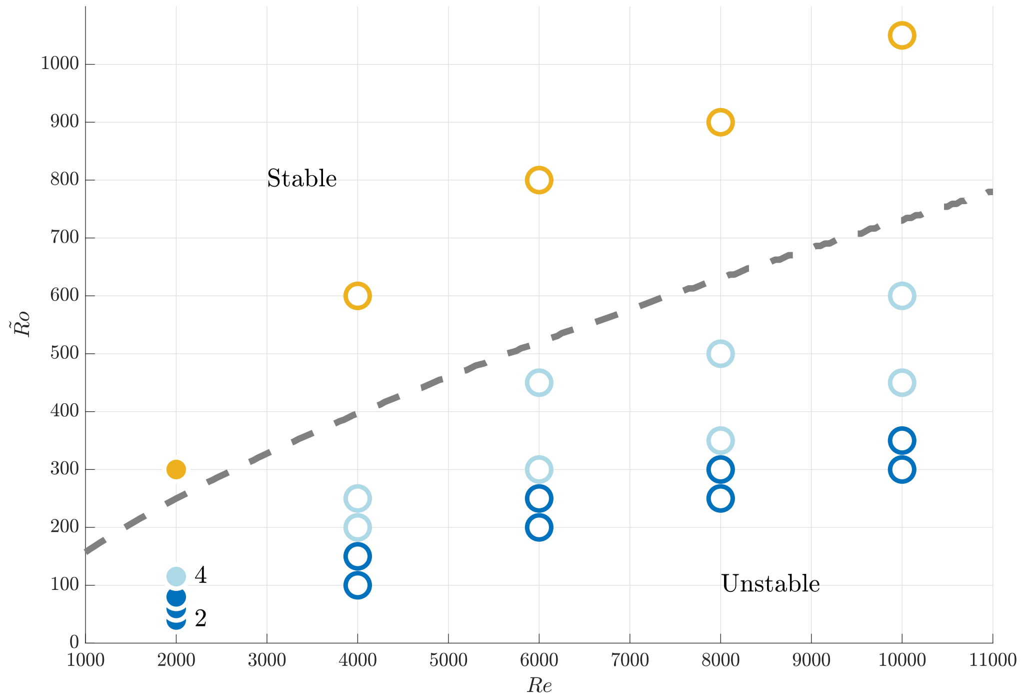

Fig. 4.20: Map of the dominant instability in the parameter space $(Re, \widetilde{Ro})$ for $F_h = 4$ and $\Omega_b = 0.1$ $(Ro \approx 20)$. Two-dimensional and three-dimensional instabilities are represented by light and dark blue circles, respectively. The two-dimensional instability has not been observed at the yellow circles. Filled and open circles correspond to the results of the stability analyses of the DNS flow and the local non-linear solution, respectively. The dashed grey line represents the criterion (3.71) from chapter 3 for $F_h = 4$, $a = \infty$ and $c = 0.4$.

dominant only for lower $\widetilde{Ro}$.

It seems however difficult to derive a theoretical criterion for the critical non-traditional Rossby number between the two-dimensional and three-dimensional instabilities. Indeed, this would require scaling laws for the growth rate of each instability in order to be able to compare their strength. Since the growth rate of the three-dimensional instability can be reasonably well predicted only by taking into account second order effects, it does not appear easy to obtain a simple scaling law for this instability. However, this might be possible by solving the stability problem (4.21) asymptotically with τ as a small parameter instead of solving it as a whole as done in (4.24). This approach will be tested in the future. Similarly, the dependence of the growth rate of the two-dimensional instability on Re and $\widetilde{Ro}$ is complicated (figure 4.14). Nonetheless, it could be worth trying in the future to obtain an analytic scaling law from (4.30).

4.7.2 Effect of the traditional Rossby number

The effect of the traditional Rossby number Ro has been investigated for the parameters $Re = 2000$, $F_h = 4$ and for a constant non-traditional Rossby number $\widetilde{Ro} = 40$ by means of DNS. When Ro is decreased from $Ro = 23.1$ (figures 4.2 and 4.3) to $Ro = 5$ (not shown), the three-dimensional instability continues to be observed but becomes weaker. However, when Ro is further decreased down to $Ro = 2.5$ (figures 4.21 and 4.22), the three-dimensional instability is no longer observed. The two-dimensional instability then develops at a later time (figures 4.21(c, f, i) and 4.22(c, f)).

The local stability analysis of the non-linear solution (4.13,4.15) has been investigated for the same parameters. Figure 4.23 shows the growth rates of the three-dimensional instability (red circles) and of the two-dimensional instability (red squares) as a function of the traditional Rossby number for $\widetilde{Ro} = 40$, $Re = 2000$ and $F_h = 4$. When the traditional Rossby number is reduced from $Ro = 23.1$ to $Ro = 2.5$, the growth rate of the three-dimensional instability drops and becomes almost equal to the growth rate of the two-dimensional instability that is independent of Ro. This can be explained thanks to the local three-dimensional stability analysis taking into account second order terms (4.24). The importance of these terms is controlled by the parameters $\hat{\phi}$ and $\hat{N}$. From (4.24), we can see that $\hat{\phi}$ depends on the inverse of the traditional Rossby number. Hence, $\hat{\phi}$ increases from $\hat{\phi} = 0.002$ for $Ro = 23.1$ to $\hat{\phi} = 0.046$ for $Ro = 2.5$. As shown in figure 4.13, the maximum growth rate decreases strongly when $\hat{\phi}$ increases only slightly. As a result, decreasing the traditional Rossby number Ro strongly damps the three-dimensional instability and favors the two-dimensional instability.

4.8 Conclusion

We have studied the three-dimensional evolution of a stratified vortex under the complete Coriolis force by means of DNS. When the initial conditions are purely two-dimensional, Toghraei & Billant (2022) have reported that the dynamics remains strictly two-dimensional but with three-velocity components. Due to the non-traditional Coriolis force, a vertical velocity field and vertical vorticity anomaly are generated in the flow at the critical radius r_c where the angular velocity of the vortex is equal to the inverse of the Froude number (the Brunt–Väisälä frequency in dimensional form) when it is larger than unity. The strengths of the vertical velocity field and vertical vorticity anomaly are proportional to $Re^{1/3}/\widetilde{Ro}$ and $Re/\widetilde{Ro}^2$, respectively. They are concentrated around the critical radius r_c over the viscous length scale $\tilde{r} = Re^{1/3}(r - r_c)$. Then, a two-dimensional shear instability develops for a sufficiently large non-traditional Rossby number $\widetilde{Ro}$ due to the inflection point created by the vorticity anomaly. This evolution resembles the one reported by Wang & Balmforth (2020, 2021) for a forced baroclinic critical layer in a horizontal shear flow.

To test the robustness of this dynamics with respect to small three-dimensional perturbations, we have performed DNS of the vortex disturbed initially by a small three-dimensional white noise for four different non-traditional Rossby numbers ranging

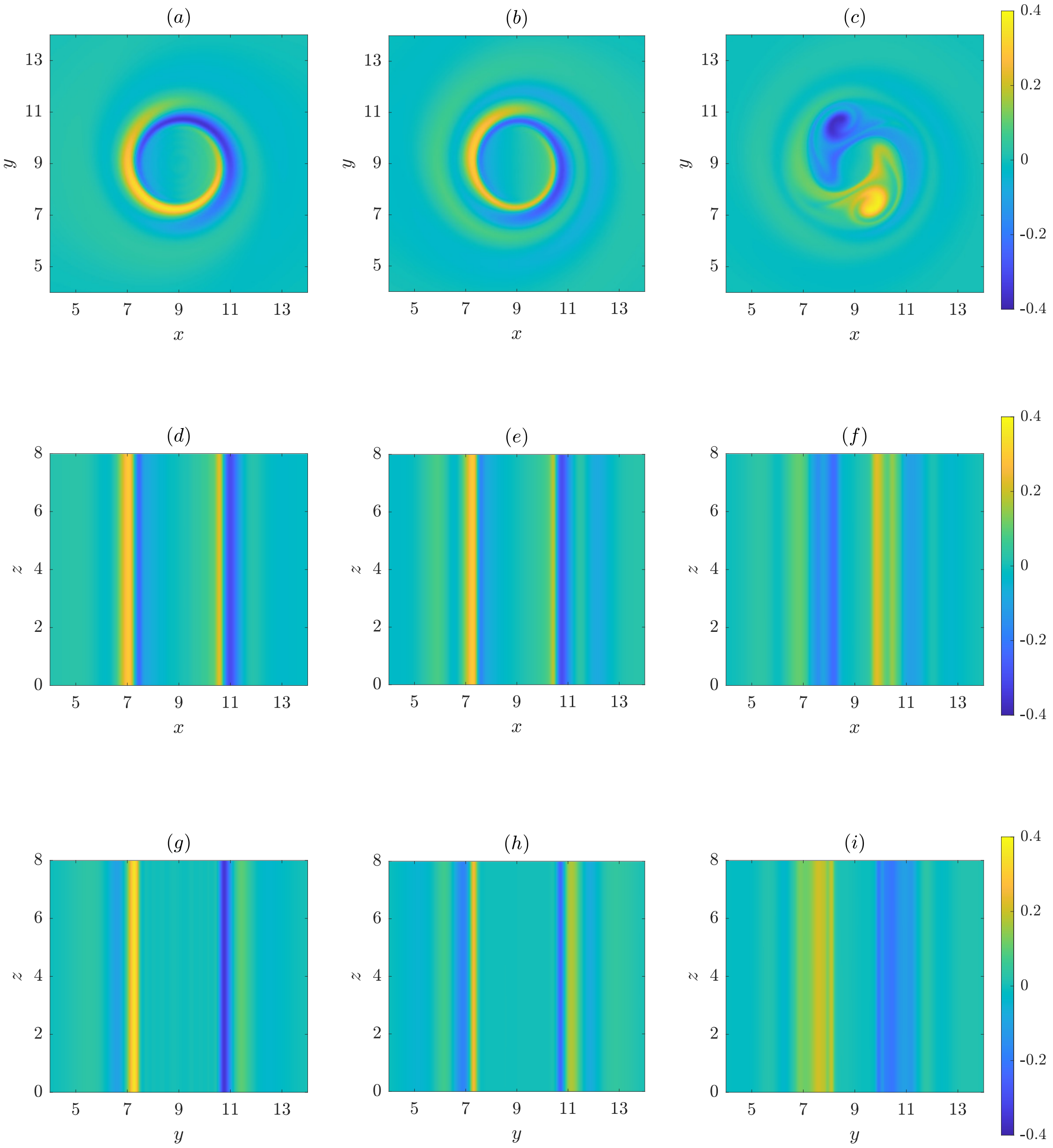

Fig. 4.21: Same as figure 4.2 but for $Ro = 2.5$ and $\widetilde{Ro} = 40$: $\widetilde{Ro} = 115$ $(Ro = 20.3)$ (a, d, g) $t = 40$, (b, e, h) $t = 56$, (c, f, i) $t = 85$.

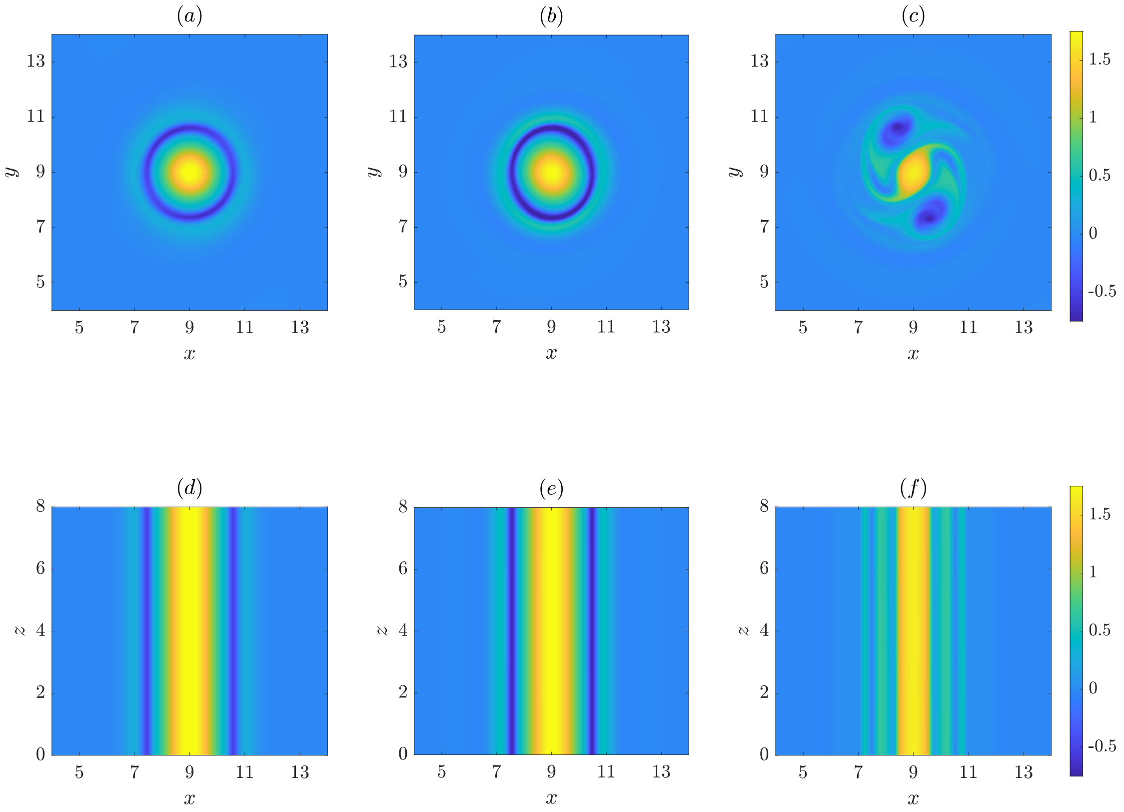

Fig. 4.22: Same as figure 4.3 but for $Ro = 2.5$ and $\widetilde{Ro} = 40$: (a, d) $t = 40$, (b, e) $t = 56$, (c, f) $t = 85$.

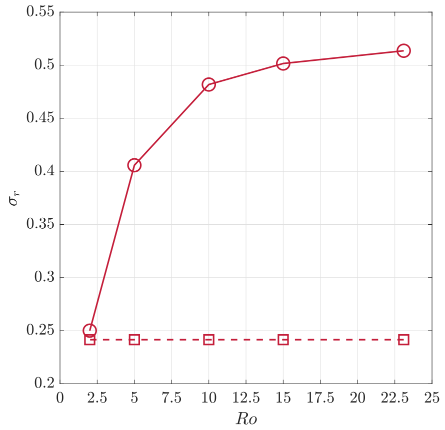

Fig. 4.23: Growth rates of the two-dimensional instability (red dashed line with square symbols) and of the three-dimensional instability (red solid line with circle symbols) obtained from local stability analyses of the non-linear solution (4.13,4.15) as a function of Ro for $\widetilde{Ro} = 23.1$, $Re = 2000$ and $F_h = 4$ at $t_{b2} = 50$.

from $\widetilde{Ro} = 40$ to $\widetilde{Ro} = 115$ while keeping the other parameters fixed to $Re = 2000$, $F_h = 4$ and $Ro \approx 20$. In the presence of such perturbations in the initial conditions, the initial evolution of the vortex remains identical to the one described in Toghraei & Billant (2022). For all the investigated parameters, the vortices eventually become unstable. For $\widetilde{Ro} \lesssim 80$, a three-dimensional instability with a dominant vertical wavenumber $k \approx 4$ develops. It resembles the instability reported by Boulanger *et al.* (2007, 2008) on a stratified tilted vortex. For $\widetilde{Ro} = 115$, the instability is two-dimensional as observed by Toghraei & Billant (2022). Hence, the dominant instability can be two-dimensional or three-dimensional depending on the parameters.

In order to understand the competition between the two instabilities, we have performed a linear stability analysis of the DNS flows by freezing them at a given time t_b, before the onset of the instabilities. The results are fully consistent with the DNS. They show that the growth peak near the vertical wavenumber $k = 4$ gradually decays as $\widetilde{Ro}$ increases and becomes lower than the growth rate in the two-dimensional limit ($k = 0$).

To gain a deeper understanding of the instabilities, we have next conducted stability analyses of the local linear and non-linear solutions in the vicinity of the critical radius provided by Toghraei & Billant (2022). We have first shown that these local solutions are in good agreement with the flows in the DNS. The local three-dimensional stability analysis assumes that the vertical variations are of the same order as the radial variations and neglects any azimuthal variations following Boulanger *et al.* (2008). At leading order, the problem is governed by a well-known Rayleigh equation around the vertical velocity field. The growth rate then scales as $Re^{2/3}/\widetilde{Ro}$. We have also provided another stability equation taking into account the second order terms. These second order terms become important for large non-traditional Rossby numbers for a given Reynolds number. The results show that the maximum growth rate drops significantly in comparison to the Rayleigh equation as the non-traditional Rossby increases. Results have also shown that the vertical velocity profile at $\theta = 0$ is more unstable than at $\theta = \pi/2$ in agreement with Boulanger *et al.* (2008). Such local three-dimensional stability analysis is not valid at small vertical wavenumbers, especially at $k = 0$. Therefore, we have also conducted a local two-dimensional stability analysis which fully takes into account the azimuthal variations. A Rayleigh equation around the angular velocity anomaly has been thereby derived. The dependence of the growth rate on Re and $\widetilde{Ro}$ has been found to be of the form $\sigma_r = Re/\widetilde{Ro}^2 \mathcal{F}(Re/\widetilde{Ro}^2)$ where $\mathcal{F}(Re/\widetilde{Ro}^2)$ tends to a constant for $Re/\widetilde{Ro}^2 \to \infty$. However, for the parameters investigated in the DNS, the dependence on Re and $\widetilde{Ro}$ through $\mathcal{F}$ is not negligible.

In a second step, we have compared the results of these local stability analyses to the stability analysis of the DNS flows. Both local three-dimensional and two-dimensional stability analyses are in good agreement with the maximum growth rates observed in the stability analysis of the DNS flows. The local three-dimensional Rayleigh equation predicts well the growth rates of the three-dimensional instability for $\widetilde{Ro} \lesssim 60$, but its accuracy weakens when $\widetilde{Ro}$ is larger. In contrast, the stability equation incorporating second order terms predicts reasonably well the maximum growth rate of the three-dimensional instability. To improve these predictions for large $\widetilde{Ro}$, it would be necessary to abandon the assumption of zero azimuthal variations and/or to consider higher order terms. The local two-dimensional Rayleigh equation also correctly predicts the growth rates at $k = 0$ of the DNS flows. Thereby, the stability analyses of the local theoretical solutions in the critical layer predict that the two-dimensional instability should dominate the three-dimensional instability for $\widetilde{Ro} \gtrsim 120$ in good agreement with the DNS.

Thanks to the reliability of the local stability analyses for predicting the maximum growth rates of each instability, we have determined the dominant instability in the parameter space $(Re, \widetilde{Ro})$ for larger values of Re. The two-dimensional instability is dominant in an intermediate range of $\widetilde{Ro}$ for each Reynolds number investigated. The three-dimensional instability is dominant only for lower $\widetilde{Ro}$. We have also investigated the effect of the traditional Rossby number Ro by means of DNS. As Ro decreases while keeping the other parameters fixed, the strength of the three-dimensional instability weakens so that the two-dimensional instability becomes dominant for the lowest value of Ro investigated. The local stability analyses are in full agreement with this behavior. As the traditional Rossby number Ro decreases, the second order terms increase and damp the three-dimensional instability whereas the two-dimensional instability is independent of Ro.

In summary, when small three-dimensional perturbations are introduced initially, the evolution of a vortex under the complete Coriolis force becomes three-dimensional for certain parameters while for others, it remains purely two-dimensional as in Toghraei & Billant (2022). The three-dimensional and two-dimensional instabilities are due to different mechanisms and different components of the flow generated in the critical layer. The two-dimensional instability comes from the shear of the angular velocity profile whereas the three-dimensional instability comes from the shear of the vertical velocity field. The latter is strong and develops more quickly than the former. However, the three-dimensional shear instability is highly sensitive to the damping effects due to the traditional Coriolis force (i.e. $\hat{\phi}$) and to the stable stratification and the buoyancy field (i.e. $\hat{N}$) that oppose against three-dimensional variations.

A theoretical criterion for the occurrence of the two-dimensional instability has been provided by Toghraei & Billant (2022). In the future, it would be interesting to obtain also an analytical criterion for the threshold between the three-dimensional and two-dimensional instabilities. It would be also interesting to investigate whether a similar competition of instabilities exists if the vortex axis is aligned along the rotation vector Ω_b instead of the vertical.

Appendix

A Additional figures

The figures 4.24,4.25 and 4.26,4.27 show the evolution of the vortex for the intermediate values of the non-traditional Rossby number $\widetilde{Ro} = 60$ and $\widetilde{Ro} = 80$. The figures 4.28 and 4.29 compares also the DNS flows to the local theoretical solutions for these two values of $\widetilde{Ro}$.

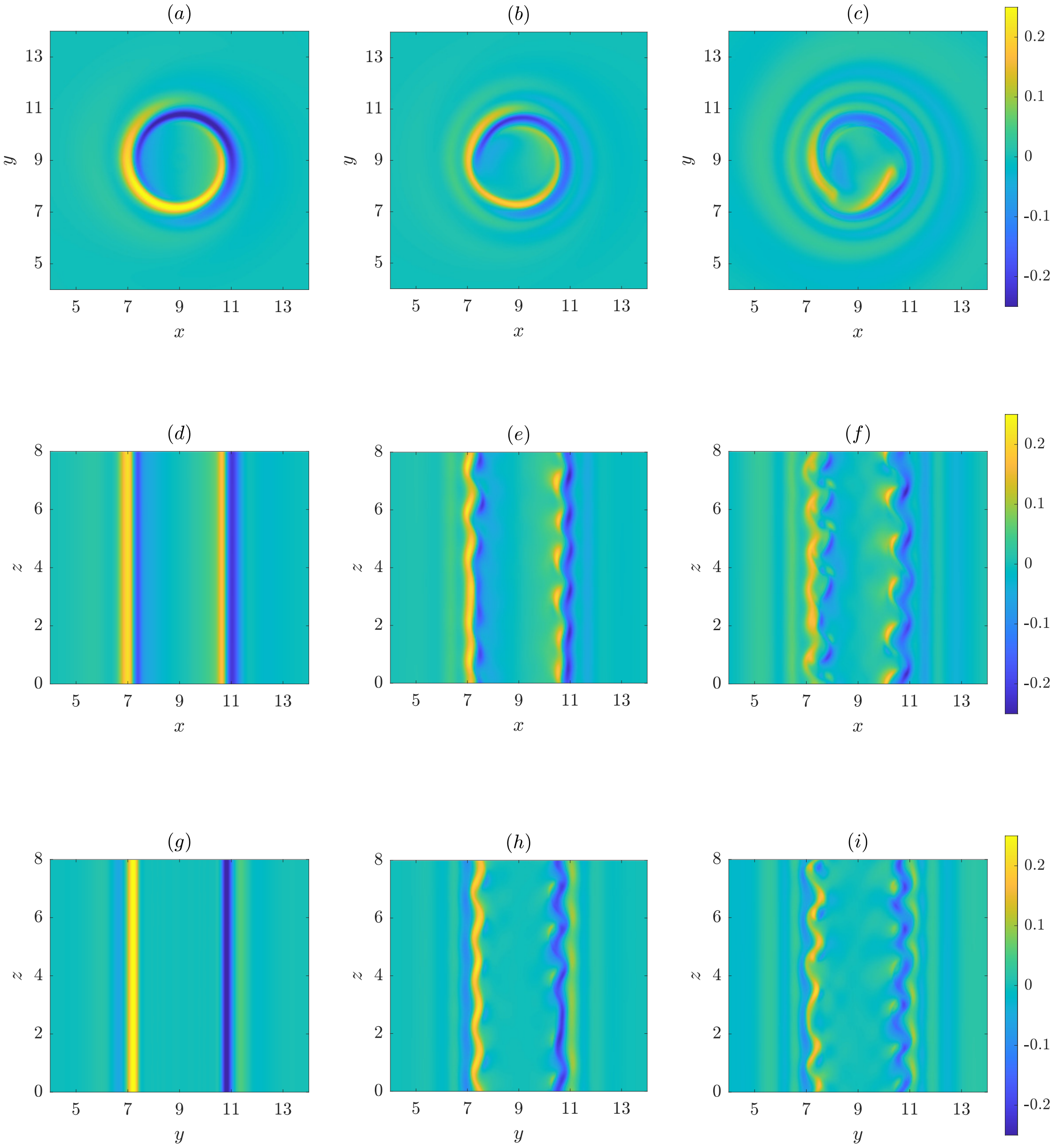

Fig. 4.24: Same as figure 4.2 but for $\widetilde{Ro} = 60$ and $Ro = 21.2$: (a, d, g) $t = 50$, (b, e, h) $t = 75$, (c, f, i) $t = 80$.

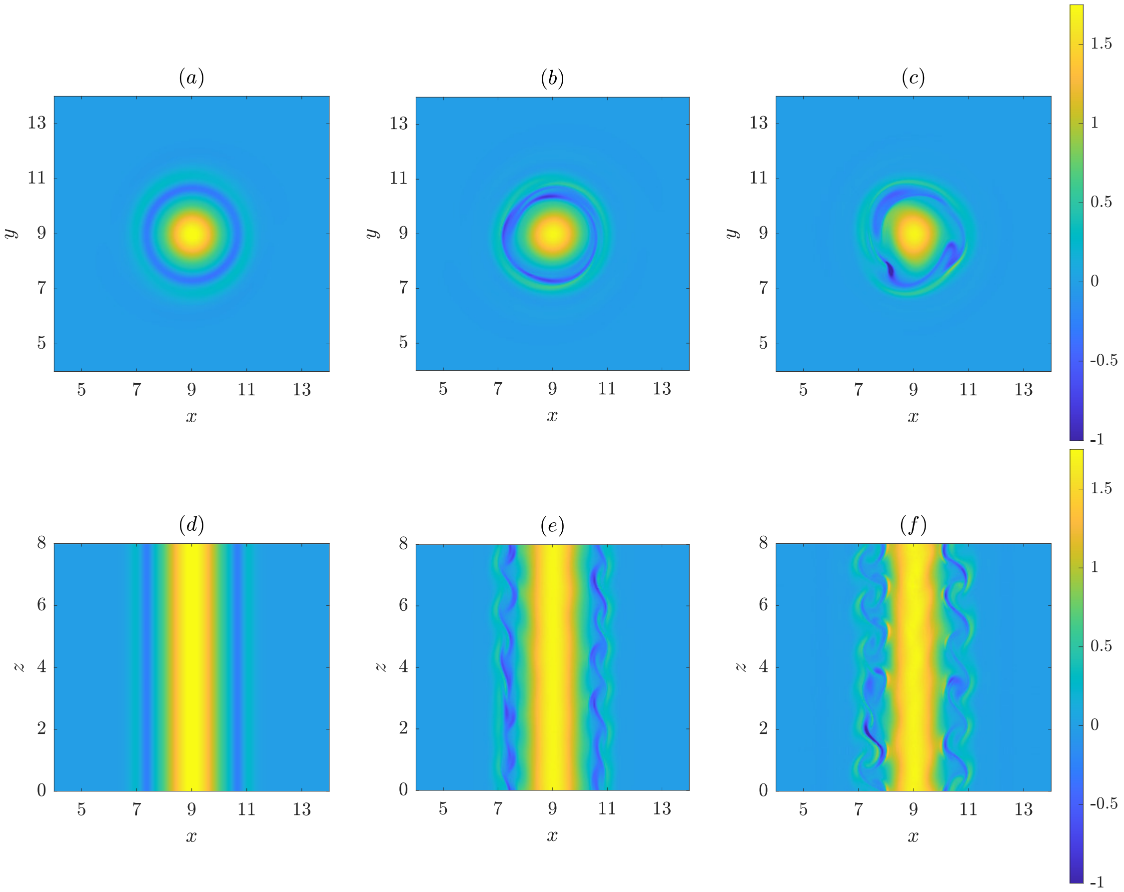

Fig. 4.25: Same as figure 4.3 but for $\widetilde{Ro} = 60$ and $Ro = 21.2$: (a, d) $t = 50$, (b, e) $t = 75$, (c, f) $t = 80$.

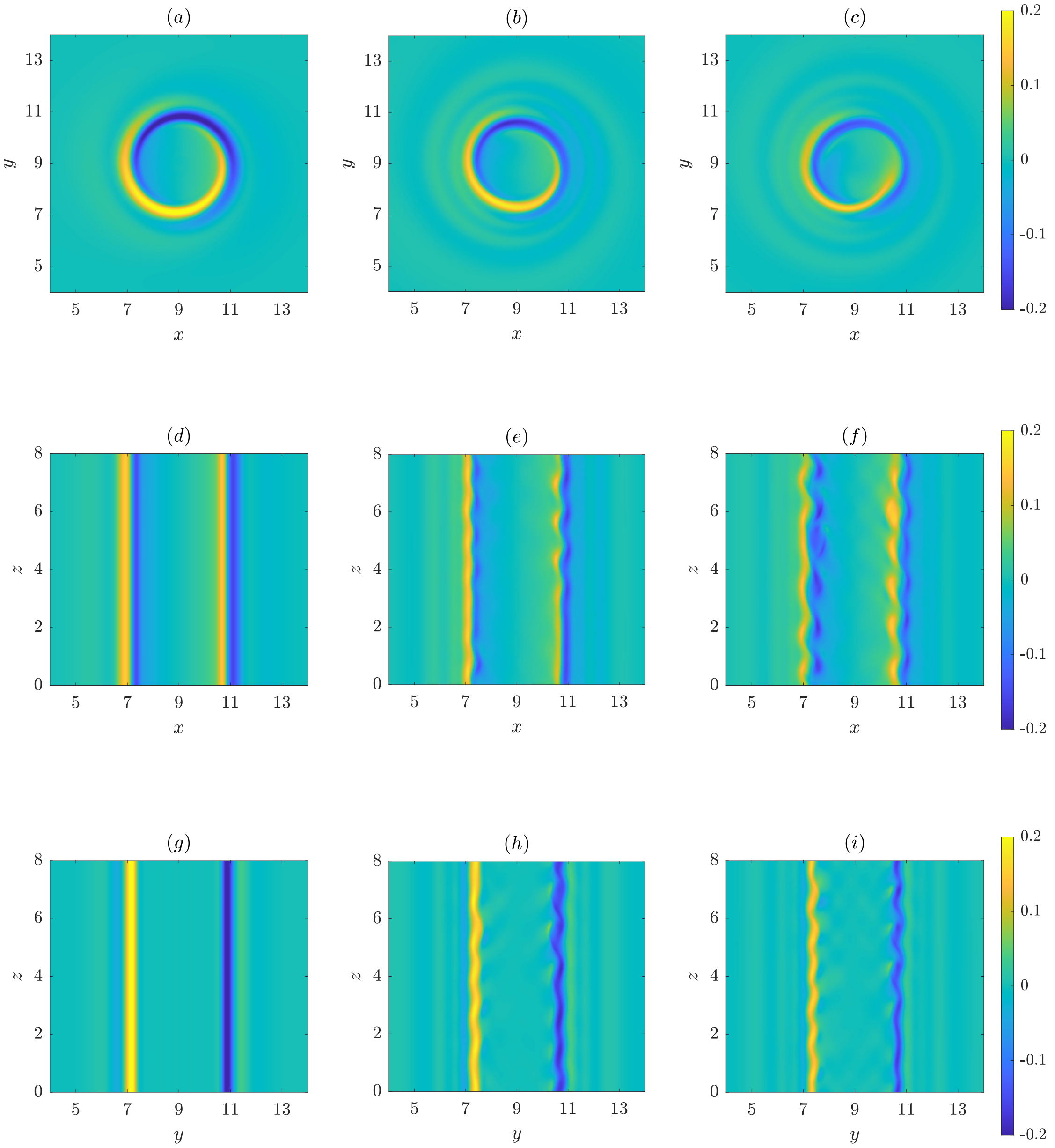

Fig. 4.26: Same as figure 4.2 but for $\widetilde{Ro} = 80$ and $Ro = 20.7$: (a, d, g) $t = 50$, (b, e, h) $t = 98$, (c, f, i) $t = 102$.

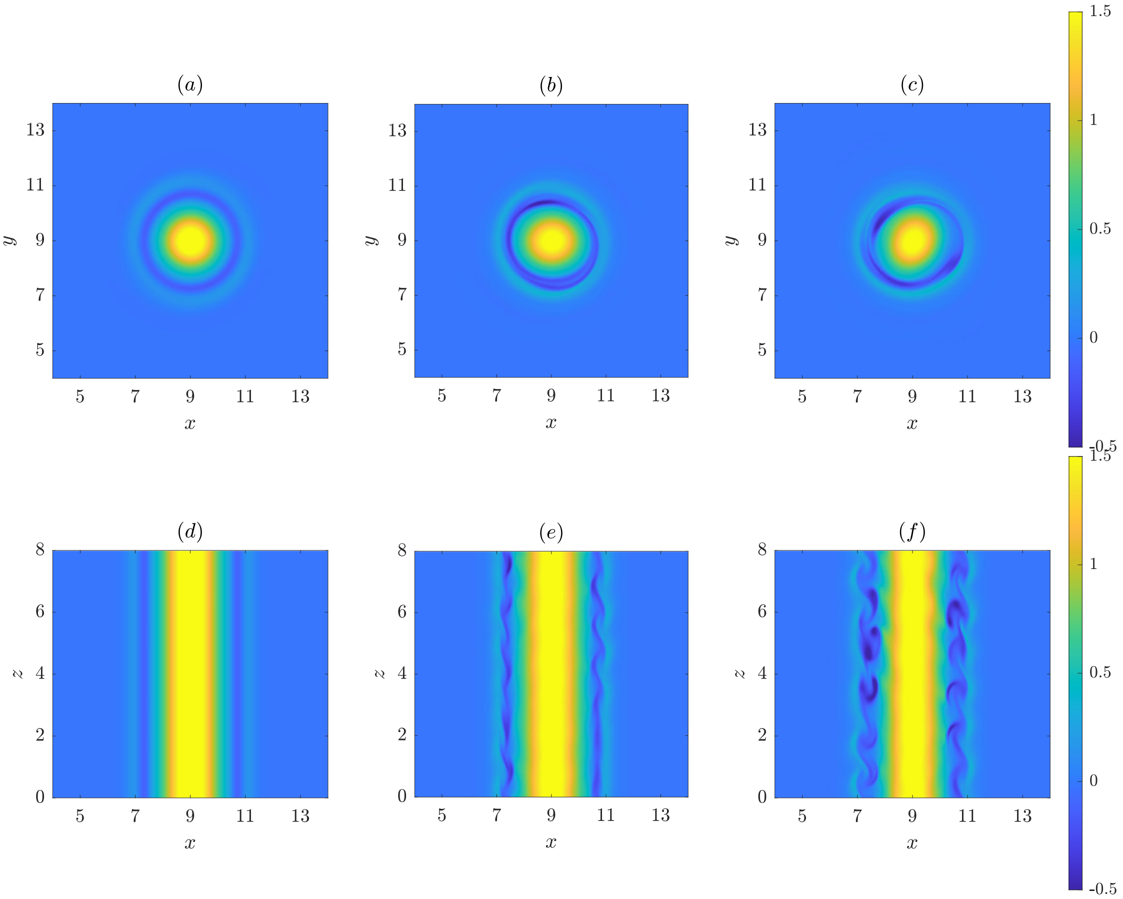

Fig. 4.27: Same as figure 4.3 but for $\widetilde{Ro} = 80$ and $Ro = 20.7$: (a, d) $t = 50$, (b, e) $t = 98$, (c, f) $t = 102$.

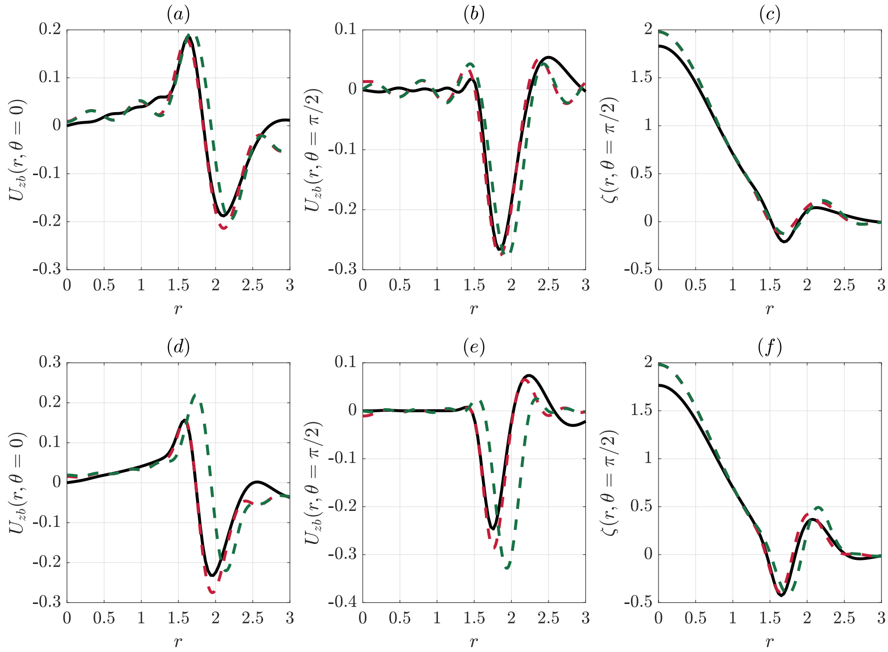

Fig. 4.28: Comparison between the vertical velocity at $\theta = 0$ (left column) and $\theta = \pi/2$ (middle column) in the DNS (black solid line), predicted by the viscous solution (4.13,4.18-4.16) (green dashed line) and by the non-linear equations (4.13,4.15) (red dashed line) at $t_{b1} = 40$ (top row) and $t_{b2} = 60$ (bottom row) for $\widetilde{Ro} = 60$ and $Re = 2000$, $F_h = 4$, $Ro = 21.2$.

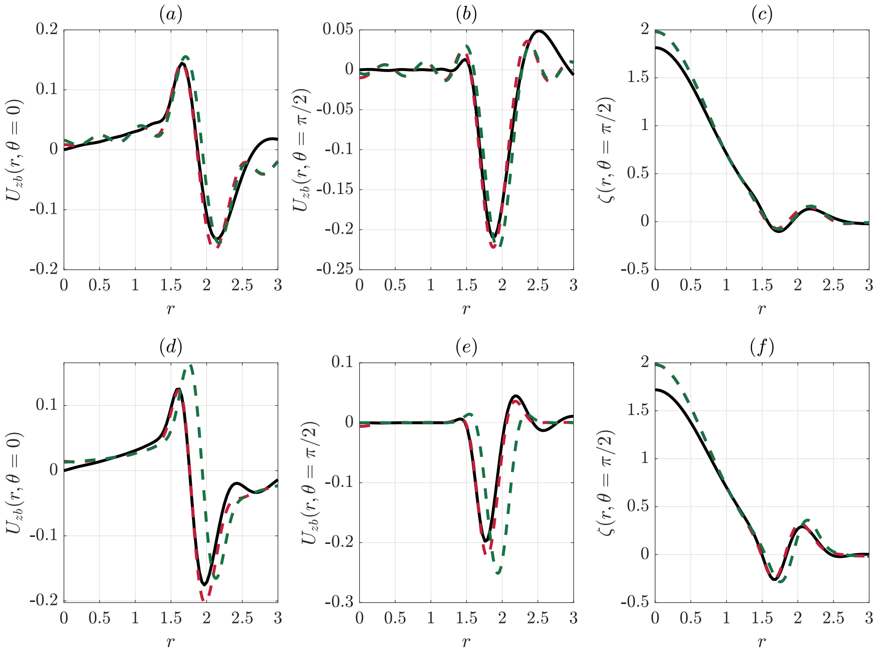

Fig. 4.29: Comparison between the vertical velocity at $\theta = 0$ (left column) and $\theta = \pi/2$ (middle column) in the DNS (black solid line), predicted by the viscous solution (4.13,4.18-4.16) (green dashed line) and by the non-linear equations (4.13,4.15) (red dashed line) at $t_{b1} = 45$ (top row) and $t_{b2} = 75$ (bottom row) for $\widetilde{Ro} = 80$ and $Re = 2000$, $F_h = 4$, $Ro = 20.7$.

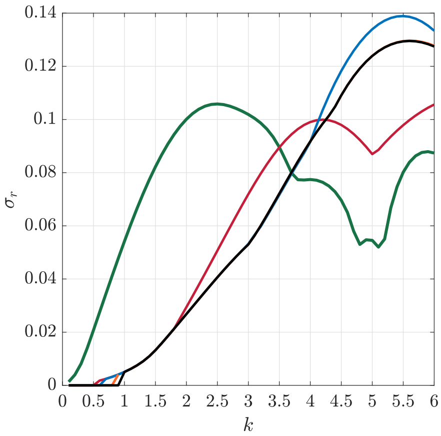

Fig. 4.30: Growth rate as a function of k for $\widetilde{Ro} = 115$ at $t_{b2} = 100$ using the linear solution (4.13,4.16,4.18) for $Re = 2000$, $F_h = 4$ and $Ro = 20.3$. The different curves correspond to: (4.24) (green), (4.21) with $N_m = 3$ (red), $N_m = 5$ (blue), $N_m = 9$ (orange) and $N_m = 15$ (black).

B Test of the assumption $\partial/\partial\theta = 0$ in the three-dimensional local stability analysis

In order to test the effect of the assumption $\partial/\partial\theta = 0$ used to derive (4.24) from (4.21) and to solve simple the stability problem, we have also solved (4.21) without this hypothesis by writing the perturbations in the form

$$[u_r, u_\theta, u_z, b, p](r,\theta,z,t) = \left(\sum_{n=-N_m}^{N_m} [u_{rn}, u_{\theta n}, u_{zn}, b_n, p_n](r) \mathrm{e}^{\mathrm{i}n\theta} \right) \mathrm{e}^{\sigma t + \mathrm{i}\tilde{k}z} + c.c., \quad (4.32)$$

where N_m is the maximum azimuthal wavenumber. Then, (4.21) has been solved by using a pseudo-spectral Chebyshev collocation method along the radial direction as done for (4.24). The eigenvalue problem is much larger than for (4.24) but can be still computed easily using the function *eigs* instead of *eig* from Matlab.

Figure 4.30 shows the growth rate obtained for various values of N_m for $\widetilde{Ro} = 115$ at $t_{b2} = 100$ using the linear solution (4.13,4.16,4.18) for $Re = 2000$, $F_h = 4$ and $Ro = 20.3$. The green curve corresponds to the growth rate obtained from (4.24), i.e. by assuming $\partial/\partial\theta = 0$, and which is already plotted in figure 4.18(b). When N_m is increased, we can see that the first peak disappears but the level of the remaining peak is close to one predicted by (4.24). Furthermore, the curves for $N_m = 9$ (orange line) and $N_m = 15$ (black line) are almost superposed indicating a convergence as the number of azimuthal modes increase. Hence, the assumption $\partial/\partial\theta = 0$ does not seem to be too crude.

Chapter 5

Conclusions and perspectives

We have studied the evolution of a Lamb-Oseen vortex in a stratified rotating fluid under the complete Coriolis force. Our study employed DNS as well as asymptotic analyses. According to the non-dimensional form of the governing equations, the dynamics of the vortex is governed by five parameters: the Reynolds number, the Froude number, and traditional and non-traditional Rossby numbers that measure the vertical and horizontal background rotation, respectively, and the Schmidt number that has been always set to unity.

For pure two-dimensional initial conditions, DNS shows that the vortex remains completely two-dimensional throughout its evolution even if there are three velocity components. It may become three-dimensional, however, when small three-dimensional perturbations are added initially. Thus, we divided our study into two parts: the two-dimensional evolution (chapter 3) and the full three-dimensional evolution (chapter 4).

In the two-dimensional case, DNS for Froude numbers larger than unity have shown that a vertical velocity field and a vertical vorticity anomaly are generated at a certain radius due to the non-traditional Coriolis force. Gradually, the vertical velocity field and the vertical vorticity anomaly concentrate and increase around this radius. At some point, a two-dimensional instability occurs in the flow for Reynolds numbers sufficiently large and non-traditional Rossby numbers $\widetilde{Ro}$ sufficiently low.

To unravel this dynamics, we have carried out asymptotic analyses for large non-traditional Rossby numbers $\widetilde{Ro}$. In the absence of viscous effects and time dependence, the theoretical analysis shows that the vertical velocity is singular when the Froude number is larger than unity at a radius where the angular velocity is equal to the inverse of the Froude number (i.e. the Brunt–Väisälä frequency in dimensional form). This singularity is first regularized by the time dependence and then by a combination of viscous effects and time dependence in the saturation phase. Hence, two linear solutions for the vertical velocity and the vertical vorticity anomaly have been provided for each stage of this evolution. These linear solutions are in great agreement with the DNS in both stages. A non-linear set of equations has been also provided. It is in even better agreement with the DNS, indicating the importance of nonlinear effects.

Next, we have shown that an inflection point appears in the vertical vorticity field and that it is responsible for the onset of the two-dimensional instability. Using the asymptotic solutions of the vertical vorticity, an instability condition in terms of $(Re, \widetilde{Ro})$ has been derived from the Rayleigh criterion for the shear instability. In the parameter space $(Re, \widetilde{Ro})$, the criterion predicts perfectly the stable and unstable domains and shows that even for small non-traditional Rossby numbers, the vortex is unstable for large Reynolds numbers.

We have then examined the evolution of the vortex when small three-dimensional perturbations are added initially. Although the initial evolution of the vortex remains similar, the instability can differ: it is three-dimensional below a critical non-traditional Rossby number. This three-dimensional instability appears similar to the shear instability reported by Boulanger *et al.* (2007, 2008) on a stratified tilted vortex. Above the critical non-traditional Rossby number, the instability remains two-dimensional as observed before. Hence, the dominant instability is determined by the parameters.

To understand the competition between the two-dimensional and three-dimensional instabilities, we have performed a linear stability analysis of the DNS flows. The results confirm that the three-dimensional instability becomes dominant over the two-dimensional instability when $\widetilde{Ro}$ decreases. We have also conducted local stability analyses of both linear and non-linear solutions provided in chapter 3 in order to gain a deeper understanding of the instabilities. The local three-dimensional stability analysis shows that the growth rate of the three-dimensional instability can be adequately predicted by a Rayleigh equation taking into account only the vertical velocity field as base flow. However, its accuracy weakens when $\widetilde{Ro}$ increases for a given Reynolds number. The equation taking into account second order effects then provides better accuracy. In addition, the local two-dimensional stability analysis gives a Rayleigh equation with the angular velocity field as base flow that is reliable for predicting the growth rate of the two-dimensional instability.

The local stability analyses demonstrate thereby that the two-dimensional instability is a shear instability due to an inflection point in the vertical vorticity profile, while the three-dimensional instability is a shear instability of the vertical velocity. In addition, we have investigated the domains of existence of the instabilities in the parameter space $(Re, \widetilde{Ro})$ by means of the local stability analyses. Results show that the two-dimensional instability is the most dangerous instability in an intermediate range of $\widetilde{Ro}$ while the three-dimensional instability is dominant for lower $\widetilde{Ro}$.

Finally, in order to discuss whether or not the process described in this thesis can occur on atmospheric and oceanic vortices, we have reproduced in figure 5.1 their domains of existence in the parameter space $(F_h, \widetilde{Ro})$ from table 1.1 in chapter 1. Only some of these vortices are mapped in figure 5.1, while others are not shown either because they are outside our region of interest or cover a small area. Two dashed lines are also shown in figure 5.1 separating the stable region (above the line) and the unstable region (below the line). They have been obtained from the instability criterion (3.71) from chapter 3 for the Reynolds numbers $Re = 10^5$ (black dashed line) and $Re = 10^7$ (grey dashed line) for $a = \infty$ and $c = 0.4$. The Reynolds numbers are chosen merely to show the trend of the criterion when Re increases. The vertical solid line represents also the condition $F_h > 1$ required to have a critical layer. Only the region $F_h < 10$ is displayed since the instabilities are expected to be strong when the Froude number is not too large so that the critical radius is close to the vortex core.

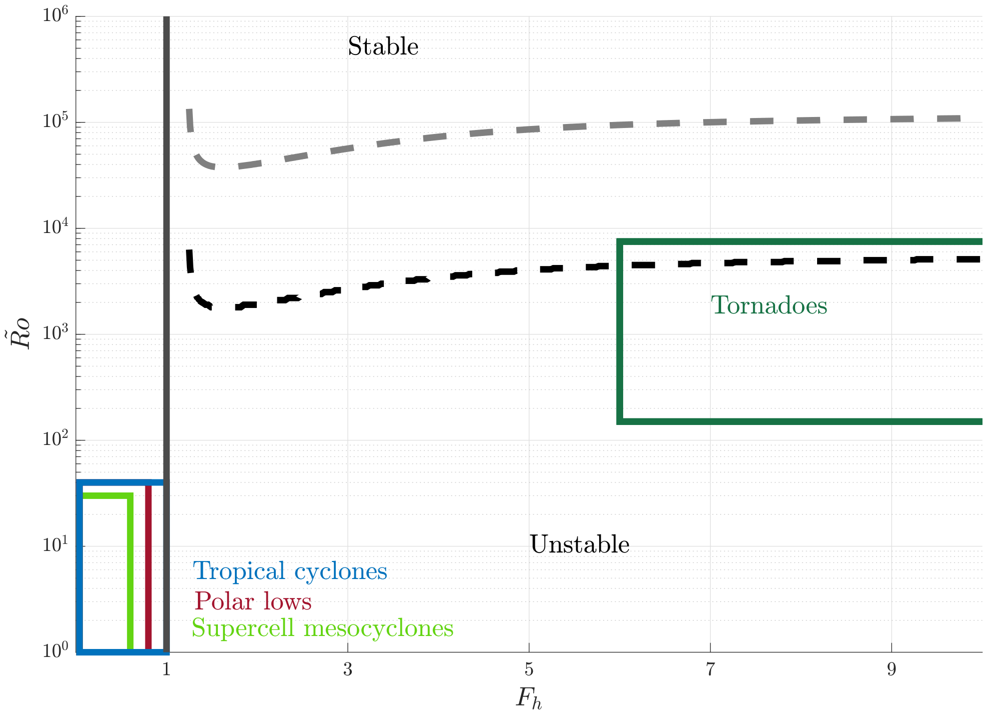

Fig. 5.1: Map of some geophysical vortices in the parameter space $(F_h, \widetilde{Ro})$. Two dashed lines are showing the criterion (3.71) from chapter 3 for $Re = 10^5$ (black dashed line) and $Re = 10^7$ (grey dashed line) for $a = \infty$ and $c = 0.4$. Vortices below the dashed lines are unstable. The black solid line shows the critical Froude number $F_h = 1$.

It is striking that no geophysical vortices are observed in the range of Froude numbers $1 < F_h < 6$ where the critical layer and associated instabilities are expected to be strong. In fact, the instabilities themselves may explain why no vortices are found in this range of Froude number. Furthermore, the instabilities grow quite quickly and affect the vortices typically after 50-100 non-dimensional time units, as seen from the DNS. When converted in real-time for specific vortices, such duration is relatively short. For example, for tornadoes with a turnover time scale L_h/U of the order of a few minutes, this corresponds to a time of the order of one hour. Hence, the instabilities should appear quickly after the vortex formation leading to its rapid decay. This might explain why no vortices are observed in the Froude number range $1 < F_h < 6$. We can conclude from this that considering the full Coriolis force might have a significant impact on the formation of vortices and force them to exist in the stable region.

As far as perspectives are concerned, it would be interesting to study a stratified vortex under the complete Coriolis force experimentally. Making a horizontal background rotation i.e. misaligning the buoyancy force and the rotation vector, is the most challenging part. This can be done by rotating a turn table very fast since the apparent gravity is then the sum of the gravity and the centrifugal force. There is therefore an angle with the vertical rotation vector. This method has been used for example by Sheremet (2004) to study convection.

It could be also interesting to study numerically different vortex configurations under the complete Coriolis force. For example, the case of a vortex whose axis is tilted between the vertical and total background rotation vector could be investigated. A study of vortices with lenticular shapes would be also of interest. It could be also worth investigating the effects of the full Coriolis force on waves propagating within the vortex. The horizontal component of the background rotation could trigger wave resonances, causing instabilities similar to the elliptical instability, or generate secondary flows as a result of a new critical layer similar to the vortex studied by Caillol (2012) under the traditional approximation.

Bibliography

Abramowitz, M. & Stegun, I. A., ed. 1972 *Handbook of Mathematical Functions with Formulas, Graphs, and Mathematical Tables*, tenth printing edn. Washington, DC, USA: U.S. Government Printing Office.

Billant, P. & Bonnici, J. 2020 Evolution of a vortex in a strongly stratified shear flow. part 2. numerical simulations. *J. Fluid Mech.* **893**, A18.

Bonnici, J. 2018 Vertical decorrelation of a vortex by an external shear flow in a strongly stratified fluid. Phd thesis, Université Paris-Saclay.

Boulanger, N., Meunier, P. & Le Dizès, S. 2007 Structure of a stratified tilted vortex. *J. Fluid Mech.* **583**, 443–458.

Boulanger, N., Meunier, P. & Le Dizès, S. 2008 Tilt-induced instability of a stratified vortex. *J. Fluid Mech.* **596**, 1–20.

Caillol, P. 2012 Multiple vortices induced by a tridimensional critical layer in a rapidly rotating vortex. *IMA J. Appl. Math.* **77** (3), 282–292.

Carton, X. & Legras, B. 1994 The life-cycle of tripoles in two-dimensional incompressible flows. *J. Fluid Mech.* **267**, 53–82.

Chew, R., Schlutow, M. & Klein, R. 2022 Instability of the isothermal, hydrostatic equatorial atmosphere at rest under the full coriolis acceleration. *arXiv preprint arXiv:2206.00577* .

Cushman-Roisin, B. & Beckers, J-M. 2011 *Introduction to geophysical fluid dynamics: physical and numerical aspects*. Academic press.

Delbende, I. 1998 Réponse impulsionnelle dans les jets tournants et les sillages plans: analyse spatio-temporelle par simulation numérique directe. PhD thesis, Palaiseau, Ecole polytechnique.

Deloncle, A. 2014 *NS3D v2.14: user's manual*. Ecole polytechnique.

Deloncle, A., Billant, P. & Chomaz, J. 2008 Nonlinear evolution of the zigzag instability in stratified fluids: a shortcut on the route to dissipation. *J. Fluid Mech.* **599**, 229–239.

Denbo, D. W. & Skyllingstad, E. D. 1996 An ocean large-eddy simulation model with application to deep convection in the greenland sea. *J. Geophys. Res. Oceans* **101** (C1), 1095–1110.

Drazin, P. G. & Reid, W. H. 2004 *Hydrodynamic stability*. Cambridge university press.

Eckart, C. 1960 *Introduction to geophysical fluid dynamics: physical and numerical aspects*. Pergamon.

Etling, D. 1971 The stability of an ekman boundary layer flow as influenced by thermal stratification. *Beitr. Phys. Atmos.* **44**, 168–186.

Fjørtoft, R. 1950 Application of integral theorems in deriving criteria of stability for laminar flows and for the baroclinic circular vortex **17**, 1–52.

Flor, J.-B. 2010 *Fronts, waves and vortices in geophysical flows*, , vol. 805. Springer.

Gerkema, T., Zimmerman, J.T.F., Maas, L.R.M. & Van Haren, H. 2008 Geophysical and astrophysical fluid dynamics beyond the traditional approximation. *Rev. Geophys.* **46** (2), RG2004.

Hayashi, M. & Itoh, H. 2012 The importance of the nontraditional coriolis terms in large-scale motions in the tropics forced by prescribed cumulus heating. *J. Atmos. Sci.* **69** (9), 2699–2716.

Hickernell, F. J. 1984 Time-dependent critical layers in shear flows on the beta-plane. *J. Fluid Mech.* **142**, 431–449.

Hua, B. L., Moore, D. W. & Le Gentil, S. 1997 Inertial nonlinear equilibration of equatorial flows. *J. Fluid Mech.* **331**, 345–371.

Igel, M.R. & Biello, J.A. 2020 The nontraditional coriolis terms and tropical convective clouds. *J. Atmos. Sci.* **77** (12), 3985–3998.

Killworth, P. D. & McIntyre, M. E. 1985 Do rossby-wave critical layers absorb, reflect, or over-reflect? *J. Fluid Mech.* **161**, 449–492.

Kloosterziel, R.C., Carnevale, G.F. & Orlandi, P. 2017 Equatorial inertial instability with full coriolis force. *J. Fluid Mech.* **825**, 69–108.

Knobby, R. D., Rhome, J. R. & Brown, D. P. 2023 Tropical cyclone report hurricane katrina.

Kohma, M. & Sato, K. 2013 Kelvin and rossby waves trapped at boundaries under the full coriolis force. *Sola* **9**, 9–14.

Kossin, J.P., Schubert, W.H. & Montgomery, M.T. 2000 Unstable interactions between a hurricane's primary eyewall and a secondary ring of enhanced vorticity. *J. Atmos. Sci.* **57** (24), 3893–3917.

Lavrovskii, EK, Semenova, IP, Slezkin, LN & Fominykh, VV 2000 Mediterranean lenses as liquid gyroscopes in the ocean. *Dokl. Phys.* **45** (11), 606–609.

Le Dizès, S. 2000 Non-axisymmetric vortices in two-dimensional flows. *J. Fluid Mech.* **406**, 175–198.

Leibovich, S. & Lele, S. K. 1985 The influence of the horizontal component of earth's angular velocity on the instability of the ekman layer. *J. Fluid Mech.* **150**, 41–87.

Lin, C.-L., Ferziger, J. H., Koseff, J. R. & Monismith, S. G. 1993 Simulation and stability of two-dimensional internal gravity waves in a stratified shear flow. *Dyn. Atmospheres Oceans* **19** (1-4), 325–366.

Maes, C. & O'Kane, T. J. 2014 Seasonal variations of the upper ocean salinity stratification in the tropics. *J. Geophys. Res. Oceans* **119** (3), 1706–1722.

Marshall, J. & Schott, F. 1999 Open-ocean convection: Observations, theory, and models. *Rev. Geophys.* **37** (1), 1–64.

Maslowe, S. A. 1986 Critical layers in shear flows. *Annu. Rev. Fluid Mech.* **18** (1), 405–432.

Maslowe, S. A. & Nigam, N. 2008 The nonlinear critical layer for kelvin modes on a vortex with a continuous velocity profile. *SIAM J. Appl. Math.* **68** (3), 825–843.

Orszag, S. A. 1971 On the elimination of aliasing in finite-difference schemes by filtering high-wavenumber components. *J. Atmos. Sci.* **28** (6), 1074–1074.

Park, J., Prat, V., Mathis, S. & Bugnet, L. 2021 Horizontal shear instabilities in rotating stellar radiation zones-ii. effects of the full coriolis acceleration. *Astron. Astrophys.* **646**, A64.

Pickart, R. S., Torres, D. J. & Clarke, R A. 2002 Hydrography of the labrador sea during active convection. *J. Phys. Oceanogr* **32** (2), 428–457.

Pradeep, D. S. & Hussain, F. 2004 Effects of boundary condition in numerical simulations of vortex dynamics. *J. Fluid Mech.* **516**, 115–124.

Rayleigh, Lord 1880 On the stability, or instability, of certain fluid motions. *Proc. London Math. Soc.* **9**, 57–70.

Schecter, D. A. & Montgomery, M. T. 2006 Conditions that inhibit the spontaneous radiation of spiral inertia–gravity waves from an intense mesoscale cyclone. *J. Atmos. Sci.* **63** (2), 435–456.

Semenova, I.P. & Slezkin, L.N. 2003 Dynamically equilibrium shape of intrusive vortex formations in the ocean. *Fluid Dyn.* **38** (5), 663–669.

Sheremet, V.A. 2004 Laboratory experiments with tilted convective plumes on a centrifuge: a finite angle between the buoyancy force and the axis of rotation. *J. Fluid Mech.* **506**, 217–244.

Stewartson, K. 1977 The evolution of the critical layer of a rossby wave. *Geophys. Astrophys. Fluid Dyn.* **9** (1), 185–200.

Straneo, F., Kawase, M. & Riser, S. C. 2002 Idealized models of slantwise convection in a baroclinic flow. *J. Phys. Oceanogr* **32** (2), 558–572.

Taylor, G. I. 1923 Experiments on the motion of solid bodies in rotating fluids. *Proc. Math. Phys.* **104** (725), 213–218.

Toghraei, I & Billant, P 2022 Dynamics of a stratified vortex under the complete coriolis force: two-dimensional three-components evolution. *J. Fluid Mech.* **950**, A29.

Tort, M. & Dubos, T. 2014 Dynamically consistent shallow-atmosphere equations with a complete coriolis force. *Q. J. R. Meteorol. Soc.* **140** (684), 2388–2392.

Tort, M., Dubos, T., Bouchut, F. & Zeitlin, V. 2014 Consistent shallow-water equations on the rotating sphere with complete coriolis force and topography. *J. Fluid Mech.* **748**, 789–821.

Tort, M., Ribstein, B. & Zeitlin, V. 2016 Symmetric and asymmetric inertial instability of zonal jets on the-plane with complete coriolis force. *J. Fluid Mech.* **788**, 274–302.

Wang, C. & Balmforth, N.J. 2020 Nonlinear dynamics of forced baroclinic critical layers. *J. Fluid Mech.* **883**, A12.

Wang, C. & Balmforth, N. J. 2021 Nonlinear dynamics of forced baroclinic critical layers ii. *J. Fluid Mech.* **917**, A48.

Wippermann, F. 1969 The orientation of vortices due to instability of the ekman-boundary layer. *Beitr. Phys. Atmos.* **42** (4), 225–244.

Zeitlin, V. 2018 Symmetric instability drastically changes upon inclusion of the full coriolis force. *Phys. Fluids* **30** (6), 061701.

Zhang, R. & Yang, L. 2021 Theoretical analysis of equatorial near-inertial solitary waves under complete coriolis parameters. *Acta Oceanol. Sin.* **40** (1), 54–61.

ECOLE
DOCTORALE

Titre :Dynamique d'un tourbillon dans les fluides stratifiés tournants en présence de la force de Coriolis complète.

Mots clés : Fluides géophysiques, l'instabilité, écoulements tourbillonnaires

Résumé : Les études des effets de la rotation planétaire sur les mouvements des fluides géophysiques sont généralement réalisées dans le cadre de l'approximation traditionnelle. Celle-ci consiste à ne prendre en compte que la composante verticale du vecteur de rotation planétaire à une latitude donnée, tandis que la composante horizontale est négligée. Cette thèse étudie la dynamique d'un tourbillon lorsque l'on tient compte également de la composante horizontale (approximation non traditionnelle). Dans ce but, nous effectuons des simulations numériques directes de l'évolution d'un tourbillon vertical de Lamb-Oseen en présence de la force de Coriolis complète dans un fluide stratifié de manière stable. Les résultats de ces simulations sont complétés et interprétés par des analyses asymptotiques lorsque la composante horizontale de la rotation planétaire est petite et le nombre de Reynolds grand. Il est montré que la force de Coriolis due à la composante horizontale de la rotation planétaire génère une couche critique au rayon où la vitesse angulaire du tourbillon est égale à la fréquence Brunt–Väisälä lorsque le nombre de Froude est supérieur à l'unité. De ce fait, un champ de vitesse verticale intense et une anomalie de vorticité verticale sont créés au voisinage de la couche critique. Ces écoulements peuvent alors conduire à deux types d'instabilité : une instabilité bidimensionnelle déclenchée par le cisaillement de l'anomalie de vorticité verticale et une instabilité tridimensionnelle due au cisaillement du champ de vitesse verticale. Les domaines d'existence de ces deux instabilités sont cartographiés dans l'espace des paramètres. Elles conduisent toutes deux à une décroissance rapide du tourbillon jusqu'à la disparition de la couche critique lorsque la vitesse angulaire est partout inférieure à la fréquence de flottabilité. Ce processus peut se produire même si la composante horizontale de la rotation planétaire est très faible lorsque le nombre de Reynolds est grand. Par conséquent, la composante horizontale de la rotation planétaire pourrait avoir un impact beaucoup plus important sur les tourbillons géophysiques que ce que l'on pourrait penser en considérant seulement son ordre de grandeur.

Title : Dynamics of a vortex in stratified-rotating fluids under the complete Coriolis force.

Keywords : geophysical flows, instability, vortex flows

Abstract : The effects of the planetary rotation on geophysical fluid motions are usually studied using the traditional approximation. This consists in taking into account only the vertical component of the planetary rotation vector at a given latitude, while the horizontal component is neglected. This thesis studies the dynamics of a vortex when the horizontal component is also taken into account (non-traditional approximation). To this end, we perform direct numerical simulations of the evolution of a vertical Lamb-Oseen vortex in the presence of the complete Coriolis force in a stably stratified fluid. The results of these simulations are completed and interpreted by asymptotic analyses when the horizontal component of the planetary rotation is small and the Reynolds number is large. It is shown that the Coriolis force due to the horizontal component of the planetary rotation generates a critical layer at the radius where the angular velocity of the vortex is equal to the Brunt–Väisälä frequency when the Froude number is greater than unity. As a result, an intense vertical velocity field and a vertical vorticity anomaly are created in the vicinity of the critical layer. These flows can then lead to two types of instability : a two-dimensional instability triggered by the shear of the vertical vorticity anomaly and a three-dimensional instability due to the shear of the vertical velocity field. The domains of existence of these two instabilities are mapped in the parameter space. They both lead to a rapid decay of the vortex until the critical layer disappears when the angular velocity is everywhere below the buoyancy frequency. This process can occur even if the horizontal component of the planetary rotation is very small when the Reynolds number is large. Therefore, the horizontal component of the planetary rotation could have a much larger impact on geophysical vortices than one might think by considering only its order of magnitude.

Institut Polytechnique de Paris
91120 Palaiseau, France